Design of Continuous Crystallizers for Production of Active Pharmaceutical Ingredients

Capellades Mendez, Gerard

Publication date:
2017

Document Version
Publisher's PDF, also known as Version of record

Link back to DTU Orbit

Citation (APA):
Capellades Mendez, G. (2017). *Design of Continuous Crystallizers for Production of Active Pharmaceutical Ingredients*. Technical University of Denmark.

Design of Continuous Crystallizers for Production of Active Pharmaceutical Ingredients

by Gerard Capellades Méndez

PhD thesis
September 14, 2017

Supervisor	Søren Kiil (DTU Chemical Engineering)
Co-supervisors	Kim Dam-Johansen (DTU Chemical Engineering)
	Michael J. Mealy (H. Lundbeck A/S)
	Troels V. Christensen (H. Lundbeck A/S)

DTU Chemical Engineering
Department of Chemical and Biochemical Engineering

Preface

This dissertation is the result of 3 years of research conducted in cooperation between the Technical University of Denmark (DTU) and the pharmaceutical company H. Lundbeck A/S. The project took place between September 2014 and September 2017. Most of the laboratory work was conducted in the center for Combustion and Harmful Emission Control (CHEC) at DTU Chemical Engineering, except for a 6 months research stay at Massachusetts Institute of Technology (MIT) in Prof. Allan S. Myerson's research group.

This work would not have been possible without the invaluable support from a large team of advisors and co-workers. First of all, I would like to thank Søren Kiil for his guidance throughout both my master and my PhD, and for always finding time to discuss new ideas and provide feedback. I am also grateful to Kim Dam-Johansen who always cared for my professional development and provided with innovative feedback in our meetings. I consider myself very lucky to have Michael Mealy as a co-supervisor. He made sure that this project was successful and at the same time provided me with valuable feedback for my development as a researcher. Troels Christensen has been a constant source of motivation, and I owe most of my knowledge on the practical aspects of industrial crystallization to his guidance. I would also like to thank Allan Myerson for welcoming me to his research group and for making me feel as one of his full-time students. My experience during the research stay exceeded the best of my expectations, and our discussions were an invaluable source of knowledge and motivation.

I would like to acknowledge the work of my former students Parth Joshi, Alessandro Duso and Shagana Thiyakaran, who made a considerable contribution to this research through hard work and motivation. I will miss our interesting discussions and I hope that you learned from me as much as I learned from you. Also, I would like to thank the DTU technicians Benjamin Petersen and Rasmus Christensen for their valuable support with the equipment design. Their know-how and practical suggestions made the equipment design and construction much simpler than I originally expected.

I am very grateful to the PhD students in CHEC for providing a cozy working environment, and for being one of the best reasons to go to work every day. Even though we have been working in different fields, I truly appreciate our practical discussions and the time we spent together outside work. Furthermore, I believe that Victor Møller, Yashasvi Laxminarayan, Burak Ulusoy and Xueting Wang deserve a special mention for their efforts to understand my research area and provide me with useful feedback at the times when it was most needed.

Considering the distance and my rather urgent requests, I really appreciate the efforts made by my colleagues in Lumsås to provide me with practical information and a rapid solution to the problems faced throughout this project. Special thanks to those in POL for their cooperation with the experimental work, for giving me a spot every time I needed it, and for the interesting tours and updates around the lab facilities.

I can only have gratitude for my colleagues in MIT, who made my research stay an amazing personal and professional experience. Our discussions were invaluable and this work would not have been possible without everything I learned in those 6 months. Special thanks to my office mates for our memorable times outside work and for being a source of motivation towards crystallization research and career development.

Last but not least, I would like to thank my family and friends for their support throughout this journey. I cherish every minute I have spent in Barcelona, Lyngby and Boston, and my life during these three years would not have been the same without all of you. Thank you for your patience and for your unconditional support.

Gerard Capellades Méndez
September 2017

Abstract

The production of Active Pharmaceutical Ingredients (APIs) is conducted primarily in batch processes. This manufacturing approach is reinforced by a patent-driven business model and the need to minimize the process development times for newly patented drugs. However, the regulatory and business environments are now changing. The increasing costs of drug development, combined with the strict regulations and the competition from generic manufacturers, have pushed pharmaceutical companies to seek cheaper and more sustainable production methods.

Transition from batch to Continuous Pharmaceutical Manufacturing (CPM) could lead to significant reductions in the production costs and an improved consistency of the product quality. As a result, development of such processes has received a significant interest in the past decade. To be able to compete in a patent-driven industry with relatively small annual production rates, CPM should be conducted in versatile units that offer short process development times and can be used for production of different compounds.

This PhD project deals with the development of novel crystallizer configurations and process design methods oriented to the crystallization of APIs with strict requirements for the control of crystal size and shape. The project includes the development of methods for the early assessment of crystal quality and the evaluation of techniques for improved control of crystallization kinetics in continuous systems.

In the first block of the PhD, a two-stage continuous Mixed Suspension Mixed Product Removal (MSMPR) crystallization setup was designed for the production of an API presenting elongated crystals. A step by step characterization was applied based on image analysis of the crystallization magma, from which the effects of process conditions on crystal size and shape were evaluated. Crystal breakage was found to be highly selective for a single crystal plane, leading to a significant broadening of the crystal shape distribution. This behavior was consistent with the observations in full-scale batch production, where the crystallization product is subject to significant mechanical stress in downstream processing. The attainable regions for the MSMPR cascade were obtained through a population balance model that is based on the real crystal dimensions obtained from image analysis. Finally, the crystallizer was optimized for a crystal dimension that is consistent through a moderate degree of crystal breakage during downstream processing.

The second block of the PhD involves a fundamental study of the effect of gas dispersion on crystal nucleation kinetics. It is frequently stated in the literature that the presence of an inert gas in a crystallizer can have an impact on crystallization kinetics, either via an improved mass transfer in the crystallizing suspension or by promoting heterogeneous nucleation. These statements are supported by a variety of studies in batch mode. However, the mechanisms are not yet fully understood. In this thesis, the effect of injecting a saturated gas on batch crystallization kinetics has been evaluated from experimental induction times. Combining induction time statistics with a detection method based on sample turbidity, the average time for crystal formation is separated from a detection delay that is a function of the rates of secondary nucleation and crystal growth. Results show a consistent 5-fold reduction in the detection delay for two model systems, and an effect on primary nucleation that is sensitive to the gas injection rate and the studied solute. These results indicate that the induction time reductions frequently reported in the literature could actually be a consequence of a faster crystallization rate after the first nuclei is formed. The mechanism behind these observations is presumably related to a significant improvement in the mixing pattern and intensity.

A novel continuous crystallizer design based on self-induced gas dispersion is presented and evaluated in the last block of the PhD. The objective was to evaluate if gas dispersion could be used to generate smaller crystals in an MSMPR crystallizer, as well as to further develop the understanding of the effect of a moving gas on secondary nucleation and crystal growth. The effect of gas dispersion on crystallization yield and crystal size distribution has been evaluated for a configuration that would be expected in an implemented process, and for operating conditions that are already optimized for the generation of small crystals. Results show that, in contrast with the observations in batch crystallizers, the effect of gas dispersion in a well-mixed MSMPR crystallizer is very limited. Further studies on the effect of impeller speed revealed that crystallization kinetics are not sensitive to variations in the mixing intensity for conditions that meet the requirements for homogeneous three-phase mixing. Results from this study further support the hypothesis that a moving gas phase is an alternative to promote different mixing conditions and demonstrate the limited applicability of this technique in a continuous MSMPR crystallizer.

Dansk resumé

Produktionen af aktive farmaceutiske ingredienser (API'er) udføres primært i batchprocesser. Denne fremstillingsmetode styrkes af en patentdrevet forretningsmodel og behovet for at minimere procesudviklingstiderne for nyligt patenterede lægemidler. Dog er de lovgivningsmæssige og erhvervsmæssige miljøer ved at ændre sig nu. Stigende omkostninger ved lægemiddeludvikling kombineret med strenge regler og konkurrencen fra generiske producenter har presset lægemiddelvirksomhederne til at søge billigere og mere bæredygtige produktionsmetoder.

Overgang fra batch til kontinuerlig farmaceutisk produktion kan føre til betydelige reduktioner i produktionsomkostningerne og mere pålidelig produktkvalitet. Som følge heraf har udviklingen af sådanne processer haft en betydelig interesse i det seneste årti. For at være i stand til at konkurrere i en patentdrevet industri med relativt små årlige produktionshastigheder, bør kontinuerlig produktion udføres i alsidige enheder, der tilbyder korte procesudviklingstider og kan bruges til produktion af forskellige medicinale produkter.

Dette ph.d.-projekt beskæftiger sig med udvikling af nye krystallisatorkonfigurationer og procesdesignmetoder med hensyn til krystallisering af aktive farmaceutiske ingredienser med strenge krav til styring af krystalstørrelse og form. Projektet omfatter udvikling af metoder til tidlig vurdering af krystalkvalitet og evaluering af teknikker til forbedret kontrol af krystalliseringskinetik i kontinuerlige systemer.

I den første blok af ph.d.-studiet blev en to-trin kontinuerlig blandet suspension og blandet produkt fjernelse (MSMPR) -krystallisation designet til fremstilling af en API, der producere aflange krystaller. En trinvis karakteriseringsmetode blev anvendt baseret på billedanalyse af krystallisationsmagma, hvorfra virkningerne af procesbetingelser på krystalstørrelse og form blev evalueret. Krystalbrydning viste sig at være yderst selektiv til et enkelt krystalplan, hvilket førte til en betydelig udvidelse af krystalformfordelingen. Denne adfærd var i overensstemmelse med observationerne i fuldskala batchproduktion, hvor krystalliseringsproduktet er underlagt væsentlig mekanisk belastning ved downstream behandling. De opnå regioner for MSMPR-kaskaden blev opnå gennem en populationsbalancemodel, der er baseret på de reelle krystaldimensioner opnå ved billedanalyse. Endelig blev krystallisatoren optimeret til en krystaldimension, som er konsekvent gennem en moderat grad af krystal brydning under downstream behandling.

Den anden blok af ph.d.-studiet indebærer en grundlæggende undersøgelse af effekten af gasdispersion på kimdannelse kinetik. Det fremgår ofte af litteraturen, at tilstedeværelsen af en inert gas i en krystallisator kan påvirke krystallisationskinetikken enten via en forbedret masseoverførsel i krystalliseringssuspensionen eller ved at fremme heterogen kimdannelse. Disse udsagn understøttes af en række undersøgelser i batch mode. Imidlertid er mekanismerne endnu ikke fuldt ud forstået. I denne afhandling er effekten af at injicere en mættet gas på batchkrystallisationskinetik blevet evalueret fra eksperimentelle induktionstider. Ved at kombinere induktionstidsstatistikker med en detekteringsmetode baseret på prøvesturbiditet, adskilles den gennemsnitlige tid for krystaldannelse fra en detekteringsforsinkelse, som er en funktion af hastigheden af sekundær kimdannelse og krystalvækst. Resultaterne viser en konsekvent 5-ganges reduktion i detekteringsforsinkelsen for to modelsystemer og en virkning på primær kimdannelse, som er følsom over for gasinjektionshastigheden og det undersøgte opløste stof. Disse resultater viser, at induktionstidsreduktioner, der ofte rapporteres i litteraturen, rent faktisk kunne være en konsekvens af en hurtigere krystallisationshastighed, efter at de første kerner er dannet. Mekanismen bag disse observationer er formodentlig relateret til en signifikant forbedring i blandemønsteret og intensiteten.

Et nyt kontinuerligt krystallisationsdesign baseret på selvinduceret gasdispersion præsenteres og evalueres i den sidste blok af ph.d.-projektet. Målet er at vurdere, om gasdispersion kan anvendes til at frembringe små krystaller i en MSMPR-krystallisator samt at udvikle forståelsen af effekten af en bevægende gas på sekundær kimdannelse og krystalvækst. Virkningen af gasdispersion på krystallisationsudbytte og krystalstørrelsesfordeling er blevet evalueret for en konfiguration, der ville forventes i en implementeret proces og for driftsbetingelser, som allerede er optimeret til dannelse af små krystaller. Resultater viser, at i modsætning til observationerne i batchkrystallisatorer er virkningen af gasdispersion i en velblandet MSMPR-krystallisator meget begrænset. Yderligere undersøgelser af effekten af blandingshastigheden afslører, at krystallisationskinetikken ikke er følsom over for variationer i blandingsintensiteten for betingelser, som opfylder kravene til homogen trefase-blanding. Resultater fra denne undersøgelse understøtter endvidere hypotesen om, at en strømmene gasfase er et alternativ til at fremme forskellige blandingsbetingelser og demonstrere den begrænsede anvendelighed af denne teknik i en kontinuerlig MSMPR-krystallisator.

Contents

List of figures

List of tables

Abbreviations and symbols

Abbreviations:

ACS	American Chemical Society
AISI	American Iron and Steel Institute
API	Active Pharmaceutical Ingredient
CCDC	Cambridge Crystallographic Data Centre
CHEC	Center for Combustion and Harmful Emission Control
CLD	Chord Length Distribution
CPM	Continuous Pharmaceutical Manufacturing
CSD	Crystal Size Distribution
CSTR	Continuous Stirred Tank Reactor
DAD	Diode Array Detector
DTU	Technical University of Denmark
EMA	European Medicines Agency
FBRM	Focused Beam Reflectance Measurement
FDA	United States Food and Drug Administration
GCI	Green Chemistry Institute
GI	Gastrointestinal tract
GMP	Good Manufacturing Practice
HCl	Hydrogen chloride
HD	High Definition
HELOS	Helium-Neon Laser Optical System
HPLC	High-Performance Liquid Chromatography
IA	Image Analysis
ICH	International Conference on Harmonization of Technical Requirements for Registration of Pharmaceuticals for Human Use

MEC	Minimum Effective Concentration
MIT	Massachusetts Institute of Technology
MSMPR	Mixed Suspension Mixed Product Removal crystallizer
MTC	Minimum Toxic Concentration
NBE	New Biological Entity
NME	New Molecular Entity
PAT	Process Analytical Technology
PTFE	Polytetrafluoroethylene
PVC	Polyvinyl chloride
PVM	Particle Vision and Measurement
QA	Quality assurance
QC	Quality control
RH	Relative humidity
R&D	Research and Development
SEM	Scanning Electron Microscopy
TCA	Tricyclic antidepressant
US / USA	United States of America
USD	United States Dollar
XRD / XRPD	X-Ray Powder Diffraction

Equation symbols:

Latin:

B	Nucleation rate	$m^{-3}s^{-1}$
b	Nucleation rate order for supersaturation	-
C_0	Feed concentration	g/L
C_{ml}	Mother liquor concentration	g/L
C_{sat} (T)	Temperature dependent solubility	g/L
C_{tot}	Total API concentration in the crystallization magma	g/L
E_{ab}, E_b	Activation energy for nucleation	J/mol
E_{ag}, E_g	Activation energy for crystal growth	J/mol
G	Linear crystal growth rate for the characteristic dimension	m/s
g	Growth rate order for supersaturation	-
h	Crystal height	m
j	Nucleation rate order for suspension density	-
k_{b0}	Pre-exponential nucleation rate factor	$m^{-3}s^{-1}$
k_{g0}	Pre-exponential growth rate factor	m/s
k_v	Volumetric shape factor based on the characteristic dimension	-
L	Size of the characteristic crystal dimension	m
l	Crystal length	M
M_T	Suspension density in the MSMPR crystallizer	g/L
$M_{T,exp}$	Experimental suspension density in the MSMPR crystallizer	g/L
n (L)	Population density of crystals with size L	$m^{-3}m^{-1}$
n^0	Population density of zero-sized nuclei	$m^{-3}m^{-1}$
n_{exp} (L)	Experimental population density of crystals with size L	$m^{-3}m^{-1}$
P(t)	Probability of detecting crystals at time t	-
Q	Volumetric flow rate	m^3/s
R	Gas constant (8.314 $Jmol^{-1}K^{-1}$)	$Jmol^{-1}K^{-1}$
Re	Reynolds number	-

s	Impeller speed	min^{-1}
t	Time	s
T	Temperature	°C or K
t_d	Detection delay	s
V	Crystallizer volume	m^3
V_c	Volume of a single crystal	m^3
vol (L)	Volume fraction of crystals sharing a characteristic size L	-
vol(w)	Volume fraction of crystals sharing a characteristic width w	-
w	Crystal width	m
$w_{4,3}$	Mass-based mean crystal width	m

Greek

ΔL	Channel size for a distribution based on the dimension L	m
ΔV	Variation in the crystallizer volume during withdrawal	m^3
Δw	Channel size for the crystal width distribution	m
θ	Parameter vector	-
ξ	Total number of independent induction time experiments	-
ξ'(t)	Number of detected nucleation events at time t	-
ρ	Density of the crystalline phase	g/L
σ	Supersaturation defined as $(C_{ml}-C_{sat}(T)/C_{sat}(T))$	-
τ	Residence time	s
τ_{ind}	Induction time	s
τ_{tot}	Total residence time in the MSMPR cascade	s

1

Introduction

In a pharmaceutical drug, the Active Pharmaceutical Ingredient (API) is the substance that holds the medical function. These products are subject to strict requirements from health authorities to ensure that the given drug will be stable and deliver the appropriate systemic effects. The solid state properties of an API will have a major impact on its dissolution rate and, consequently, on the extent and duration of the medicine's effect. In this context, crystallization is one of the most common unit operations in pharmaceutical production, responsible for delivering crystalline APIs within the required solid state quality.

In a context where drug development is becoming increasingly expensive and the competition from generic manufacturers keeps increasing, research-based pharmaceutical companies have turned focus to cheaper, more sustainable production methods. In this area, continuous pharmaceutical production has received a significant interest during the past decade. To get the full benefit from continuous production and at the same time fit in a patent-driven industry where short development times are a priority, continuous pharmaceutical processes have to be simple and utilize flexible equipment.

Continuous stirred tank crystallizers, normally falling in the Mixed Suspension Mixed Product Removal (MSMPR) crystallizer formalism, are arguably the most common choice for continuous pharmaceutical crystallization. Their capacity for handling concentrated suspensions and long residence times, combined with the simplicity of process development, is only obstructed by the product and process constraints that limit the attainable product quality. Especially when small crystals are required, simply changing the process conditions is often not sufficient, and dealing with large supersaturations tends to be infeasible.

In addition to the equipment limitations for the generation of small crystals, traditional methods for MSMPR process development are based on crystal size determination techniques that give poor information on the crystal shape. Especially for elongated particles that tend to break in downstream processing, the crystal size distribution as assessed during the crystallization process will be heavily different than that at the formulation product. Thus, there is a need for the development of novel characterization approaches that simultaneously account for the size and shape of the crystals, not only for fragile crystals, but also for those compounds that exhibit different crystal habits during crystallization process development.

1.1 Objectives

This project has been conducted in close cooperation between the Technical University of Denmark and the pharmaceutical company H. Lundbeck A/S. It has been structured to be academically relevant and satisfy the industrial needs for the development of a given continuous process. The project works around Melitracen hydrochloride, a relevant compound from Lundbeck's production that not only exhibits a challenging crystal habit, but it is also subject to strict requirements for the generation of small crystals. The objectives of this PhD project have been summarized below:

- Provide a proof-of-concept for the continuous crystallization of Melitracen hydrochloride, including an assessment of the crystallizer configuration and the optimal set of operating conditions.
- Investigate the application of novel approaches for the characterization of MSMPR crystallizers, allowing for a simultaneous assessment of crystal size and shape during process development.
- Investigate into novel methods for crystal size distribution control in MSMPR crystallizers, with special focus on the generation of small crystals at lower supersaturations.

1.2 Hypotheses

To address the aforementioned objectives, this thesis has been divided in two main blocks. The first block involves the application of image analysis for the characterization of MSMPR crystallizers. Despite similar methods have been used before, a step-by-step characterization using modern methods for MSMPR process development is yet to be applied. This characterization can either be conducted entirely by image analysis or by correlating *in situ* Focused Beam Reflectance Measurements (FBRM) to the real crystal dimensions.

The second block of the PhD study investigates the effect of gas dispersion on crystallization kinetics, particularly for the promotion of nucleation rates. Most of the methods to obtain small crystals in MSMPR crystallizers are based on promoting nucleation in a local, high energy point. Normally employing milling or ultrasonication, the considerable mechanical stress applied to that point promotes crystal breakage and secondary nucleation. Despite these techniques are effective for obtaining small crystals, they usually come with additional concerns for energy dissipation, safety and product quality.

The impact of system fluid dynamics on secondary nucleation is already well-known. Variations in the impeller type, speed and even on the vessel configuration lead to different kinetics and thus variations in the crystal size distribution. While contact secondary nucleation relies on a minimum impact energy, it is clear that methods based on milling and ultrasonication surpass this energy to the point of inducing variations in crystal shape and, in some cases, structure. In this thesis, it is hypothesized that gas dispersion could induce variations in the flow pattern inside the crystallizer, thus promoting crystal collisions and secondary nucleation without the need for unreasonably high supersaturations. In contrast with methods that are based on a local, high energy point, gas dispersion would be significantly gentler, more scalable, versatile, and affect the entire active crystallization volume. Thus, instead of having extremely high nucleation rates at a single point, this method would give a smaller, but widespread promotion of the rate of crystal formation. Alternatively, the presence of the gas-liquid interphase or the perturbations from gas injection could promote heterogeneous nucleation in the crystallizer. This hypothesis is supported by previous studies that reported significant reductions in crystallization induction times in batch crystallization. However, because the formation of a primary nucleus with gassing has never been observed directly, it is yet to be known if the smaller induction times are a result of a higher rate of primary nucleation or a faster crystallization rate after the first nucleus is formed. An insight into the mechanism could thus give critical information for the design of novel crystallization configurations.

1.3 Structure of this thesis

The rest of this thesis has been divided into 6 chapters. The contents of each chapter are summarized below:

- **Chapter 2** is a critical literature review describing the background for this project. The relevant theory for the understanding of this thesis is provided, together with practical examples that support the motivation for the research and show the limitations of the state-of-the-art.
- **Chapter 3** includes the preliminary studies conducted to select an appropriate solvent and crystal size determination technique for the Melitracen hydrochloride case. Although most of the contents are oriented to industrial process development, the chapter ends with an experimental demonstration of the limitations of FBRM that support a need for the development of novel characterization strategies.
- **Chapter 4** provides a proof-of-concept for the crystallization of Melitracen HCl employing quantitative image analysis. A two-stage MSMPR crystallization cascade was characterized using quantitative image analysis, from which the source and

extent of crystal breakage were evaluated. Mathematical modelling of the MSMPR cascade allowed assessing the optimal number of stages and crystallization conditions to obtain crystals with a similar size than those currently used in formulation.

- **Chapter 5** describes a fundamental study on the effect of a flowing gas on nucleation kinetics. Induction time statistics were applied to separate the time for formation of the first nucleus from a detection delay related to the rate of crystallization after the first nucleation event. This study demonstrates not only that the rate of crystallization can be promoted with a flowing gas, but also that this promotion occurs beyond primary nucleation. This behavior was observed for two model systems at conditions where crystallization kinetics could be promoted by mixing.
- **Chapter 6** includes the design of a novel, flexible MSMPR crystallizer that utilizes the impeller rotation to disperse gas from the headspace into the crystallization magma. The effects of gas dispersion studied in Chapter 5 were evaluated for a crystallizer design that is already optimized to generate small crystals. Results showed that, for the mixing intensities that allow for three-phase mixing, the rate of crystallization cannot be significantly promoted by gas dispersion or mixing.
- **Chapter 7** summarizes the academic and industrial conclusions from this thesis, and describes a set of suggestions for future work.

2

Background

This chapter is aimed to locate the reader in the field of this thesis, providing the necessary knowledge to understand the motivation for the research as well as the achievements and limitations of the state-of-the-art. A more specific literature review will be provided in the introduction of the manuscript chapters.

2.1 Continuous pharmaceutical manufacturing

2.1.1 The patent-driven pharmaceutical industry

The pharmaceutical market is dominated by the competition between research-based companies and generic manufacturers. The main competitive edge of the first has traditionally been innovation in drug development. However, discovery and development of new drug compounds is an expensive process, where high drug failure rates contribute significantly to the total R&D costs. As it was estimated by the Tufts Center for the Study of Drug Development in 2016, the capitalized pre-approval costs of drug development per approved drug is currently at the order of 2.588 billion USD with an estimated clinical success rate of 11.83%.[1]

The elevated costs of drug development are barely compensated with the discovery of a new entity. A patent application for a promising drug candidate is normally filed early on in the process, while the development of a new drug typically takes 10-15 years.[2] Consequently, about half of the patent life is spent before the product can be launched. Moreover, due to the intense competition from generic manufacturers, it is possible for the original manufacturer to lose up to 90% of their market share within a year after the patent expires.[3] Considering the significant costs of drug development and the relatively short patent protection times, a rapid process development is of utmost importance to maximize the time between product release and patent expiration.

2.1.2 Transition to continuous production

Pharmaceutical production is traditionally conducted in batch mode. This approach comes from the need for a simple and rapid process development and is further supported by the low annual production rates in this industry. The campaign-based production relies on equipment flexibility and requires significant expertise in logistics and production management. The use of multipurpose facilities combines well with the patent-driven approach to this industry, where new products are constantly developed and require a rapid release to the market. However, with an increased pressure for cost reduction and the drive to increase sustainability, pharmaceutical companies are looking towards novel production methods that provide with increased productivity, waste reduction and increased control over product quality.

One of the main driving factors for the transition to continuous manufacturing is the increasing drug development costs relative to the success of drug discovery. Figure 2.1 shows the yearly amount of approved New Molecular Entities (NME) and New Biological Entities (NBE), related to the estimated total expenditures in drug development in the U.S. for the past 53 years.

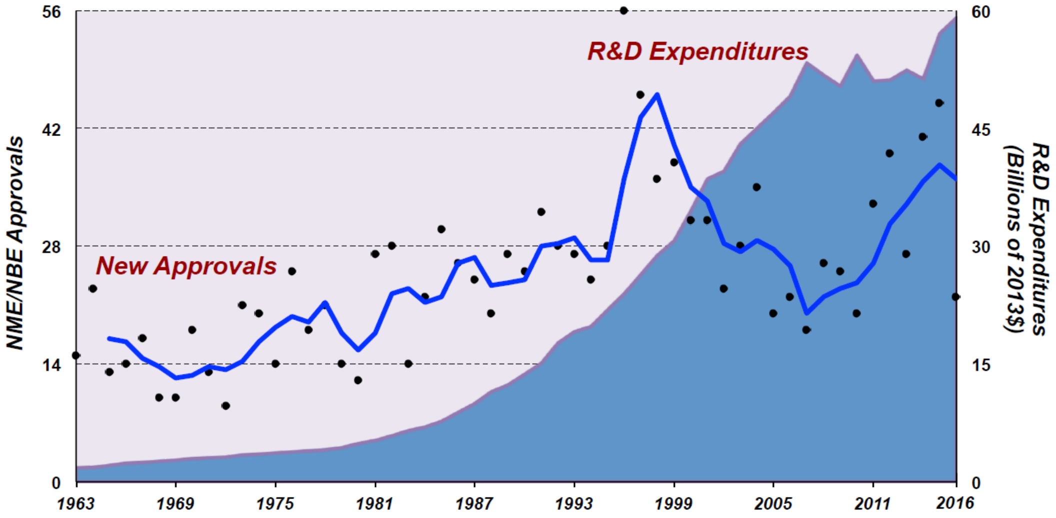

Figure 2.1 New compound approvals and pharmaceutical R&D expenditures (adjusted for inflation) in the United States from 1963 to 2016. The trend line is a 3-year moving average for NME/NBE approvals.[1] [Provided by and used with permission from the Tufts Center for the Study of Drug Development, Tufts University School of Medicine, USA]

While the investments in R&D have increased considerably since the 1980s, the rate of drug discovery has become stagnant. The increased costs of drug development are partially responsible for the merging and failure of a large number of companies invested in drug innovation,[4] and led to a sharp decline in the annual growth rate of the larger pharmaceutical manufacturers.[5] This trend encouraged pharmaceutical companies to seek a reduction in the manufacturing costs, which typically represent 30% of the total costs in an average pharmaceutical company.[6,7] In this context, transition to continuous production is seen as one of the most promising solutions.[8]

On top of the increased drug development costs, the strengthened environmental policies reinforce the need for novel production methods with improved waste management and safety. In 2005, a Pharmaceutical Roundtable was established by the American Chemical Society (ACS), the Green Chemistry Institute (GCI) and several global pharmaceutical companies. The objective was to encourage the integration of green chemistry and engineering into the pharmaceutical industry. Few years after, the Roundtable released a list of key green engineering research areas as a result of brainstorming and prioritization exercises.[7] The use of continuous processing topped the list, followed by bioprocesses and improved separation and reaction technologies.

Because of the intense demands for consistent product quality, the licensing authorities are also supporting the implementation of continuous processes combined with in-line quality assurance through the application of Process Analytical Technology (PAT) tools.[9–11] Batch processes are still poorly understood and the current manufacturing approach is characterized by a lack of robustness in product quality. Because of the large amounts that are manufactured in a single campaign, a defective batch can lead to a sudden drug shortage and a significant revenue loss for the pharmaceutical company.[12–14]

Continuous processes enable the use of smaller and safer equipment, in-line monitoring of process conditions and real-time product release with consistent quality. In addition, the amount of waste is reduced as recycle streams are handled more efficiently.[3,8,15,16] In contrast with the production of bulk chemicals, continuous pharmaceutical synthesis can usually be attained using tank reactors at the 10 liter scale or in a set of microreactors in parallel.[16–18] This is an enormous advantage over the scale-up limitations of batch processes, since the process development could be conducted directly in full-scale units or simplified by numbering-up instead of scaling-up.[18,19] Furthermore, smaller units generally facilitate the attainment of homogeneous reaction conditions as well as an excellent control over reaction temperature, being a great benefit for handling highly exothermic reactions that would otherwise be impossible in batch mode.[18,20]

Continuous pharmaceutical manufacturing has raised a considerable interest from both academic institutions and industrial manufacturers in the past decade. This led to significant advances in the development of small continuous units that culminated with the development of end-to-end continuous pharmaceutical manufacturing systems. In 2013, the Novartis-MIT Center for Continuous Manufacturing presented the first example of an end-to-end integrated continuous manufacturing plant for the API aliskiren hemifumarate, demonstrating a reduction in processing time from 300 h in batch manufacturing to a process residence time of 47 h in continuous mode.[21] More recently, a compact, reconfigurable continuous system based on flexible modules was presented for the end-to-end manufacture of a wide variety of pharmaceuticals.[22] Although it is not the intention to replace continuous manufacturing with this system, it is a potential solution to unexpected disease outbreaks and the aforementioned drug shortages in batch production, and it puts in practice the first plug-and-play solution for continuous pharmaceutical manufacturing.

2.2 API quality from a solid state perspective

The International Conference on Harmonization of Technical Requirements for Registration of Pharmaceuticals for Human Use (ICH) defines quality as "The suitability of either a drug substance or drug product for its intended use. This term includes such attributes as the identity, strength, and purity".[23] When it comes to APIs, quality can be partially assessed from their crystal size, shape, form and purity.[23,24] Some of these properties will have a direct impact in the product compressibility, melting point and bulk density, which will in turn impact the powder manufacturability. From a medical perspective, the solid state properties will affect the drug's bioavailability and stability.

The bioavailability is defined as the proportion of the drug that is absorbed and available to produce systemic effects.[25] Several parameters including drug dosage are based on a given bioavailability that must be ensured through API production and formulation. A tablet that is administered orally needs to go through a disintegration process followed by API dissolution before the drug is absorbed into the bloodstream. While disintegration can be assisted by the use of excipients, API dissolution is highly dependent on its crystal structure and crystal size distribution (CSD). The plasma concentration profile will result from the kinetic competition between drug absorption and its elimination. This concept has been illustrated in Figure 2.2.

The effectiveness of a drug is related to a therapeutic range, defining the plasma drug concentrations that should be attained through control of the absorption kinetics. Some drugs will be administered for a fast onset of action, while others will be tailored to a more delayed but prolonged effect.[26] The Minimum Effective Concentration (MEC) defines the lower end of the therapeutic range, below which the drug concentration is not sufficient to produce a therapeutic effect. The Minimum Toxic Concentration (MTC) falls at the upper end of the therapeutic range and defines the concentration value above which the drug reached its toxicity level.[27] Since the drug dosage is based on a predefined bioavailability that depends on the dissolution rate of the API, the administration of an API with the wrong crystal structure or crystal size distribution could pose a serious threat for the health of the patient.

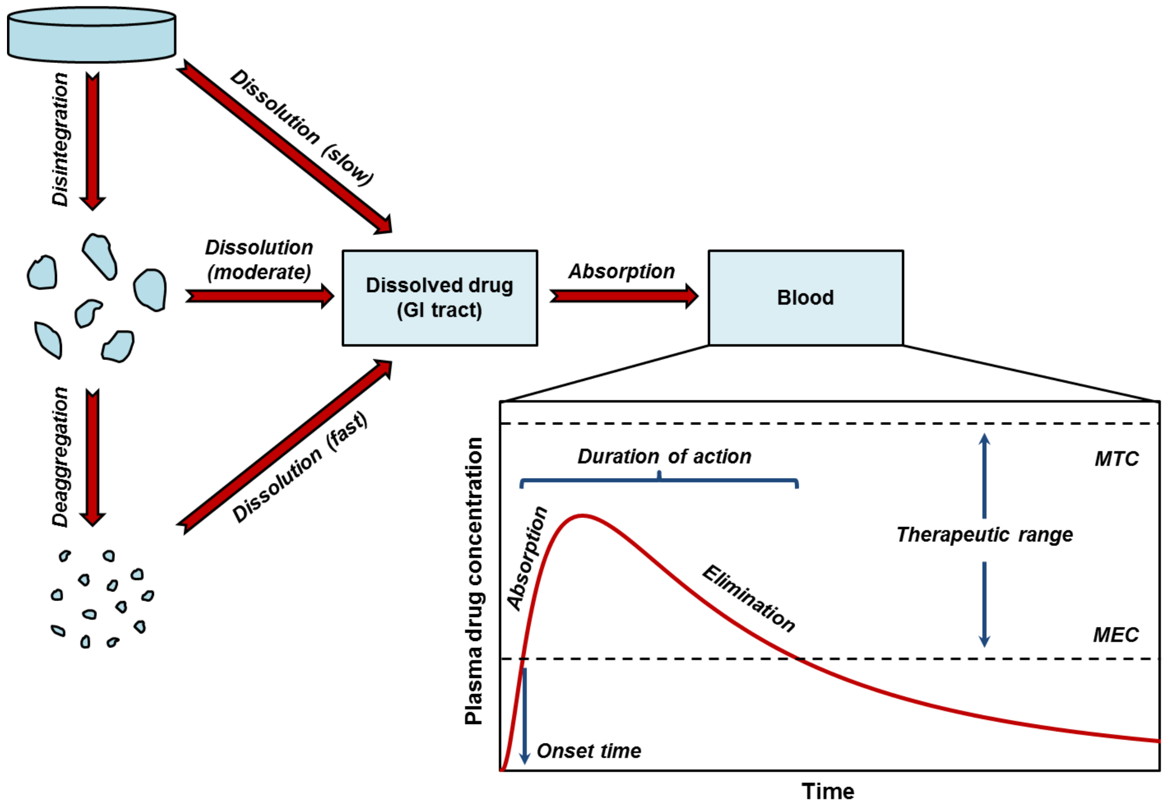

Figure 2.2 Mechanisms of drug absorption from oral administration, and the impact of dissolution/absorption kinetics on the plasma drug concentration profile.

Similarly, the stability of a drug depends on the crystal structure of the API, which is not necessarily administered in the most stable form. Some drugs with poor water solubility are administered in metastable crystal forms or even as amorphous solids to enhance their dissolution rate.[28,29] In other cases, obtaining the most stable polymorph might not be efficient for a crystallization process. Since recrystallization of the formulated API could lead to a complete change in the physical properties and bioavailability, ensuring polymorphic purity is of utmost importance for the formulated drug.

2.3 Practical aspects of crystallization kinetics

Despite the availability of alternative particle technologies for the control of bioavailability and drug stability,[28] crystallization is a necessary unit operation that defines most of the solid state properties of the active ingredient. Crystallization process development starts with knowledge on the different mechanisms that induce crystal formation and is based on a deep understanding on how the kinetics of nucleation and crystal growth impact the quality of the crystallized product.

Crystallization from solution can be thought as a two-step process, starting from the formation of a new crystal (nucleation) and followed by the growth of the crystal to larger sizes.[30] In this section, a short overview of nucleation and growth kinetics will be given from a perspective of crystal quality control.

2.3.1 Nucleation

Nucleation is the commencement of a new phase, and thus it plays a decisive role in determining the crystal form and size distribution.[31] There are two major distinctions for the classification of nucleation mechanisms: primary and secondary nucleation.

2.3.1.1 Primary nucleation

Primary nucleation occurs without the assistance of solute crystals, and thus it is the mechanism that starts crystallization in unseeded solutions. A primary nucleus can either be formed from the bulk solution (homogeneous nucleation) or facilitated by a foreign surface (heterogeneous nucleation). The main difference between the two relies on the activation energy for crystal formation. The presence of an external surface provides with a significant reduction in the activation energy. Consequently, heterogeneous nucleation is the predominant mechanism in unseeded solutions, to the point that homogeneous nucleation rarely occurs in practice.[30] The fundamental mechanisms of crystal formation in a molecular level have been a discussed topic for several years, although they fall out of the scope of this thesis. More information can be found elsewhere.[32–35]

From a kinetic perspective, the formation of a primary nucleus is a stochastic process that depends on the composition of the supersaturated solution as well as on temperature, supersaturation degree and the concentration and nature of the provided external surfaces.[35–39] Primary nucleation can also be triggered by perturbations in the supersaturated solution, including those from mixing or physical manipulation of the sample.[40–42] Because of its stochastic nature, and since new crystals can only be detected after they have grown to a certain size, the study of primary nucleation has always been a challenge.[31,43] However, given the appropriate statistical tools, studies on primary nucleation are an excellent method to study the effect of process conditions and external surfaces on crystal formation.

2.3.1.2 Secondary nucleation

Secondary nucleation occurs with the assistance of solute crystals, and thus it is heavily dependent on the suspension fluid dynamics. Early studies demonstrated that the rate of secondary nucleation is a function of the frequency and intensity of collisions on the parent crystals.[44–48] Even though the mechanism is not yet fully understood, the hypotheses can be englobed in two categories depending on whether the nuclei come from the parent crystal or from the surrounding solution.[30]

The concept of a fluidized layer of supersaturated solution near the parent crystal was introduced by Powers in 1963.[49] It was hypothesized that a layer of semiordered clusters of solute molecules surrounding the crystal, rather than the crystal itself, could be a source of secondary nuclei. A later study by Clontz and McCabe demonstrated that low energy crystal contact was able to trigger nucleation from a growing crystal. The frequency of nucleation was dependent on contact force and supersaturation. Different studies have been conducted to elucidate the mechanism since then, many supporting that secondary nucleation is purely a consequence of microattrition.[48,50–53] In a recent study, Cui and Myerson realized that most of the studies where secondary nucleation had been detected without visible damage in the parent crystal used relatively small contact forces. In their study,[54] they took advantage of the unique polymorphism behavior of glycine to investigate further on the source of secondary nuclei. Applying different contact forces to a γ-glycine crystal (most thermodynamically stable form), they found that contact forces below 2 N would only produce crystals of α-glycine. As the contact force was increased, crystals of both polymorphs were formed. Since fragments of the parent crystal would still retain the same crystal structure, it was concluded that the formed α-glycine crystals came from the solution phase as a result of the applied contact force.

A secondary mechanism based on mild contacts has an important implication for crystal size distribution control in stirred tanks, as variations in the system fluid dynamics can easily lead to a variations in the nucleation rate. Because secondary nucleation relies on contact, the secondary nucleation rate depends on solids concentration, crystal size, supersaturation and stirring speed in the crystallizer.[55] Consequently, nucleation rate equations for stirred tank crystallizers usually involve terms for suspension density and impeller speed in addition to the supersaturation and temperature dependencies.[56]

In a stirred tank, the dominant mechanism depends on the supersaturation level and the energy required for secondary nucleation.[56] This has been illustrated in Figure 2.3.

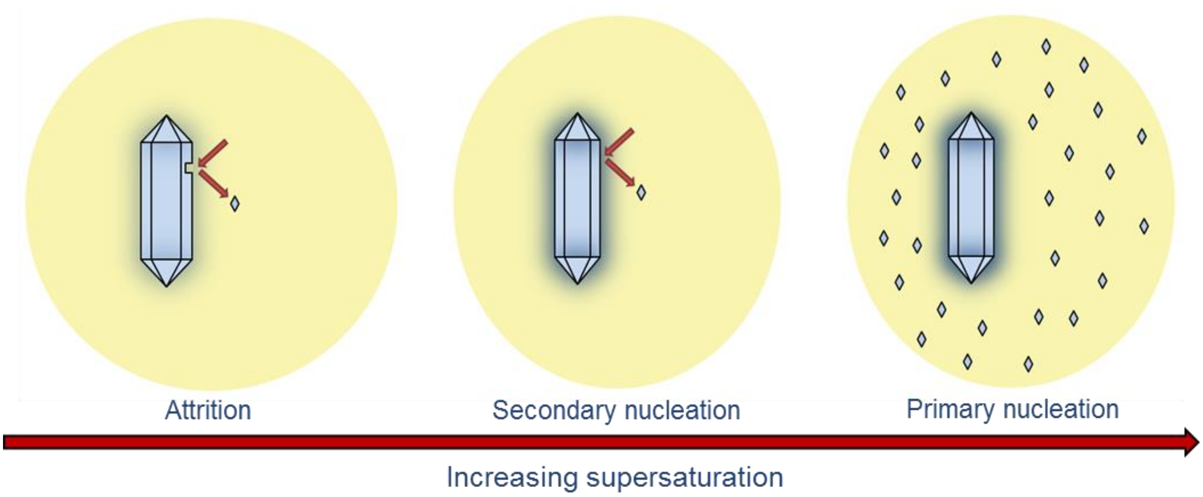

Figure 2.3 Nucleation mechanisms in a stirred tank based on supersaturation level, including Power's concept of a reservoir layer near the crystal surface.[49,56]

Because of yield requirements, practical constraints and the desire for fouling prevention, stirred crystallizers tend to operate at the lower end of supersaturation. Thus, most of the methods for size distribution control based on nucleation enhancement operate by increasing the rates of secondary nucleation or by triggering primary nucleation in a local point. More information on these methods will be provided in Section 2.6.

2.3.2 Crystal growth

Crystal growth occurs from the addition of solute molecules from the supersaturated solution to the surface of a crystal. Since the crystal grows in different directions simultaneously, there is no single definition for the crystal growth rate. This phenomenon can be studied as the linear growth velocity of a certain crystal face, as the overall gain in crystal mass, or as the variation on a characteristic dimension related to the crystal volume or surface area (e.g. equivalent sphere diameter).

The growth of a crystal consists of an initial diffusion step followed by a surface reaction step.[56] Especially for static systems and poorly mixed crystallizers, the growth rate can be dominated by transport phenomena rather than by surface incorporation. In those cases, increased agitation intensities lead to a faster rate of crystal growth. When a growth cluster reaches the surface of a crystal, it must shed its layer of solvent and bond with that surface. Because of the larger surface for the stabilization of the incoming cluster, growth tends to occur at crystal defects and kinks. At high supersaturations, crystal growth can occur after formation of two-dimensional nuclei at the surface of the crystal. Thus, the crystal growth rate is dominated by the generation of steps in the flat crystal faces, either by dislocation or by 2D nucleation. More information on the crystal growth theories and mechanisms can be found elsewhere.[39,57,58]

One of the important quality attributes of crystalline products is their crystal habit, as it will impact not only the further downstream process but also the dissolution rate of the solid phase. The external appearance of a crystal is a function of its internal structure and the conditions at which the crystals are grown, including composition of the liquid phase and the rate of crystal growth.[30,57] Crystals with the same structure have shown completely different crystal habits depending on the growth conditions, and thus the validation of a consistent crystal habit is an important part in the development of crystallization processes.[59–62]

Two additional phenomena have to be considered in the design of crystallization processes: size-dependent crystal growth and growth rate dispersion. In a suspension, small crystals have a higher effective solubility than the larger ones. This is a consequence of the system trying to reduce its Gibbs free energy by minimizing the total contact area between the crystalline phase and the surrounding solution.[30] This behavior is responsible of additional phenomena including Ostwald ripening, by which smaller particles tend to dissolve and larger particles tend to grow in suspension, even when this suspension is at thermodynamic equilibrium. In a growing suspension, the smaller crystals will have a lower effective supersaturation and, thus, their growth rate will be smaller. However, this mechanism is likely to be significant only for crystals at the sub-micron range.[30] Alternatively, size-dependent growth can be a consequence of the larger crystals having a higher frequency of dislocations because of their larger area, thus increasing their effective growth rate.[30] Size-dependent growth is often confused with growth rate dispersion,[63] by which crystals with the same size on the same suspension grow at different rates. This could be a consequence of crystals growing at different constant rates, or of the growth rate of individual crystals varying with time.[30,64] When crystal growth is investigated for large crystal populations, these mechanisms will lead to a broadening of the crystal size distribution. Their impact on continuous crystallization will be further discussed in the next section.

2.4 The Mixed Suspension Mixed Product Removal (MSMPR) crystallizer

2.4.1 Introduction

Because of the equipment flexibility and their capacity for handling concentrated suspensions and long residence times, continuous crystallization is often conducted in stirred tank reactors (CSTR). These crystallizers follow the Mixed Suspension Mixed Product Removal (MSMPR) formalism, by which the active crystallization volume is perfectly mixed and the properties of the product suspension are the same as those in the crystallizer.[56] Modelling of MSMPR crystallizers is usually simplified with the assumptions of negligible crystal breakage, negligible agglomeration and uniform crystal shape factor throughout the crystallizer magma. Following these assumptions, the crystal size distribution is a direct function of crystallization kinetics and it can be modelled on the basis of a single crystal dimension. In this type of system, the population balance can be reduced to eq 2.1. Details on the derivation can be found elsewhere.[56]

$$V\frac{d(Gn)}{dL} = Q_i n_i - Qn \tag{2.1}$$

Where V represents the active crystallization volume, G is the rate of crystal growth for the characteristic dimension L, Q is the flow rate through the crystallizer and n is the crystal population. The index i indicates which properties correspond to the crystallizer feed.

For systems presenting size-independent crystal growth without growth rate dispersion (i.e. following McCabe's ΔL law[65]), the population balance can be integrated analytically. In a single stage MSMPR crystallizer with clear feed, the integrated population balance equation takes the form of eq 2.2.[56]

$$n(L) = n^0\, exp\left(\frac{-L}{G\tau}\right) = \frac{B}{G} exp\left(\frac{-L}{G\tau}\right) \tag{2.2}$$

Where the residence time τ expressed as Q/V, B is the nucleation rate, G is the linear growth rate in the characteristic dimension and n^0 represents the population of embryo-sized crystals used as boundary condition for the integration.

As expressed in eq 2.2, the crystal population distribution is a direct function of the rates of crystallization and the residence time in the crystallizer. The crystal population will define the steady state suspension density (M_T) from the third moment of the distribution, the density of the crystalline phase ρ and a volumetric shape factor k_v that relates the characteristic dimension to the volume of a crystal.

$$M_T = k_v \rho \int_0^{\infty} L^3 n(L) dL \tag{2.3}$$

Since the rate at which solute is lost from the solution phase is equal to the rate at which mass is gained by the crystalline phase, the supersaturation σ can be expressed as a function of the crystallizer suspension density, accounting for the mass balance in the crystallizer:

$$\sigma = \frac{C_0 - M_T - C_{sat}(T)}{C_{sat}(T)} \tag{2.4}$$

Where C_0 is the feed concentration and $C_{sat}(T)$ is the solubility at the crystallization temperature T.

For a constant feed concentration, temperature and residence time, the steady state is dominated by an internal feedback between crystallization kinetics and the crystal size distribution. The way this feedback interacts with process development has been expressed for a hypothetical system in Figure 2.4, assuming that crystallization kinetics follow semi-empirical power-law equations and that crystallization is conducted by cooling at constant agitation intensity. A more generalized version can be found elsewhere.[56]

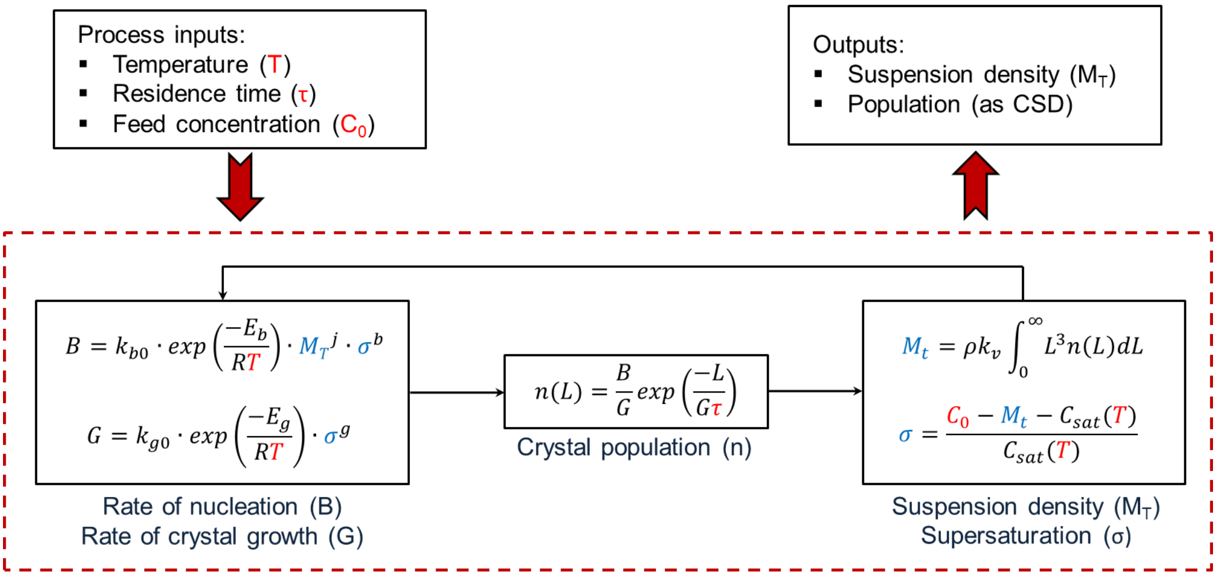

Figure 2.4 Internal feedback between crystallization kinetics and crystal size distribution in a hypothetical cooling MSMPR crystallizer at steady state.

Note that the impact that process conditions have on the steady state crystal size distribution is determined by the solute-solvent system (solubility $C_{sat}(T)$; kinetic parameters k_{b0}, E_b, j, b, k_{g0}, E_g, g; and solid phase properties ρ_c and k_v), which dictates the extent of crystallization and the attainable crystal sizes. For instance, similar orders of nucleation and crystal growth could lead to a mean crystal size that is independent of residence time, thus limiting the capacity of production engineers to control the obtained crystal sizes.[56] Furthermore, selective promotion of one of the two rates (e.g. by ultrasonication) will result on a higher mass deposition and thus a lower operating supersaturation. The resulting smaller driving force from supersaturation will inhibit part of this kinetic enhancement, especially when the mass deposition rate is heavily dependent on supersaturation (high b or g). For the same reason, extending the crystallizer residence time usually leads to a smaller mass deposition rate. After a certain point, considerable prolongations of the residence time have a negligible improvement on the steady state yield (see ref.[66] for an example).

From a process development perspective, the use of mathematical models for optimization of MSMPR crystallizers provides a considerable advantage over an entirely experimental assessment of the optimal crystallization conditions. Especially when the properties of the crystallization magma will depend on several process conditions, experimental screening is time consuming and costly. For this reason, MSMPR crystallizers are normally optimized through prediction models based on semi-empirical kinetic rate equations and the appropriate population and mass balance.

Selection of a population model, as well as the determination of the kinetic rate equations, requires experimental data on the phenomena occurring in the crystallizer (e.g. size-dependent growth, agglomeration, breakage) and the effect of process conditions on crystallization kinetics. The former can be first assessed qualitatively from images of the crystallization product, and later quantitatively from the experimental populations (n_{exp}), calculated from eq 2.5.

$$n_{exp}(L) = \frac{vol(L)M_T}{\rho k_v L^3 \Delta L} \tag{2.5}$$

Where $vol(L)$ is the volume fraction of crystals with characteristic size L, and ΔL is the channel size of the discrete CSD.

If the experimental data follows the assumptions for an ideal MSMPR crystallizer, the experimental population (eq. 2.5) will have the shape of eq. 2.2. Thus, when the population is expressed in the logarithmic form versus crystal size, it will yield a linear plot. One of the most common deviations from an ideal MSMPR crystallizer presents a strong upward curvature in the logarithmic population density plot. Even though this behavior can be a consequence of other phenomena,[30] it is commonly attributed to size-dependent crystal growth.[63] Usually, this behavior is either neglected by fitting the effective nucleation rates (linear extrapolation)[67] or modelled with semi-empirical expressions.[68–72]

With the appropriate design of experiments, the kinetic rate equations in Figure 2.4 can be fitted based on the steady state crystal size distribution of approximately 10 runs to steady state by solving a nonlinear estimation problem.[73,74] These models have also been extended to consider the effect of process conditions on impurity incorporation through the estimation of additional parameters.[75–78] Once the kinetic rate equations have been estimated, prediction models based on crystallization kinetics and the population and mass balances can be used for the assessment of attainable crystal sizes,[74,79,80] optimization of start-up,[81] and determination of the optimal number of stages and operating conditions to control crystal purity, polymorphism and size distribution.[66,74,75,77,82,83] The rapid methods for determination of crystallization rate equations and their extended applicability for process development and control make MSMPR crystallization an excellent choice for a pharmaceutical crystallization process. Nevertheless, it is important to note that the fitted rate equations are based on the method for measuring crystal size distribution, for which the crystal growth rate is related to how the measuring technique “sees” crystal size. Thus, these models predict the crystal size distribution based on the same methods that were used for the acquisition of the experimental CSDs.

2.4.2 Size characterization methods in MSMPR process development

In recent years, size characterization methods have evolved significantly from the use of sieving or coulter counters in crystallization.[84] A large number of techniques are currently available for the measurement of crystal size distributions.[85,86] This section includes a critical review of the two most common methods applied in MSMPR process development: in-line Focused Beam Reflectance Measurements (FBRM) and off-line laser diffraction.

FBRM is a probe-based instrument that is inserted into the crystallizer for *in situ* determination of a chord length distribution (CLD). The instrument uses a rotating monochromatic laser beam directed to the crystallization magma. As the focused beam scans across the particle system, individual particles and structures will backscatter the laser beam to the detector. These distinct pulses of backscattered light are detected, counted, and the duration of each pulse is multiplied by the scan speed to calculate the distance across each particle (chord length). The probe can scan through thousands of particles per second, thus delivering chord length distributions in real time.[87]

Being an in-line method capable to quickly deliver reproducible size distribution data makes FBRM a preferred option as a PAT tool with great potential for crystallization feedback control. Nevertheless, FBRM loses reliability when significantly different process conditions are employed (e.g. during experimental screening in process development). Beyond the measurement sensitivity to probe position and focal point, it has been shown that the measured chord length distribution depends on the sample mixing intensity and in some cases on solids concentration.[88–91] Furthermore, despite the extensive development of correlations and models between chord length distributions and crystal size distribution,[88,92–97] these are situational and mostly based on spherical particles. Because the measured chords belong to different crystal dimensions, the chord length distributions can appear broader for elongated particles, even after square-weighting. This complicates the assessment of the MSMPR assumptions from population functions based on chord length distributions.

It is now common in MSMPR process development to use FBRM to determine the onset of steady state and then measure the crystal size distributions with laser diffraction for the estimation of kinetic parameters. Laser diffraction is highly reproducible and provides a crystal size distribution that is commonly used for validation of crystal quality in the final product.[86] Despite this method being very reliable for spherical crystals and ideal systems, the assessment of crystal size distributions is limited when the crystal shape varies during process development. If the optimal operating conditions are assessed from laser diffraction data, adjusting the process conditions to produce crystals within the required specifications is only valid when crystal breakage in downstream processing is negligible. In those cases, laser diffraction has to be supplemented by imaging techniques and downstream breakage models.

2.4.3 Limits of attainable crystal sizes

In cooling MSMPR crystallizers, the crystal size distribution is commonly controlled through variations in the crystallization temperature, feed concentration, impeller speed and residence time. When reactive or anti-solvent crystallization are employed, the number of theoretical degrees of freedom increases as the solvent composition and reactant surplus can be adjusted to expand the attainable crystal sizes. However, in practice, MSMPR crystallizers are heavily limited for crystal size distribution control. The optimization is subject to various constraints related to equipment limitations, industrial requirements and product specifications.

The use of attainable regions of crystal sizes is probably the most illustrative method to demonstrate the limitations of MSMPR crystallizers when realistic operating constraints are applied. In this area, Vetter *et al.* presented a detailed methodology for the determination of attainable crystal sizes based on known crystallization kinetics.[79,80] Applying this methodology to three case studies including cooling and anti-solvent crystallization, they showed that the attainable crystal sizes can be easily expanded to larger sizes by increasing the number of

MSMPR stages and the total residence time. However, the minimum attainable crystal sizes were independent of these parameters as they were a main function of supersaturation and residence time constraints.

Generating small crystals relies on the use of high supersaturations that, for most systems, promote nucleation kinetics over crystal growth. Nevertheless, the operating supersaturations on a real system will certainly be limited by fouling at the crystallizer and by process yield requirements. Furthermore, product limitations including the attained crystal habit, structure, defect formation, impurity incorporation and prevention of oiling out will affect the maximum attainable supersaturation.[57,62,98] The consequence of defining a maximum supersaturation in the system was investigated by Vetter *et al.* and it is displayed in Figure 2.5.[80]

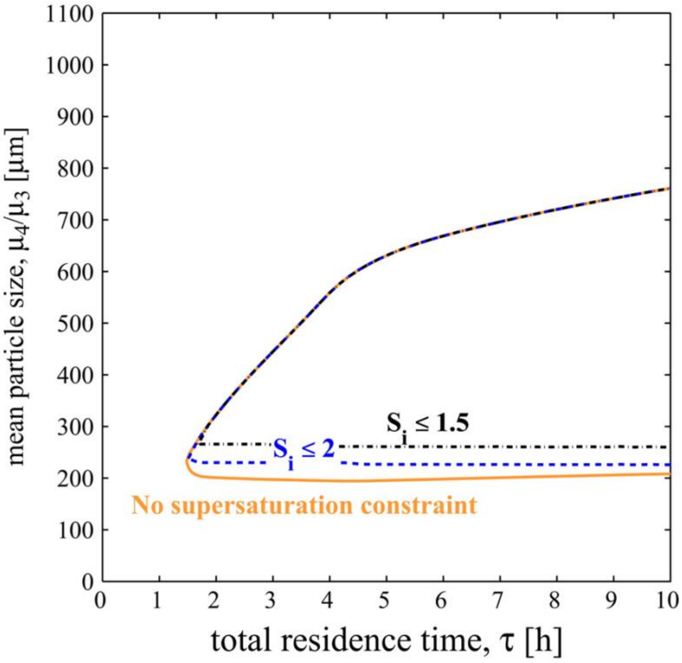

Figure 2.5 Effect of a maximum supersaturation constraint on the attainable crystal sizes during cooling crystallization of paracetamol in a three stage MSMPR cascade. S_i represents the maximum steady state supersaturation ratio for any of the crystallizers in the cascade.[80] [From T. Vetter *et al.*, "*Regions of attainable particle sizes in continuous and batch crystallization processes*", Chemical Engineering Science 106 (2014), 167-180. Used with permission from Elsevier. ©2013 Elsevier]

Note that, when a constraint for realistic supersaturations is applied to the prediction of attainable regions, only the smaller end of the attainable region suffers. These limitations can hardly be compensated by adding crystallization stages. In these situations, alternative methods for the generation of small crystals are required, either by choosing a different crystallization strategy or through mechanical size reduction.

Power *et al.* later expanded on this concept by introducing two more constraints: energy balance and operating volume. The first constraint is related to the setup heat transfer capacity. Indeed, attaining high supersaturations is limited by the capacity of the system to provide the required temperature drop at low residence times. In their experimental setup, the desired crystallization temperature (5 °C) was never achieved because of the high feed temperatures (40 °C) and the low residence time (13 min). The second constraint defines a minimum operating volume for the crystallizers to prevent vortex formation. The effect of both constraints on the attainable crystal sizes is illustrated in Figure 2.6.

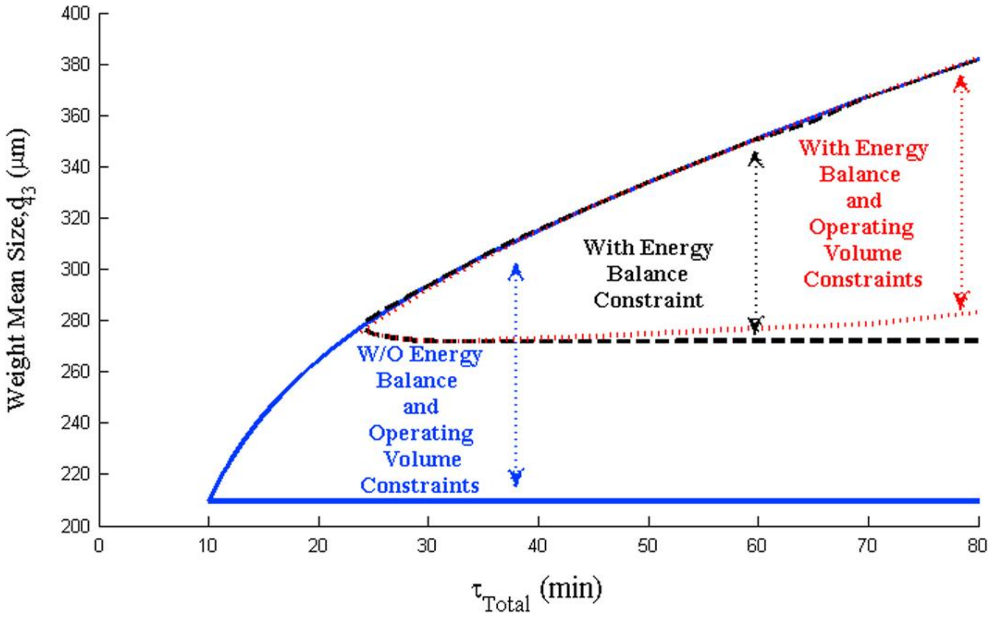

Figure 2.6 Effect of energy balance and operating volume constraints on the attainable crystal sizes during cooling crystallization of paracetamol in a two stage MSMPR cascade.[74] [From G. Power *et al.*, "*Design and optimization of a multistage continuous cooling mixed suspension, mixed product removal crystallizer*", Chemical Engineering Science 133 (2015), 125-139. Used with permission from Elsevier. ©2015 Elsevier]

Overall, when generation of small crystals relies entirely on the use of high supersaturations, process and product constraints will define the lower limit of attainable crystal sizes in an MSMPR cascade. When the required crystal sizes cannot be met in the crystallization process, the manufacturer has to rely on post-crystallization powder processing that can influence the critical attributes of the crystalline API.[28,99,100]

2.5 Recent developments towards process imaging in crystallization

As it was described in Sections 2.4.1 and 2.4.2, crystallization process development is currently simplified to the use of unidimensional models for crystal size distribution and a qualitative assessment of the crystal shape variations. Despite the accuracy of current methods for the prediction of the crystal size distribution based on laser diffraction or FBRM, information on the three-dimensional shape of the crystals is critical for process development. Especially when the shape of the crystals varies during process development and downstream processing, these techniques become unreliable. Hence, several research groups have started implementing imaging techniques in their work.

Although similar instruments are commercially available,[101,102] Mettler Toledo's Particle Vision Measurement (PVM) probe is probably the most common instrument for *in situ* image analysis in crystallization. This instrument has been employed to detect polymorphic transitions,[103–105] to characterize crystal shape during crystallization process development,[70,106–111] to detect the onset of nucleation,[112] and to monitor induced shape transitions during crystallization.[113]

Alternative to the use of probes, images of the crystallization magma can be taken from outside the crystallizer through an observation window or circulating part of the magma in an integrated flow-through cell. In 2005, Calderon De Anda *et al.* presented an on-line image acquisition system using a high-speed camera connected to an observation window.[114] The system was later applied in the batch crystallization of L-glutamic acid, including the determination of the crystal growth rates in different dimensions.[115,116] The same group has recently presented a similar system, employing two high-speed cameras for the reconstruction of the 3D crystal shape from 2D images.[117–119] In parallel to this work, Eggers *et al.* designed an off-line flow-through cell with an external camera for real time process imaging. The method was tested with elongated carbon fiber particles[120] and later applied to the crystallizations of ascorbic acid[121] and paracetamol.[61] Further improvements to this equipment involved the addition of mirrors for the analysis of the 3D crystal shape[122] and their later replacement by a second camera.[123] In contrast with probe-based instruments, external high-speed cameras provide with a non-invasive method for image acquisition that could be advantageous for image acquisition from tubular crystallizers or systems where a probe would be blinded by encrustation. Such instruments have been extensively applied to measure crystallization kinetics and detect the onset of fouling in oscillatory baffled crystallizers.[124–127]

Despite the recent developments on imaging methods, the use of quantitative image analysis in crystallization process development is rarely seen. Images taken on-line present several challenges for the analysis due to variations in background intensity, overlapping crystals, random orientation and a varying distance with respect to the lens.[101,128,129] The use of these instruments is thus limited by the availability of more advanced image acquisition methods and, mainly, because of the lack of appropriate software to determine individual crystal dimensions from images including overlapping crystals and random orientations. In this area, improvement of traditional algorithms for image segmentation and feature detection is receiving a significant interest.[118,119,130,131]

Even though many algorithms are tested with manual image analysis,[123,132,133] the use of manual analysis in process development is very limited because of the large amount of particles required to obtain accurate results. Masuda, Iinoya and Gotoh estimated the amount of measurements required for the accurate determination of the mean mass diameter from a lognormal distribution.[134,135] With a relative error of 5%, and depending on the geometric standard deviation, the required number of measurements varied between 585 and 60,811. The amount of measurements was severely reduced to 37 – 3,801 for a relative error of 20%. Despite these demanding requirements, sampling sizes between 200 and 2,000 crystals have been previously employed to analyze crystal shapes, correlate different analysis methods, and identify trends during crystallization process development.[60,97,113,136–142] Especially when manual analysis is employed for mass-based distributions, the variations during the experiment must be high enough to compensate for the poor accuracy of this approach.

2.6 Novel continuous crystallization configurations to generate small crystals

Because several drugs present poor water solubility, the development of novel crystallizer configurations for generation of small crystals has received considerable attention during the last decade. Several configurations involve the use of tubular crystallizers combined with a seeding step, where seeds are generated using high supersaturations in a high intensity mixer,[106,143–145] by ultrasonication[146–149] and even through the use of directed contact secondary nucleation on a parent crystal.[150,151] However, most configurations based on plug flow crystallizers lack the flexibility of MSMPR crystallizers and present issues with solids classification and fouling.[127,129,152,153]

Recent advances are directed towards production of small crystals using modified MSMPR units. Due to secondary nucleation being the predominant mechanism in these crystallizers, most methods employ mechanical stress for nucleation control. A direct method that has been widely used to reduce crystal size is the integration of wet milling into the crystallization process.[100] Recently, Yang *et al.* investigated the effect of wet mill location on the steady state chord length distribution in MSMPR crystallization, showing that the mill can be used both for downstream size reduction and for upstream seed generation.[154,155] In 2017, Acevedo *et al.* applied population balance models to an MSMPR crystallizer with an integrated wet milling unit, finding that the *in situ* wet mill has a contribution both as a nuclei generator and for crystal breakage.[156] On a similar area, Igarashi *et al.* used a high speed agitator for the generation of small crystals of glycine and L-alanine in a small MSMPR-type crystallizer.[157] Despite the obtained crystal sizes were of the order of 10 µm, it is important to note that they had to employ an agitation speed of 24,000 rpm in a 0.9 mL crystallizer.

Ultrasonication has also been employed as a method to produce small crystals in an MSMPR crystallizer, displaying significant size reductions in crystal size even when compared to micronization or high shear wet milling.[158] During continuous crystallization of adipic acid, the application of power ultrasound reduced the steady state crystal size by almost an order of magnitude.[159] Nevertheless, the actual contribution to nucleation is hard to elucidate as a considerable size reduction was a consequence of the effect of ultrasonication in preventing agglomeration.

2.7 The impact of gas dispersion in batch crystallization kinetics

For many decades, ultrasonication has been used to induce nucleation and generate small crystals during research studies and in industrial production, with available academic studies dating back to the 1920s.[160] Nevertheless, there is still no consensus on the mechanisms by which ultrasonication could impact nucleation.[161] A number of hypotheses have been formulated in this regard, including the effects of collapsing cavitation bubbles on both primary and secondary nucleation, and even crystal fragmentation.[162–165]

One of these theories implies that the cavitation bubbles induced by ultrasonication act as heterogeneous nucleation centers. In 2009, Wohlgemuth *et al.* reported a study where this hypothesis was tested by dispersing the gas phase in a supersaturated solution and measuring the width of the metastable zone during batch crystallization.[166] The study was done for dodecanedioic acid in several solvents, and showed a consistent reduction in the metastable zone width that was independent of the gassing period and the saturation of the gas phase. A year after, they released a similar study comparing the effects of gassing with ultrasound to induce crystal formation during batch crystallization of adipic acid, where both methods showed a similar behavior.[167] Since then, Wohlgemuth and co-workers have applied this technique to induce nucleation and control the crystal size distribution in batch crystallizers.[168–171] In 2014, Ceyhan *et al.* evaluated the effect of the gas composition on the reduction of induction times during batch crystallization, claiming that the type of gas also has an impact on the extent of these reductions.[172] Finally, Matsumoto and co-workers reported an effect of nitrogen minute-bubbles on the nucleation rate and polymorphism of glycine during antisolvent crystallization in water-ethanol.[173]

Overall, the number of studies involving the application of gas to induce nucleation is very limited. However, if gas dispersion had an impact on the nucleation rate during MSMPR crystallization, the method would likely be cheaper, more scalable and more versatile than the application of ultrasound. To this end, it is necessary to investigate (1) if gassing has an impact on secondary nucleation and (2) if this impact can be seen in an MSMPR crystallizer that is already optimized to generate small crystals.

2.8 Conclusions

Because of the strong pressure from generic manufacturers and the increased costs of drug development, the pharmaceutical industry is turning focus towards continuous production in an attempt to reduce costs and improve product quality. In this area, crystallization is an important tool for the definition of crystal quality attributes like crystal size, habit, structure and purity. Continuous MSMPR crystallizers are arguably the most common choice for process development, which would meet the strict requirements for equipment flexibility and rapid process development. However, current development methods based on unidimensional shape-dependent crystal size distributions are very limited for the study of fragile compounds and for systems where the crystal shape depends on the process conditions. Furthermore, process and product requirements limit the maximum attainable supersaturation in MSMPR crystallizers, and thus the achievable crystal sizes. In the field of process development and control, recent advances in process imaging will soon support the simultaneous study of crystal size and shape. However, a proof of concept with modern methods of MSMPR process development is still missing. To generate small crystals in MSMPR crystallizers, novel configurations make use of ultrasonication and milling, which inflict a considerable mechanical stress on the crystals and have a direct impact on crystal shape. Following the reported effect of gas dispersion for promotion of nucleation rates in batch crystallization, this method has potential to become a cheaper and gentle alternative to the generation of small crystals in continuous systems.

3

The Melitracen hydrochloride case study

This chapter is meant to close the gap between the requirements for an academic study and the objectives for process development in Lundbeck. It includes a brief description of the case study, followed by a set of preliminary studies that led to the selection of a crystallization approach, solvent, and a strategy for monitoring the crystal size distribution.

3.1 Abstract

Melitracen hydrochloride is a tricyclic antidepressant currently manufactured by Lundbeck. The main challenges for crystallization of this compound are the elongated, varying crystal habit and the requirements for a small crystal size. In the first part of this chapter, the optimal crystallization solvent has been selected based on a solubility screening and accounting for GMP requirements, availability in Lundbeck and the versatility for use in this study and later process development. Ethanol was found to be the best candidate based on the aforementioned requirements and the considerable experience during batch production. The second part of the chapter involves the selection of an optimization approach for continuous MSMPR crystallization of this compound. The effects of crystal aspect ratio and suspension density on the *in situ* chord length distributions from FBRM were investigated experimentally, revealing that despite the chord length distribution is barely sensitive to the observed variations in aspect ratio, it is heavily dependent on suspension density. Consequently, an optimization approach based on image analysis was selected to obtain simultaneous information on crystal size and shape during the early steps of process development.

3.2 Introduction to the case study

The chosen model compound for this study is Melitracen Hydrochloride. This compound was provided in a purified form from full-scale production in Lundbeck and it was considered appropriate because of its challenging crystal habit and the formulation demands for small crystal sizes. The molecular structure is shown in Figure 3.1.

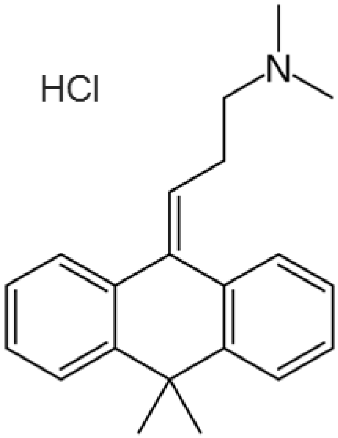

Figure 3.1 Chemical structure of Melitracen hydrochloride.

Melitracen is a tricyclic antidepressant (TCA), well known for being one of the two active ingredients in Deanxit®. While this drug is not marketed in several western countries, it is one of the most frequently used antidepressants in China.[174] Due to its high market share, there is a desire for cost reduction through the transition to a continuous production mode.

3.2.1 Challenges for the crystallization process

Being an API, Melitracen HCl is subject to strict formulation requirements for a certain crystal morphology, purity and size distribution. However, only crystal shape and size distribution are a challenge for the crystallization process investigated in this work. Despite this compound has been manufactured for several years, Melitracen HCl has never displayed polymorphism during full-scale production in Lundbeck. Furthermore, adequate crystal purity is facilitated through the use of an already purified stream as the crystallization feed. Several steps are already included in the synthesis of Melitracen that limit the accumulation of impurities prior to the crystallization process. Even in the currently implemented process, crystallization of Melitracen HCl is employed as a means of obtaining crystals within the required size specifications. These specifications are summarized in Table 3.1.

Table 3.1 Specifications for the crystal size distribution during formulation of Melitracen HCl, provided as percentiles of the cumulative volumetric distribution as measured by HELOS laser diffraction.

Percentile	Crystal size (HELOS Laser diffraction)
X10	2 – 8 µm
X50	7 – 25 µm
X95	20 – 80 µm

The lack of experience with polymorphism and the mild requirements for purification in the crystallization process make this compound an ideal choice for a study focused on crystal shape and size distribution control.

3.2.2 Strategy for continuous process development

In the batch process, Melitracen HCl is isolated by precipitation of a solution of Melitracen in ethanol using HCl gas. A similar strategy was planned at the beginning of the project, where the precipitation of Melitracen with HCl would be studied in a continuous system. However, there were several concerns related to the compatibility with laboratory equipment and the variation introduced during the recovery of Melitracen base from the crystallized Melitracen HCl. As raw material, it was most expedient to isolate Melitracen HCl powder from full-scale production at Lundbeck, and the attempts at recovering Melitracen base in solid form or in solution led to a considerable waste of the expensive API and significant impurity incorporation in the crystallization feed stream. Due to the complications with isolating the free base in a purified form, it was expected that the use of a precipitation approach would not only introduce additional uncertainties to the academic study, but also variations in the impurity profile of the raw material between different phases of the PhD project. The project was thus simplified by using cooling crystallization instead.

In further steps towards the implementation of this process, crystallization will be conducted in a lab-scale flow setup where the synthesis steps are connected to the MSMPR crystallizer. The two streams containing solutions of Melitracen and HCl can either be merged outside or inside the crystallizer. The first approach, despite requiring the use of higher temperatures to maintain Melitracen HCl in solution, will be equivalent to the crystallization process investigated in this project. Assuming that the association between Melitracen and HCl is not a rate limiting factor and that the feed streams are properly integrated in the crystallizer, the second approach should produce similar results without requiring heat traced feed streams and without being limited by the API solubility on the maximum attainable yield.

3.3 Solvent selection

3.3.1 Introduction

One of the legal limitations in pharmaceutical production is that, once a production method has been validated by the relevant authorities, modifications in the manufacturing approach usually require a significant investment in revalidating and in some cases reregistration of the process. For this reason, even though some of the choices made in process development may not be optimal, they are kept throughout production to avoid additional costs. Transition to continuous crystallization gives a chance to reconsider the choices made for the design of the current batch process, one of them being the crystallization solvent.

The crystallization solvent plays a major role in the quality of the crystallized material. Critical crystal properties including habit and polymorphism can be affected by the choice of solvent.[59,175,176] Furthermore, the solvent can have a significant impact on the rates of crystallization, and thus on the obtainable crystal sizes.[177] Unfortunately, selection of the optimal solvent for crystallization is a time consuming process that would require a significant number of crystallization experiments. Solvent selection in this project was simplified to the following considerations:

- Good Manufacturing Practice (GMP) guidelines.
- Solvent availability in Lundbeck (process integration).
- API solubility and attainable step yields.
- Physical properties of the solvent.
- Prior knowledge from full-scale production.

3.3.2 Selecting a list of candidates

Considering that Melitracen HCl is to be sold as an API, there is a heavy restriction for residual solvent contents in the formulation product. The European Medicines Agency (EMA) classified the common solvents in pharmaceutical production in three categories, listed in the ICH guideline Q3C (R6) on impurities and residual solvent contents:[178]

- Class 1: The list includes known or suspected human carcinogens, and environmental hazards. These solvents should be avoided in the production of drugs and excipients unless their use can be justified in a risk-benefit assessment.
- Class 2: Solvents associated with a less severe toxicity, including non-genotoxic animal carcinogens or possible causative agents of other irreversible toxicity, fall

into this list. The use of these solvents should be limited in the later stages of production of drugs and excipients, but they can be present in the formulated product with residual amounts significantly higher than class 1 solvents.

- Class 3: Solvents in this class have a low toxic potential. The list includes no solvent known as a human health hazard at levels normally accepted in pharmaceuticals. Residual amounts of these solvents below 50 mg per day would be acceptable without justification.

The complete list of solvents can be found elsewhere.[178] For crystallization of Melitracen HCl, the first selection was conducted for those solvents that could be recycled to other lines in Lundbeck's production and belong to class 2 or class 3. Then, the list was further reduced to those solvents for which hydrogen chloride solutions are commercially available. The resulting candidates are the class 2 solvent **methanol** and the class 3 solvents **ethanol**, **isopropanol** and **1-butanol**.

3.3.3 Solubility screening

Having reduced the list of possible solvents to four candidates, a solubility screening was conducted to determine the most appropriate solvent for crystallization, accounting for the solubility of both Melitracen HCl and the free base Melitracen.

3.3.3.1 Materials

Melitracen Hydrochloride (≥99.8% purity) was obtained from H. Lundbeck A/S. Methanol (≥99.8% purity), isopropanol (≥99.5% purity) and 1-butanol (≥99% purity) were purchased from Sigma-Aldrich. Absolute ethanol (≥99.8% purity) was purchased from VWR Chemicals. An ammonium hydroxide solution (28.0-30.0% NH_3 basis) was purchased from Sigma-Aldrich and used to recover Melitracen base.

3.3.3.2 Melitracen hydrochloride solubility

The solubility of Melitracen HCl in the four solvent candidates was assessed by gravimetric analysis. The objective was to obtain a rough estimation of the API's solubility curve to assess the maximum attainable yields for a given solvent, crystallization temperature and magma density. The measurements were conducted for different temperatures but without repetitions. The solubility line would be more accurately determined for further process development in the most appropriate solvent.

To measure the API solubility, 4 mL vials containing a suspension of Melitracen HCl on each solvent were placed in a thermomixer (Ditabis Cooling ThermoMixer MKR 13) and left agitated (800 rpm) at constant temperature for at least 20 h. Then, the equilibrium suspensions were filtered through a 0.45 µm syringe filter and the liquid phase was saved for gravimetric analysis. This procedure was repeated at 5 different temperatures (10, 20, 30, 40, 50 °C). Finally, approximately 0.5 g of each liquid solution were dried at 130 °C in an oven. The API solubility was approximated from the dry matter content assuming that the amount of non-volatile impurities and the HCl loss during drying are negligible. The resulting solubility curves are reported in Figure 3.2.

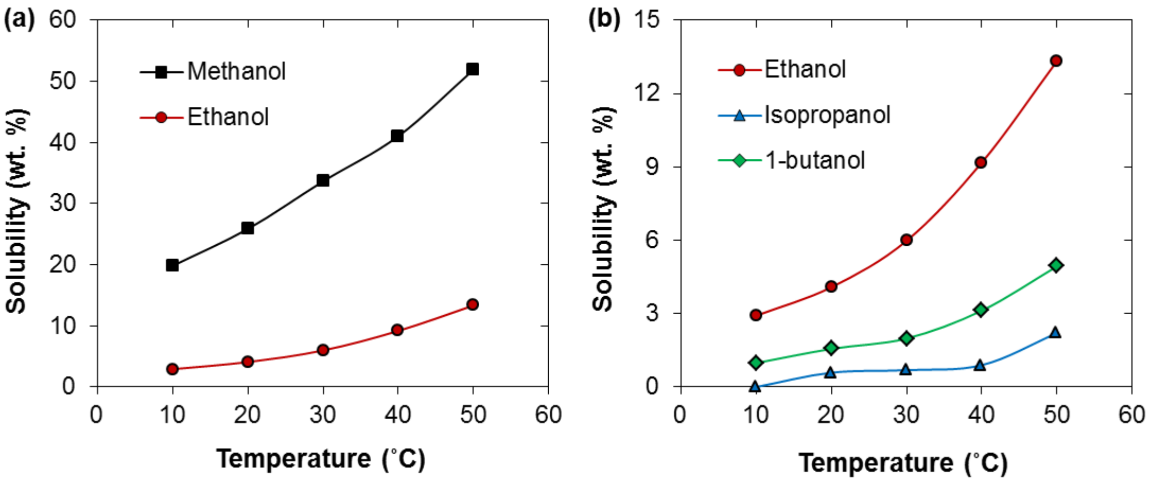

Figure 3.2 Solubility curves for Melitracen HCl in the four solvent candidates, expressed as dry matter content in the saturated solution. (a) API solubility in methanol and ethanol. (b) API solubility in ethanol, isopropanol and 1-butanol.

The four solvents presented significantly different solubilities, with methanol presenting both the highest absolute values and the largest absolute variation with temperature. In relative terms, ethanol presents the largest variation with temperature, with a 357% increase in solubility from 10 to 50 °C. Isopropanol gave the lowest API solubilities of the four solvents, and would be a good candidate for precipitation when high step yields are desired. These results were sufficient to discard methanol as a solvent candidate, as an API concentration higher than 20% in the mother liquor would always lead to low step yields and significant product losses even if solvent recycle is employed.

3.3.3.3 Melitracen base solubility

Despite the work in this thesis will be conducted for cooling crystallization, it is important that the selected solvent is able to dissolve high concentrations of both Melitracen base and HCl so that the isothermal precipitation of this compound can be evaluated in future work. To this end, the solubility of Melitracen base was investigated to demonstrate that the four solvents can solubilize this compound at a reasonable temperature.

Melitracen base was first isolated in solid form by precipitation from a 200 mL saturated aqueous solution of Melitracen HCl. The addition of 2-3 drops of a 28-30% ammonium hydroxide solution was sufficient to trigger the precipitation of Melitracen base as a yellow, amorphous solid that rapidly agglomerated to form a single piece. Vacuum filtration of the precipitated base could not be achieved because the product quickly blocked the filter. Instead, the product was removed from a spatula and washed with demineralized water. Then, it was dried for 24 h in a desiccator. Pictures of the raw material and the obtained product are supplied in Figure 3.3.

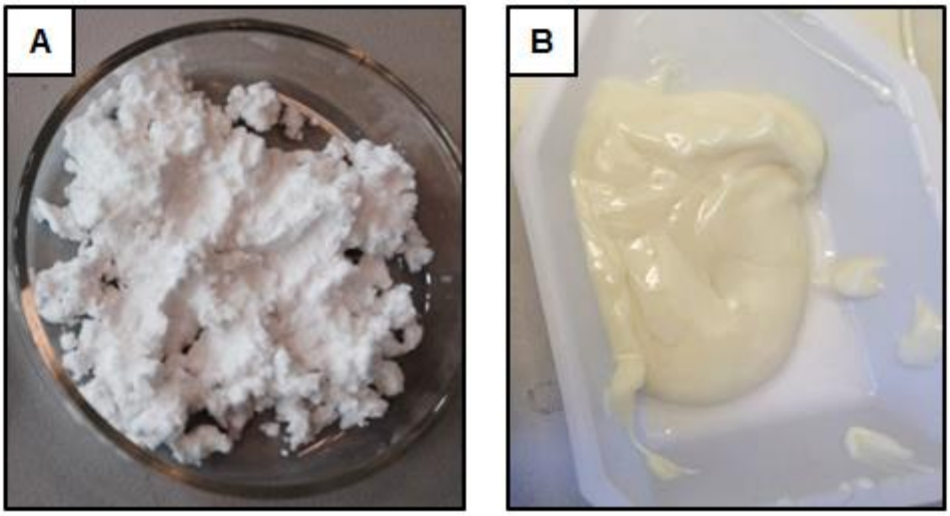

Figure 3.3 (A) Melitracen HCl powder provided as raw material from Lundbeck's production. (B) Melitracen base isolated by precipitation with ammonium hydroxide.

Note that, because of the expected incorporation of water and ammonium chloride into the amorphous solid, only a rough estimation of this compound's solubility can be obtained. It is expected that traces of water will reduce the solubility of Melitracen during the measurement.

Saturated solutions of Melitracen base in ethanol, isopropanol and 1-butanol were prepared at 50 °C using the same method used for Melitracen HCl (Section 3.2.2.2). The solubility in methanol was not investigated due to the previously found high solubilities for the API. To separate Melitracen base from the non-volatile impurities that could be incorporated in the sample, and to verify that the isolated solid was Melitracen base, the analysis was conducted using HPLC instead of gravimetric analysis. The HPLC samples were analyzed using a Hitachi LaChrom Elite system equipped with a Phenomenex Gemini® 10 cm x 4.6 mm x 3 µm C18 110 Å silica column and a L-2455 diode array detector (Hitachi). The concentration of

Melitracen base was determined at 230 nm. Details on the HPLC method are provided in Appendix A.

The obtained API solubilities were 910, 840 and 770 g/L in ethanol, isopropanol and 1-butanol, respectively. These results demonstrate that the solubility of Melitracen base is approximately an order of magnitude higher than the API solubility in the three remaining solvent candidates. Thus, obtaining a clear feed solution containing the precipitating agent is not a concern for the use of precipitation in the implemented process.

3.3.4 Solvent choice

To facilitate the final choice of solvent, the results obtained from the solubility screening have been summarized in Table 3.2 together with other relevant solvent properties.

Table 3.2 Summary of relevant properties for solvent selection. The values come from either the literature or the experimental work described in this section.

	Solvent		
	Ethanol	**Isopropanol**	**1-butanol**
Solvent class (ICH Q3C)[178]	3	3	3
Melitracen HCl solubility (wt. %)	4.1 (20 °C) 13.3 (50 °C)	0.6 (20 °C) 2.2 (50 °C)	1.6 (20 °C) 4.9 (50 °C)
Melitracen solubility (g/L)	910 (50 °C)	840 (50 °C)	770 (50 °C)
Boiling point, 1 bar (°C)[179]	78.2 °C	82.2 °C	117.6 °C
Viscosity (mPa s)[179]	1.07 (25 °C)	2.04 (25 °C)	2.54 (25 °C)
Prior crystallization experience	Full-scale (batch)	None	None

For a given solvent, the maximum attainable step yield in crystallization will be a function of the product suspension density and the API solubility in the mother liquor. Following the mass balance for the crystallization process, the maximum magma density M_T will be a function of the feed concentration C_0 and the API solubility at the filtration temperature T:

$$M_T = C_0 - C_{sat}(T) \tag{3.1}$$

The maximum step yield can be expressed as a direct function of the maximum suspension density and the end stage solubility:

$$Yield = \frac{C_0 - C_{sat}(T)}{C_0} = \frac{M_T}{C_{sat}(T) + M_T} \tag{3.2}$$

In the implemented process, it would be desired to conduct the filtration of the magma at room temperature to avoid the costs and complexity of preventing dissolution/crystallization during filtration. Consequently, the API concentration in the mother liquor has been taken as the solubility at 20 °C.

The limits for the crystallizer's suspension density are both system and scale dependent. Steady state magma densities below 15 wt. % are commonly reported for pharmaceutical MSMPR crystallization in the laboratory scale.[70,74,77,180,181] When the MSMPR crystallizer is connected to a continuous filter, handling high suspension densities becomes even more complicated.[182] These values fall below what would be expected in batch production, and they presumably come from the challenges of handling solids in a small scale flow setup as well as the requirement for longer residence times to minimize high supersaturations and fouling. From the three solvent candidates, only ethanol has the potential to give suspension densities above 10 wt. % in cooling crystallization. Using a precipitation approach instead, and assuming a maximum magma density of 20%, the maximum crystallization step yields at 20 °C would be 83% for ethanol, 97% for isopropanol and 93% for 1-butanol. The three step yields are reasonable considering that the overall yield can be improved by recycling the mother liquor. With a suspension density of 10% and using cooling crystallization in ethanol, the maximum step yield would be 71%.

Even though ethanol is the best solvent candidate for cooling crystallization, it is unclear if isopropanol would be a better solvent to precipitate Melitracen with an HCl solution. Based on yield alone, the low solubility of Melitracen HCl in isopropanol allows for almost total recovery of the solute in crystalline form, even without mother liquor recycle. However, it is important not to disregard that the API is crystallized from an already purified stream. Therefore, most of the mother liquor can be recycled after filtration while limiting the accumulation of impurities in the recycle loop, significantly increasing the overall yield of the downstream process. The solvent's boiling point and viscosity should also be included in the consideration. From a process perspective, a lower boiling point facilitates the solvent recovery by distillation, and lower viscosities are preferred for mixing and fluid transport. In this regard, despite the boiling points of ethanol and isopropanol are very similar, the lower viscosity of ethanol makes it a preferred solvent. Finally, one of the most important aspects in the consideration is the prior experience with the solvent. From batch production, it is known that crystallization of Melitracen HCl with ethanol is capable of giving crystals within the strict size specifications, and this solute-solvent system has not presented issues with polymorphism. Furthermore, there is considerable experience on how to properly separate the crystallization magma. Considering that the step yield can be increased by other means, and that crystallization with ethanol is sufficient for both cooling crystallization and precipitation, it was decided that the small yield advantage of isopropanol was not sufficient to justify the change in crystallization solvent.

In conclusion, ethanol will be used as the solvent in this thesis. This solvent provides with a significant step yield in cooling crystallization and with reasonable solubilities of Melitracen base (910 g/L at 50 °C) and HCl (38.1 wt. % at 32 °C)[183] for the later use of precipitation.

3.4 Limitations of FBRM for process development

3.4.1 Introduction

Focused Beam Reflectance Measurement (FBRM) probes are a powerful tool for the in-line determination of variations in the crystal size distribution. For this reason, they are used extensively to understand crystallization processes. In MSMPR crystallizers, FBRM is commonly used to detect the onset of steady state and, in some cases, for population balance models.[73,77,155,184] Even though the chord length distribution can be extracted *in situ*, there are some concerns as to the limitations for the accurate determination of crystal size distributions from chord length distributions. The chord length distribution given by FBRM is just a fingerprint of the crystal size distribution that depends not only on the size and shape of the crystals, but also on how the sample is presented.[89,185,186]

So far, there is no generally applicable model for the determination of crystal size distributions from chord length distributions., although partial solutions involve the use of empirical correlations or splitting the chord length distribution into different sections that are more representative of specific crystal dimensions.[94,186,187] For example, Leyssens *et al.* exploited the high aspect ratios in needle shaped crystals to detect crystal growth in different dimensions using FBRM.[109] Indeed, when the crystal size distribution is narrow and there is an order of magnitude of difference between the two largest crystal dimensions, one can assume that the counts belonging to the long end of the distribution are mainly influenced by the needle length, while those at the lower end give information on the crystal width.

Crystallization of Melitracen hydrochloride from ethanol solutions typically gives crystals with an elongated, brick-like crystal habit. This shape was consistent throughout the observations in full-scale batch production and for the first experiments with cooling crystallization in the laboratory scale. However, one of the first observations during the project was that, despite sharing the same crystal structure, the crystals obtained in the laboratory had a significantly larger aspect ratio than those provided from full-scale production. Regardless of the source, it was clear that variations in the crystal shape could be encountered during the development of the continuous process, either from different crystallization conditions or from crystal breakage.

Another concern for this compound was related to the applicability of FBRM for the direct comparison of experiments at different suspension densities. In 1999, Barrett and Glennon studied the effect of suspension density on the chord length distributions of spherical Alkaline Frit, and reported a negligible effect of suspension density on the normalized chord length distributions (concentrations below 3.5 wt. %).[91] Three years later, Heath et al. reported an effect of suspension density on the chord length distribution of aluminum particles, even for concentrations below 1 w/v %.[89] However, the same study reported a negligible effect on calcite particles, even at suspension densities at the order of 20 w/v %. Both samples had a low aspect ratio. In a later study with spherical PVC particles, Yu and Erickson reported an effect of solid concentration on the measured chord length distributions. The effect was seen for solid concentrations between 0.1 and 17 w/v %.[186] Seeing the conflicting results in previous studies, it was deemed necessary to quantify the effect of suspension density on the chord length distributions measured for Melitracen HCl crystals.

This section includes an experimental evaluation of the limitations of *in situ* FBRM for crystal size distribution control in the Melitracen HCl case study. The experimental work was aimed to answer (1) if the chord length distribution would be affected by variations in crystal shape and (2) if the obtained chord length distributions at different solid concentrations were directly comparable. The final goal was to assess the difficulty of developing correlations between FBRM and the real crystal dimensions and to investigate if this instrument could be used for MSMPR characterization and modelling.

3.4.2 Experimental section

3.4.2.1 Source of the crystal samples

Melitracen HCl samples with two different aspect ratios were chosen to investigate the FBRM sensitivity to the crystal shape and solids concentration. The formulation product with a small aspect ratio was obtained from full-scale production in H. Lundbeck A/S (HPLC purity ≥99.8%). Crystals with a larger aspect ratio were obtained from a representative MSMPR experiment described in this thesis. The choice was based on the similarity of crystal width with that of the batch product. Details on the experimental setup and methodology are described in Chapter 6, experiment A1.1. The steady state was attained for a crystallization temperature of 10 °C, after which the system was allowed to reach room temperature and thermodynamic equilibrium. The suspension was collected after 24 h. An approximated solids concentration of 7 w/v % was estimated based on the total Melitracen HCl content in the suspension (HPLC, following the methods in Appendix A) and the API solubility at room temperature.

3.4.2.2 Methodology

A saturated solution of Melitracen HCl in ethanol was prepared at room temperature so that it could be used as a dilution medium. First, a 500 mL suspension containing an excess of solids was left agitated in a closed flask for 20 hours. The suspension was first filtered through an *in situ* sintered metal filter (pore size: 10 µm, IDEX Health and Science), and further filtered through a 0.45 µm syringe filter.

Samples from the batch product were prepared in a beaker at room temperature by suspending a known amount of the solid product in the saturated solution. The total suspension volume was kept at 45 mL for all the samples. To avoid crystal breakage during filtration and drying, the samples from MSMPR crystals were prepared by dilution of the 7 w/v % suspension instead of isolating the powder beforehand. The studied concentrations were approximately 1.5, 3, 7 and 10 w/v % for the full-scale batch product, and 1.5, 3 and 7 w/v % for the MSMPR product.

The FBRM measurements were conducted using a G400 probe (Mettler Toledo), measuring the primary distribution from 1 to 1000 µm. The probe was inserted in the magnetically agitated beakers and fixed in a stand. To obtain comparable chord length distributions, all the samples used the same type of magnet and the FBRM probe was kept at constant position throughout the measurements. The minimum agitation intensity for homogeneous mixing was determined at the highest solids concentration by increasing the impeller speed until the chord length distribution remained stable. All the measurements were conducted at the same agitation intensity.

Microscope pictures were taken for each of the samples using a Nikon Eclipse ME600 optical microscope equipped with an HD camera (Leica MC120) and the Leica Application Suite software (ver. 4.5). To investigate if the chord length distribution is related to the crystal dimensions, two representative pictures of each sample were manually analyzed with the help of the image processing software ImageJ (ver. 1.6.0), from which the 2D particle dimensions (width and length) were obtained for each of the crystals in the picture. In total, 644 crystals were analyzed from the batch product (4 samples, 8 pictures) and 408 crystals were analyzed from the MSMPR product (3 samples, 6 pictures). The analysis should provide a rough estimation of the mean crystal width and length for both samples.

3.4.3 Chord length distributions for different aspect ratios

Using a representative chord length distribution and the results from image analysis, the effect of crystal aspect ratio on the chord length distribution was studied in the first place. A sample of the obtained optical microscopy pictures is reported in Figure 3.4.

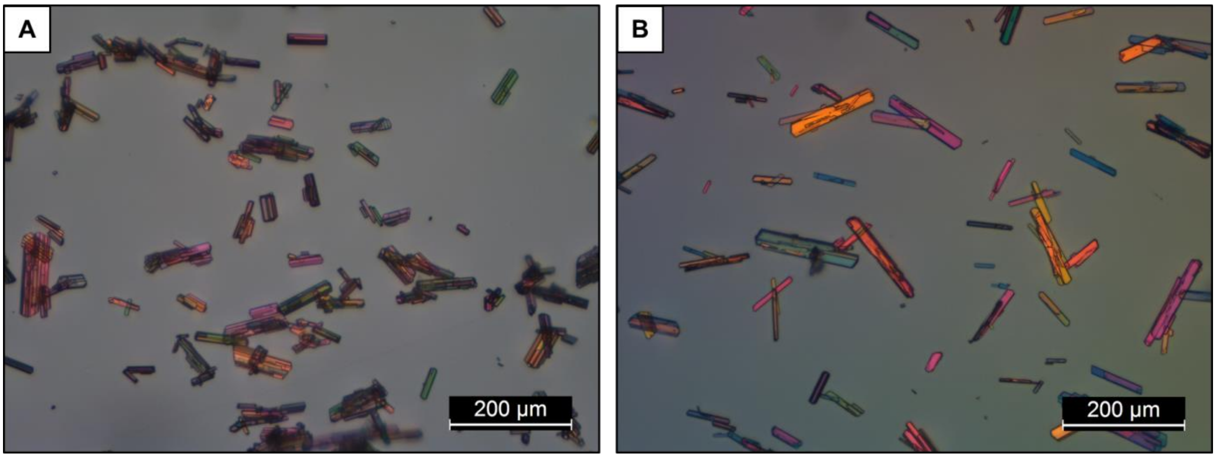

Figure 3.4 Optical microscopy pictures of the suspended product used for the FBRM measurements. (A) Crystals from full-scale batch production in Lundbeck. (B) Crystals from lab-scale MSMPR crystallization.

Note that, despite both samples present a similar crystal width, the crystal length of the product obtained from MSMPR crystallization is significantly larger. This is expressed quantitatively from the results of image analysis. As it can be seen from Figure 3.5, while the crystal width distributions fall around the same region for both samples, the crystal length distribution for the MSMPR crystals is displaced towards larger values. Comparing the typical crystal lengths with the widths, the difference between the two visible dimensions in the 2D crystal projection is approximately an order of magnitude.

Interestingly, while one of the samples presented a substantially larger aspect ratio, the square weighted distribution was not affected by the length of the crystals. These results support that, as it would be expected due to the low probability of the laser beam crossing the crystal length, most of the FBRM counts correspond to corners and smaller crystal dimensions. It is expected that obtaining a distribution representative of crystal length would require the application of an unreasonably high weight to the raw distribution. Thus, based on the results from this section, it is reasonable to assume that small variations in the aspect ratio will not have a significant effect on the chord length distribution for constant crystal width and height.

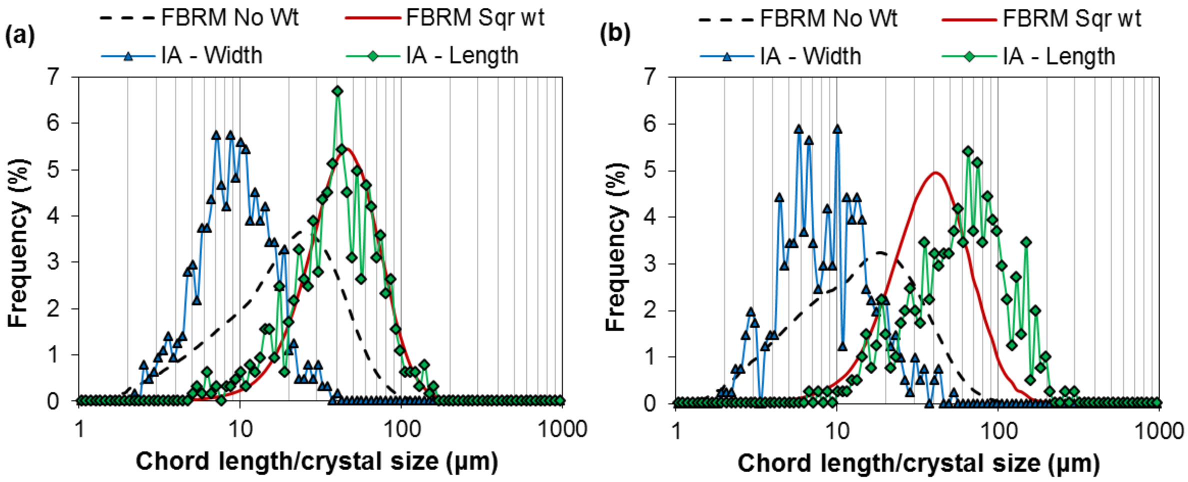

Figure 3.5 Crystal size distributions as measured by FBRM (chord length) and image analysis (IA, crystal size). The chord length distributions were measured for the samples containing 7 w/v. % solids concentration, and averaged over 60 measurements. The reported crystal size distributions from image analysis correspond to the number based distributions for crystal width and crystal length. (a) Crystals from full-scale batch production in Lundbeck. (b) Crystals from lab-scale MSMPR crystallization.

3.4.4 Effect of suspension density on the measured chord length distribution

The normalized chord length distributions for short and long aspect ratios and different suspension densities are reported in Figure 3.6. A common trend for the two aspect ratios is that larger suspension densities lead to a narrow unweighted distribution and, for most samples, a reduction in the square weighted mean size. Similar results were obtained in the previously discussed studies. Both studies by Heath *et al.* and by Yu and Erickson reported a drop in the square weighted mean size with an increase in solids concentration.[89,186] It is expected that, when the unweighted distribution narrows, only the reduction in count frequency at the higher end of the distribution will have a significant impact on the square weighted form. In other words, because the square weighted distribution is mainly defined by the higher end of the unweighted distribution, a lower frequency in both ends of the raw distribution can be seen as a reduction in the square-weighted mean crystal size. The observed narrowing at high suspension densities could be a consequence of several factors. It is expected that high suspension densities will increase the amount of overlapped crystals, thus decreasing the probability that a large chord is measured. Furthermore, as it was also stated by Yu and Erickson, suspension density can affect the laser penetration depth and beam broadening.[186] The latter can also impact the chord length distribution in the opposite way, where high suspension densities would limit the measurement to those particles that are closest to the probe and thus lead to a higher measured chord length.[92]

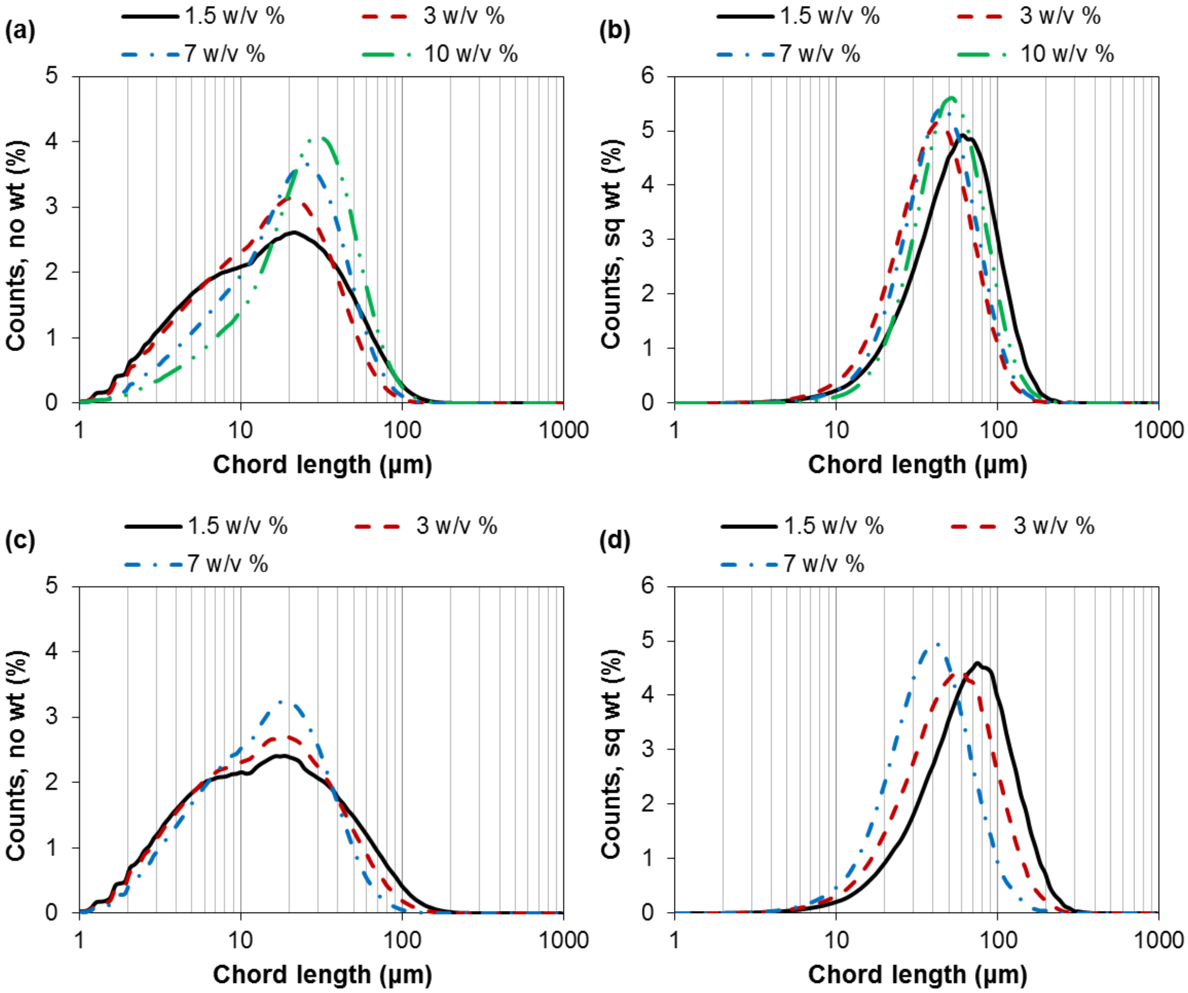

Figure 3.6 Chord length distributions obtained from FBRM analysis of the samples containing different suspension densities. Each distribution is the average of 60 measurements. (a) Unweighted chord length distribution of the batch crystals. (b) Square weighted chord length distribution of the batch crystals. (c) Unweighted chord length distribution of the MSMPR crystals. (d) Square weighted chord length distribution of the MSMPR crystals.

Due to the significant dependence of the chord length distribution with suspension density, it was decided not to employ FBRM for modelling of crystallization kinetics in an MSMPR crystallizer. Especially for the study at different feed concentrations and for multiple stages, the results would be hardly comparable due to the simultaneous variation of crystal shape and suspension density between experiments. Nevertheless, this is still a robust technique for measuring variations in the crystal size distribution *in situ*. In this thesis, FBRM will be used to detect the onset of steady state as well as to detect variations in crystal size distribution during those experiments where the suspension density does not vary significantly.

3.5 Optimization approach involving image analysis

For a new compound with limited kinetic information, defining the optimal number of crystallization stages and the operating conditions is complicated without proper screening of the crystallization process. In MSMPR crystallizers, this screening is normally oriented to obtaining a set of kinetic equations that allow for the modelling of the crystallization process. By using the rate equations in combination with the population and mass balance, one can assess the attainable regions for crystal size, the optimal number of stages to meet a certain objective, and the best operating conditions according to product and process requirements.[66,74,80,188] To this end, even though it is advantageous to obtain crystallization kinetics based on a technique that can be used *in situ*, it is best to optimize the crystallizer based on a method that gives substantial information on crystal quality.

Two size characterization approaches were considered for process development: laser diffraction and imaging techniques. Despite the first is the approved method for quality control, laser diffraction is sensitive to variations in the crystal shape. This is a concern when the obtained product does not share the aspect ratio of the formulation product. Moreover, elongated crystals with aspect ratios at the order of 1:10 are likely to break during downstream processing and tablet formulation. Thus, despite laser diffraction is the preferred method for quality control, the predicted size distributions from MSMPR modelling are not necessarily representative of the formulation product.

To further investigate the source of the different aspect ratio, and to obtain a crystal size distribution that can be used to predict the quality of the formulation product, it was decided to optimize the MSMPR crystallizer based on image analysis. This method, despite being tedious, would provide relevant information on the 3D shape of the crystals. Were the crystals breaking in the downstream process, only the variation in aspect ratio would have to be studied to predict the 3D crystal size distribution of the formulated product.

Note that, due to the lack of a reliable in-line method for quantitative image analysis in crystallization,[185] these methods will only be used for process development. Once the optimal crystallization conditions have been defined, process monitoring and feedback control in the implemented unit can still be conducted using more practical PAT methods.

3.6 Conclusions

This chapter presents an overview of the compound selected for this study, including preliminary knowledge from full-scale production and the requirements and challenges for the transition to continuous crystallization. The first step in process development was to reconsider the solvent choice for this compound. After a preliminary selection based on GMP and production requirements, a solubility screening was conducted for the remaining solvent candidates. Despite isopropanol was the solvent that presented the lowest API solubility and thus the highest attainable step yields, the difference in solubility does not compensate the advantages of ethanol in terms of prior experience and versatility. Considering that the impurity incorporation into the crystallization stream is minimal and that the crystallization yield can be increased from solvent recycle, ethanol was kept as the crystallization solvent in the continuous process.

An evaluation of the effect of crystal shape and suspension density on the measured chord length distributions revealed that *in situ* FBRM was inadequate to approximate crystal size distributions during process development. The different crystal aspect ratios between the full-scale formulation product and the crystals obtained in lab-scale made quantitative image analysis a preferred choice, as the crystal size and shape could be investigated simultaneously.

4 Characterization of a MSMPR cascade by image analysis

This chapter has been written in a manuscript format. A modified version will be submitted to the peer-reviewed journal *Crystal Growth & Design*. The authors to be included in the contribution are *Gerard Capellades, Parth U. Joshi, Kim Dam-Johansen, Michael J. Mealy, Troels V. Christensen* and *Søren Kiil*.

4.1 Abstract

This chapter demonstrates how quantitative image analysis can assist in the characterization of MSMPR crystallizers and the proper selection of mathematical models for the early assessment of crystal quality. An active pharmaceutical ingredient presenting an elongated crystal habit has been crystallized in a two stage continuous MSMPR crystallization platform. As it occurs in full-scale batch production, the API crystals tend to break in the largest dimension during downstream processing. Using image analysis of the crystallization magma, the sources of crystal breakage in the MSMPR cascade have been identified and the impact on crystal habit has been evaluated quantitatively. The kinetic rate equations for nucleation and crystal growth have been determined based on crystal width in a model that simplifies the need for control of crystal breakage. The obtained mathematical model predicts a crystal size distribution that is consistent through a moderate degree of crystal breakage during downstream processing.

4.2 Introduction

In recent years, transition from batch to continuous production has received a significant interest in the pharmaceutical industry. Due to the increasing costs of drug development and the competition from generic manufacturers, extensive research has been conducted for the development of continuous processes for the cost effective manufacturing of pharmaceuticals with consistent quality.[3,12,19]

Crystallization plays an important role in pharmaceutical production, both as a purification method and as a tool to produce crystals of APIs with the right size, habit and crystal structure.[31] MSMPR crystallizers are arguably the most common choice of system for continuous pharmaceutical crystallization. Normally in the form of stirred tanks and analogous to a CSTR reactor, these crystallizers are simple, versatile, and suitable for the in-line assessment of product quality. In contrast with plug flow crystallizers, MSMPR crystallizers are preferred for handling the concentrated suspensions and for the long residence times that are characteristic of crystallization processes.

Previous work demonstrated the applicability of MSMPR crystallizers for continuous production of well-known small molecule pharmaceuticals including cyclosporine,[66,78,189] deferasirox,[76] aliskiren hemifumarate[77] and acetaminophen,[70,74] among others. The development focus depends on the actual demands for the crystallization process, and it becomes particularly challenging for compounds showing polymorphism and complex impurity compositions in the feed stream.[83,184,190] In the field of crystal size distribution control, a common approach is to use semi-empirical rate equations combined with the mass and population balance in the crystallizer to predict the resulting yield and size distribution from a given set of process conditions. Such models offer a significant advantage for the assessment of the attainable crystal sizes and facilitate the selection of an optimal number of stages for the crystallization system.[74,80]

Size characterization techniques are typically based on laser diffraction, sieve fractions or chord length distributions. These techniques, despite being sensitive to the shape of the crystals, offer a size distribution that is based on a single characteristic dimension (equivalent sphere diameter, sieve size, chord length) and thus provide little to no information on the crystal shape. In recent years, a number of methods have been developed for process imaging that have potential for simultaneous in-line control of the crystal size and shape during crystallization.[102,129] Probe-based instruments like Mettler Toledo's Particle Vision and Measurement (PVM) system are frequently used for the qualitative evaluation of crystal shapes during crystallization.[70,103–111,113] Furthermore, the development of alternative non-invasive methods is often reported. These methods involve external high-speed cameras that are either directed to a measurement window in the crystallizer[114,117–119] or to an external sampling loop.[120,122,123]

Image analysis allows for the application of morphological population balances to crystallization. Tracking size distributions in multiple dimensions can provide several advantages for the characterization of crystallization processes, not only for the application of multidimensional crystal size prediction models, but also for the detection of phenomena like agglomeration, crystal breakage, growth rate dispersion or transitions in crystal shape.[62,191] Despite the advantages of image analysis for characterization of crystallization processes and their increasing use in batch crystallization, optimization of an MSMPR crystallizer is rarely conducted for crystal size distributions based on quantitative image analysis, an only few examples can be found in the literature.[60,192,193] In this work, an MSMPR crystallization cascade has been characterized by analyzing the 2D projection of the steady state crystallization magma. Image analysis has been used to evaluate the effect of process conditions on the crystal size and aspect ratio of elongated plate crystals. In addition, the source and extent of crystal breakage in the cascade have been identified, and the attainable particle sizes in the crystallizer have been obtained based on a crystal dimension that is consistent throughout downstream processing.

4.2.1 Motivation and hypothesis

Elongated crystals, typically in the shape of needles or plates, are very common in pharmaceutical production, with products like salicylic acid, acetaminophen or aliskiren hemifumarate often presenting this type of crystal habit.[61,77,137] These crystals are some of the hardest to characterize since most of the size determination techniques assume spherical particles. Furthermore, elongated crystals tend to be fragile in their largest dimension, and it is not uncommon that the shape of the crystallization product differs significantly from that at the formulation step. Figure 4.1 shows a typical approach for in-line size distribution control in a two stage continuous MSMPR process, and a hypothesis on how the crystal shape will evolve during crystallization and downstream processing. This hypothesis is based on the system behavior in full-scale batch production and will be later verified in this work.

The crystal size distribution can be expressed in at least as many ways as the number of dimensions defining the crystal habit. Assuming that the crystals are perfect plates, we can distinguish between crystal length, width and height in order of decreasing size. Systems that exhibit preferential breakage in a single plane have a peculiarity: ideally, only the volumetric size distribution on the perpendicular dimension will be affected by breakage, as the total mass related to each of the other crystal dimensions is retained during crystal fracture. This hypothesis assumes that crystal breakage occurs in a plane that is completely perpendicular to the largest dimension, and neglects the formation of fines during the fracture. Thus, it works best for systems with high aspect ratios and a limited degree of crystal breakage.

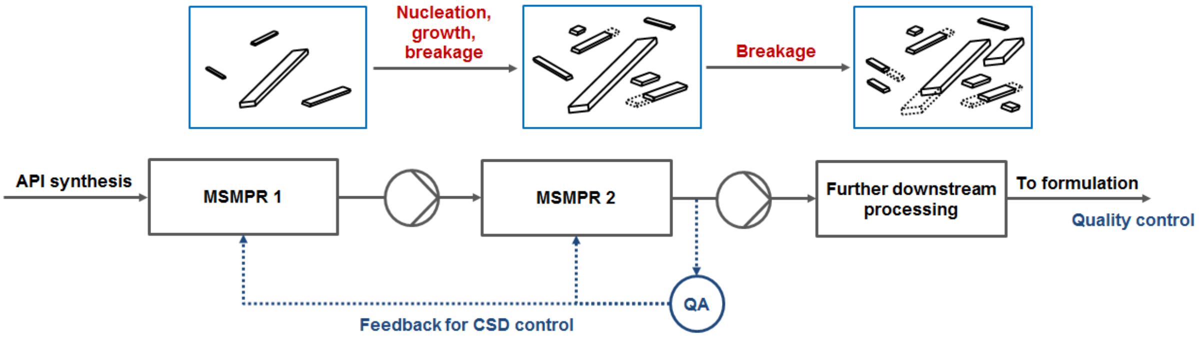

Figure 4.1 Hypothetical crystal breakage during suspension transfer and downstream processing of elongated plate crystals. Quality Assurance (QA) is expected to occur at the end of the crystallization process, providing feedback for CSD control in the MSMPR cascade.

For systems following this behavior, the mathematical modelling of the MSMPR crystallizer can be simplified by use of a crystal shape that is only dependent on the crystallization rate, which can be obtained from image analysis of those experiments with negligible crystal breakage. This distribution permits the determination of a population function that is independent of crystal breakage, thus allowing the independent evaluation of mechanisms like size-dependent growth or growth rate dispersion. Then, a crystal size prediction model can be developed for those dimensions that are consistent through downstream processing. The formulation 3D crystal size distribution can be approximated from the predicted dimension and the distribution of aspect ratios obtained after downstream processing, thus simplifying the extensive breakage modelling in downstream processing.

4.3 Materials and methods

4.3.1 Materials

Melitracen hydrochloride (≥99.8% purity) was obtained in powder form from full-scale batch production in H. Lundbeck A/S. Absolute ethanol (≥99.8% purity) was purchased from VWR Chemicals and used as a solvent for the process. Acetone (≥99.5% purity) purchased from VWR Chemicals was used to wash the crystals after filtration.

4.3.2 Experimental setup

A schematic diagram of the continuous crystallization setup is depicted in Figure 4.2. The setup consists of three vessels connected with programmable peristaltic pumps (P1: LongerPump BT100-1F; P2/P3: LongerPump WT600-1F), and it can operate both for single stage and two stage continuous crystallization. P1 continuously delivers the feed solution to the first MSMPR crystallizer at a flow rate between 1.8 and 7.3 mL/min, depending on the residence time. To prevent crystallization in the feed tubing, the stream was heat traced to 60 °C using heat tape and a temperature control unit (Lund & Sørensen).

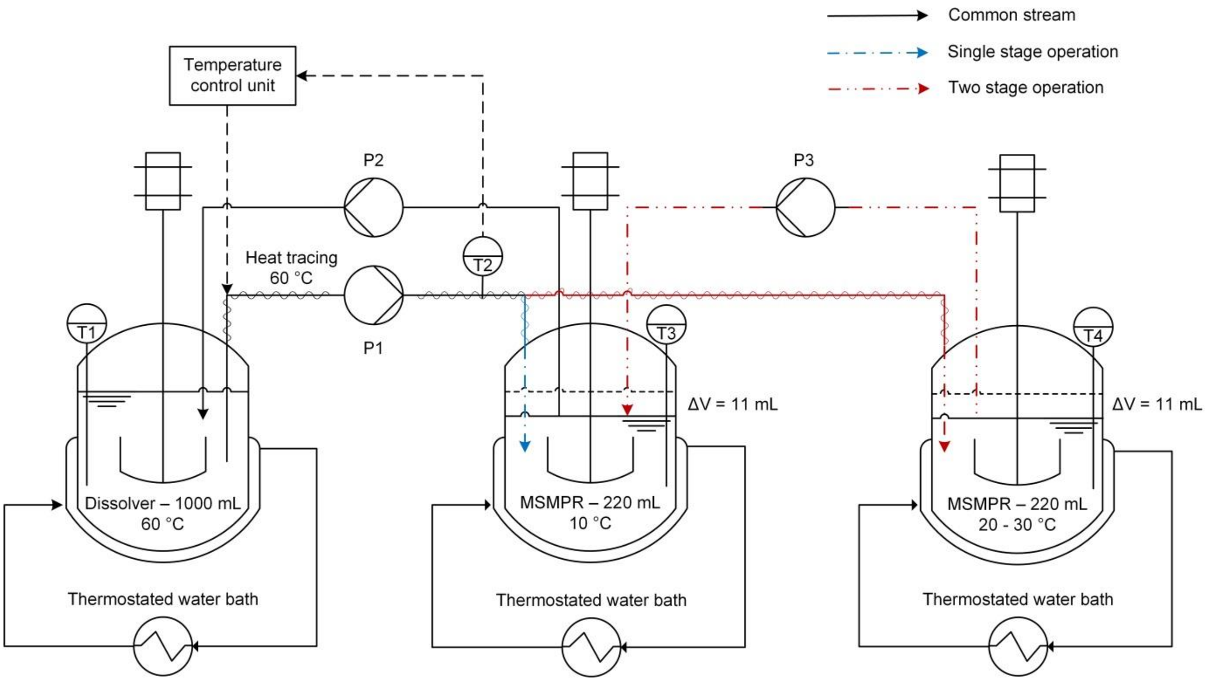

Figure 4.2 Schematic diagram of the two stage MSMPR crystallization setup.

Two jacketed round-bottom reactors with mechanical stirring and an operating volume of 220 mL were used as MSMPR crystallizers. The crystallization magma was mechanically agitated using a three-blade ringed propeller (45 mm, stainless steel, Heidolph Instruments) working at 400 rpm. Due to the nature of the crystallization system, the impellers were coated with a thermoplastic fluoropolymer (Accofal 2G54, Accoat) to prevent fouling and corrosion during extended operation times. Both crystallizers were constructed with the same components, and they operated at the same volume and agitation speed.

Following a common approach for the operation of lab-scale MSMPR crystallizers, suspension transfer was conducted in semi-continuous mode to achieve isokinetic withdrawal of the crystallization magma.[70,78,181] P2 and P3 were programmed to operate intermittently, removing 5% of the suspension volume every 5% of a residence time. First, the pump removes part of the crystallization volume until the liquid level reaches the end of the dip pipe. Then, it pumps air for another 5 seconds to rinse the stream from any remaining suspension. This intermittent withdrawal system was used to minimize classification in the removed magma by applying a high intermittent flow instead of a constant, lower flow rate. For a maximum suspension density of 100 g/L and an FBRM square weighted mean chord length between 40 and 60 μm, a flow rate of 1850 mL/min and a tubing internal diameter of 6.4 mm were sufficient to prevent both classification and plugging during suspension transfer.

To be able to operate for extended periods of time and to minimize the amount of feed solution required for an experiment, the crystallization magma was returned to the feed vessel so that the product could be re-dissolved and reused as feed.[74] For a feed temperature of 60 °C, it required only a few seconds for the magma to completely dissolve. The heat tracing in the feed pipe ensures that any remaining fines were dissolved before reaching the first crystallizer.

4.3.3 Determination of the solubility curve

To obtain accurate solubility data that can be used for the mathematical model, the solubility curve was determined again using triplicate samples and the HPLC method in Appendix A, instead of using the approximated gravimetric determination from Chapter 3. A 220 mL suspension containing 125 g/L of API was prepared in the MSMPR crystallizer at room temperature. After crash cooling to 5 °C, the suspension was maintained under agitation for 2.5 h. Then, triplicate 4 mL samples of the suspension were filtered through a 0.45 μm sterile syringe filter and the liquid phase was kept for HPLC analysis. To verify that the system was at equilibrium, samples were removed in 10 min intervals and the concentrations were compared. Further solubility points were obtained applying heating intervals of 5 °C to the same suspension. After each objective temperature was reached, the suspension was kept agitated for 90 min prior to the removal of triplicate samples. A total of 7 solubility points were obtained within the range of 5 to 35 °C.

4.3.4 Operation of the MSMPR cascade

The continuous crystallization experiments were conducted in the setup described in Figure 4.2. To start an experiment, the feed vessel and the crystallizers were filled with a saturated suspension containing the target concentration of API. Then, the temperatures of each vessel were adjusted to the experimental conditions. The pumps were started as soon as the temperatures stabilized. P1 was set to pump at full speed for the first 10 s of operation to equilibrate the temperature throughout the feed stream and prevent clogging during start-up. Then, the calibration of the flow rate was validated using a 5 mL graduated cylinder.

The evolution to steady state was tracked in-line using an FBRM ParticleTrack G400 probe from Mettler Toledo. To obtain relevant chord length distribution data, the probe window was cleaned every residence time to remove encrustation. The onset of steady state was determined from FBRM data and later verified by HPLC determination of the system concentrations.

The steady state was sustained for at least four consecutive residence times before the experiment was stopped. At each residence time, 4 mL samples were removed from the feed solution and the crystallization mother liquor. The mother liquor samples were obtained by filtration of a magma sample through a 0.45 µm syringe filter.

At the end of the experiment, the feed flow rate was measured again and compared with the value at the start of the experiment. Encrustation in the feed pipes could lead to a decay on the flow rate. Thus, this verification ensures that the residence time was not altered during the experiment. The acceptance criterion was a deviation equal to or lower than 0.1 mL/min. After measuring the feed flow rate, three samples of the crystallization magma were collected at three different positions in the crystallizer (top, middle, and bottom). The steady state classification in the MSMPR unit was determined from the difference between the API concentration in the collected samples and that in the feed vessel. Finally, the crystallization magma was filtered using a vacuum system and the crystals were washed with cold acetone. Although no issues with polymorphism have been previously experienced for this compound in batch production, samples from four relevant experiments were analyzed using X-ray powder diffraction (XRPD) to verify that the crystal structure remained consistent throughout this work. The results are reported in Appendix B.

4.3.5 Off-line analytical techniques

The solubility, feed, mother liquor and magma samples were analyzed using HPLC. The HPLC system (Hitachi LaChrom Elite) was equipped with a Phenomenex Gemini® 10 cm x 4.6 mm x 3 µm C18 110 Å silica column and a L-2455 diode array detector (Hitachi). The API concentration was determined at 230 nm (see Appendix A for methods). XRPD patterns of the filtered crystals were obtained for 2θ between 5° and 40° using a Bruker D8 Advance diffractometer. Finally, SEM analysis was conducted to determine the 3D shape of the crystals employing a FEI Quanta 200 electron microscope. The SEM samples were pre-coated with a 5-10 nm gold layer.

4.3.6 Image analysis

A simple off-line sampling method for the accurate imaging of the crystallization magma has been developed in this work. It was decided to aim for a labor intensive yet reliable method to determine the crystal size distributions. A major limitation for in-situ image analysis is the ability to provide quantitative results at high solid concentrations. In addition, determination of the 2D or 3D crystal shape from pictures obtained with an in-line camera is complicated. The observed crystal size is a function of the crystal orientation as well as their distance to the focal point. Since variations in the steady state crystal size distribution from MSMPR crystallization can sometimes be very small, an off-line method where the crystals fall flat in the same plane was employed.

The method consists of diluting a sample of the crystallization magma with a saturated solution of the solute and then measuring the crystal dimensions in a closed system. To prepare the saturated solution, Melitracen HCl powder was suspended in ethanol a day beforehand and left agitated at room temperature during the experiment. Before sampling, the suspension was filtered using two 0.45 μm syringe filters in series, collecting the liquid phase in an open petri dish (approximated capacity: 20 mL). The petri dish was completely filled to minimize the amount of air trapped in the sample. Then, a few drops of the crystallization magma were added to the clear saturated solution and the petri dish was sealed. A picture of the sampling system is shown in Figure 4.3.

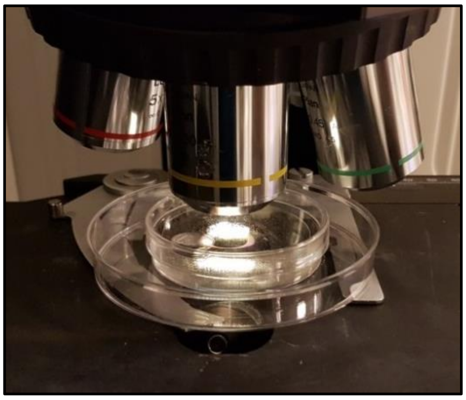

Figure 4.3 Sample cell for the microscope analysis, containing a sample of the crystallization magma diluted in a saturated solution of the API. The larger petri dish is placed to contain accidental spills.

This sampling approach has multiple advantages. First, the saturated API solution dilutes the sample, thereby bringing the supersaturation in the magma down to a negligible value. This limits crystal growth during off-line analysis. In addition, diluting the sample in the saturated solution greatly reduces the suspension density, allowing for an easier identification of each crystal in the picture and reducing the amount of overlapping crystals. Using a closed petri dish minimizes solvent evaporation, which would otherwise promote crystal growth. Lastly, analyzing a suspended sample facilitates the even distribution of the fragile crystals by gentle shaking.

The samples were analyzed using a Nikon Eclipse ME600 optical microscope equipped with an HD camera (Leica MC120) and the Leica Application Suite software (ver. 4.5). To verify the stability of the crystal size distribution during the off-line sampling, pictures were taken at the same position immediately after sample preparation and 5 minutes later to detect dissolution and crystal growth. Figure 4.4 shows an example of two pictures taken for this verification method. After the sample stability was verified, the petri dish was screened to obtain representative pictures of the crystallization magma.

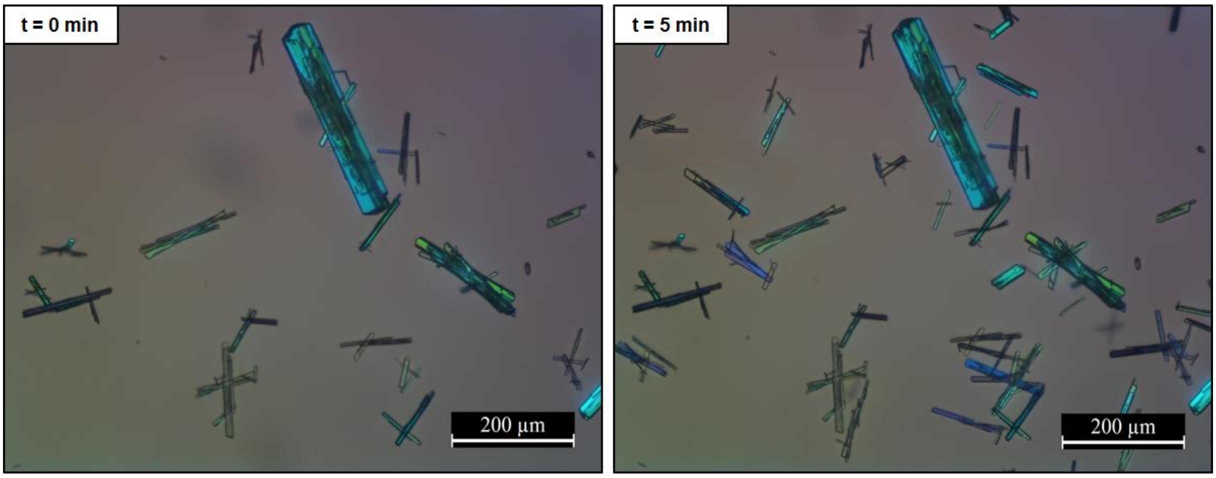

Figure 4.4 Off-line optical microscopy pictures of the crystallizer magma, taken at the same position in the petri dish. The pictures are taken 5 minutes apart to study the stability of the off-line samples. The second picture contains more crystals as the suspension takes 2-3 minutes to settle completely.

Note that this off-line sampling method is not as practical as the state of the art in-line process imaging, from which magma pictures can be obtained in real time using a non-invasive instrument. The main disadvantage of the method described here is that it is limited to process design, and off-line sampling is not a practical approach for crystal shape control in the full-scale process. However, with the recent advancements in the development of algorithms for the accurate determination of crystal size and shape from on-line process imaging, this process will likely be automated soon.[118–120,130]

Image analysis was conducted manually using the image processing software ImageJ (ver. 1.6.0). The measurements originated from several pictures obtained at four different residence times in the steady state crystallizer. An approximated sample number of 700 crystals was chosen based on the relative variations in the mean crystal dimensions over sample number compared to the crystal size variations between crystallization experiments. The relative variations in the mean size with the sampling number are provided in Appendix B, and consequences of the measurement uncertainty will be discussed later in Section 4.5. During the measurement, all the complete crystals in a given picture must be analyzed before the next picture is studied. This is done by dividing the image into 12 segments of equal size and analyzing all the crystals in each region. This approach minimizes the operator error during sample analysis, as it becomes more difficult to overlook the smaller crystals.

4.4 Experimental results

4.4.1 Solubility curve

The obtained solubility curve for Melitracen HCl in ethanol is reported in Figure 4.5. The solubility of the system has an exponential temperature dependency for temperatures between 5 and 35 °C. The fitted exponential expression will be used to determine supersaturations in both the experimental data and the mathematical model.

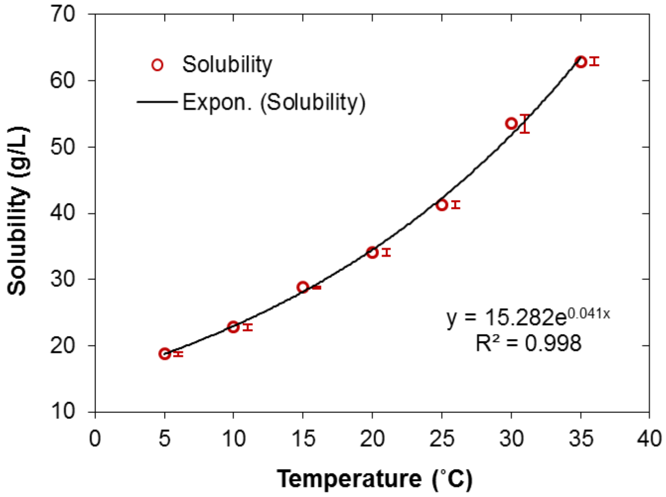

Figure 4.5 Solubility curve for Melitracen hydrochloride in ethanol. The error bars show the standard deviation between the triplicate HPLC samples. These are placed at the side of each point for clarity.

4.4.2 Evolution to steady state and reproducibility

As a first step to assess the reliability of the MSMPR data, three MSMPR experiments were conducted in single stage aiming for the same process conditions. A summary of the steady state conditions for each repetition is provided in Table 4.1.

Following a similar approach to the one presented by Hou *et al.*,[70] the system reproducibility was assessed for different starting suspensions. R1 started from an equilibrium suspension using crystals from the full-scale batch process. R2 started from the steady state suspension from R1, which was left to reach equilibrium before the experiment. At the end of R2, 30 mL of the feed solution were pumped into the steady state magma and the crystals were allowed to grow overnight. The agitation intensity was kept at 150 rpm to minimize crystal breakage. The resulting suspension was used as the starting point in R3. As it will be discussed from the SEM and microscopy analysis, the full-scale batch and MSMPR crystals present significantly different crystal habits. Thus, the reproducibility has been studied for starting suspensions including different shapes and starting crystal sizes.

Table 4.1 Steady state conditions for the three repetitions in single stage MSMPR crystallization. The concentration values include the mean ± standard deviation of the four replicates at steady state.

Experiment	C_0 (g/L)	T (°C)	τ (min)	C_{ml} (g/L)	σ^a	Yield (%)^b
R1	122.0 ± 3.4	10	60	33.7 ± 2.0	0.46	72.4
R2	127.2 ± 3.0	10	60	34.2 ± 0.6	0.49	73.1
R3	128.4 ± 0.6	10	60	33.6 ± 0.1	0.46	73.8

[a] The supersaturation σ is calculated as $(C_{ml}-C_{sat}(T))/C_{sat}(T)$, for which a value of 0 corresponds to the thermodynamic equilibrium.

[b] The step yield is calculated as $100(C_0-C_{ml})/C_0$.

As it can be seen from Table 4.1, the three repetitions gave similar mother liquor concentrations and yields. The standard deviation of each concentration value is a function of the concentration fluctuations at steady state. These are at a similar order than the variations in the steady state mother liquor concentration for different repetitions. Furthermore, the feed concentrations tend to give a higher deviation than the crystallizer mother liquor, presumably because of the higher dilution factor that these samples require for HPLC analysis.

The steady state consistency is further verified with the FBRM data from the three repetitions and reported in Figure 4.6.

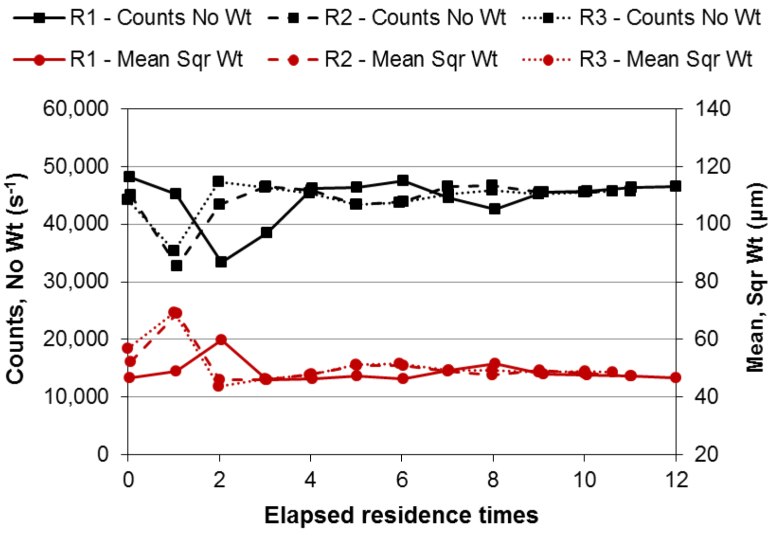

Figure 4.6 Evolution of the FBRM counts and square weighted mean chord length throughout the three repetitions.

As it has been seen for other systems, the experiment starts with a washout phase lasting for 1-2 residence times, when the initial suspension is removed at a faster rate than new crystals are generated.[74] This is seen as a drop in the total number of counts and, for this system, as an increase of the mean chord length due to the growth of the seed crystals. The washout phase leads to an increase in the system supersaturation that eventually triggers system response. Then, the total number of counts increases and the mean size is reduced due to the increased nucleation rate. The system reaches a pseudo steady state after 4 residence times. However, the chord length distribution does not stabilize until residence time 8-9. This behavior was consistent throughout all the experiments in this work. Considering the small extent of the fluctuations, it could be caused by a high dependency of the nucleation rate on supersaturation. Such dependency would lead to a high nucleation at the end of the washout phase, dropping the supersaturation below the steady state value and leading to a second washout. As it will be reported in Section 4.5, this system has a nucleation rate order for supersaturation of 2.60, which is on the high end for cooling MSMPR crystallization.[194] However, these values are far below what would be expected for high-order cycling, which explains why the system eventually stabilizes.[30,56] To ensure consistent concentration and size distribution data, HPLC and microscope sampling were conducted after residence time 9.

4.4.3 Continuous crystallization experiments

A set of continuous crystallization experiments were conducted to serve as a basis for the characterization of the MSMPR cascade. For the experimental design, a constant temperature of 10 °C was selected at the final crystallization step. The objective in the implemented process will be to obtain a crystallization magma that is saturated at room temperature to limit variations in the crystal size distribution and fouling in the transfer pipes connecting to the filtration process. Lower temperatures were not explored in this work because of this constraint. The experimental conditions and steady state concentrations are summarized in Table 4.2.

The effects of feed concentration and residence time on crystallization kinetics were investigated first in single stage (E1-5). Then, the experiments were extended to investigate the effects of performing part of the separation at a higher temperature (E6-9, stage 1). Note that, in contrast with varying solely the feed concentration, variations in temperature lead to significant changes in both the temperature dependent rate constants and the crystallizer's suspension density. This combined effect does not allow to isolate the effect of suspension density unless the feed concentration is varied in separate experiments.

Table 4.2 Steady state results for the continuous crystallization experiments. Those experiments containing two columns were conducted in two stage crystallization, showing data for stage 1 (S1) and stage 2 (S2). The concentration values include the mean ± standard deviation of the four replicates at steady state.

Exp.	C_0 (g/L)	MSMPR stage	T (°C)	τ (min)	C_{ml} (g/L)	σ	Yield (%)
E1	130.2 ± 1.2	S1	10	60	34.3 ± 0.1	0.49	73.6
E2	127.9 ± 0.9	S1	10	90	33.0 ± 0.3	0.43	74.2
E3	125.8 ± 1.3	S1	10	120	30.3 ± 0.2	0.32	75.9
E4	90.4 ± 0.9	S1	10	60	32.1 ± 0.4	0.40	64.4
E5	60.2 ± 1.5	S1	10	60	31.8 ± 0.1	0.38	47.1
E6	127.5 ± 0.4	S1	20	30	44.8 ± 0.7	0.29	64.9
		S2	10	30	28.6 ± 0.3	0.24	77.6
E7	127.0 ± 1.0	S1	20	60	43.3 ± 0.3	0.25	65.9
		S2	10	60	27.7 ± 0.6	0.20	78.1
E8	127.7 ± 2.2	S1	30	30	66.6 ± 0.9	0.27	47.8
		S2	10	30	32.7 ± 0.7	0.42	74.4
E9	125.9 ± 1.2	S1	30	60	62.6 ± 1.0	0.20	50.3
		S2	10	60	30.2 ± 0.7	0.31	76.0

The multistage crystallization experiments (E6 to E9) were designed to have the same total residence time as experiments E1 and E3. This allows for a direct comparison of the effect of number of stages and first stage temperature on crystallization yield. As it was recently reported by Li *et al.*,[66] increasing the number of stages is a practical method to attain higher yields for a constant residence time and final stage temperature. Working with multiple stages allows part of the crystallization process to be conducted at a higher temperature, which typically results in faster crystallization rates. The temperature of the first stage plays an important role in the extent of this promotion.[189]

Note that, for the same feed concentration and total residence time, the highest product recoveries were obtained when the first stage operates at 20 °C (E6 and E7), while a first stage temperature of 30 °C (E8 and E9) does not offer a significant advantage against single stage crystallization (E1 and E3) from a yield perspective. This behavior shows that higher temperatures in the first stage do not necessarily lead to a higher productivity. Although kinetics are expected to be faster at 30 °C, increasing the crystallization temperature reduces the attainable step yield in the first stage. This means that most of the solute recovery is left for the second stage that is subject to slower kinetics. Furthermore, the faster kinetics in the first stage lead to lower steady state supersaturations. For the same residence time, the crystallizers operating at 30 °C have the lowest supersaturation observed in the first crystallization stage. From a yield perspective, operating this close to equilibrium is not efficient in an intermediate stage as it lowers the overall productivity of the crystallization process.

The fraction between the API concentration in the crystallization magma and that at the feed vessel was used to investigate the steady state classification. The values for each experiment are presented in Figure 4.7. From all the experiments in this work, only one of the MSMPR crystallizers presented a higher API concentration in the MSMPR than in the feed vessel. Considering that the observed deviations never exceeded 5%, and that the classification levels seem to be independent of the residence time and suspension density, it is reasonable to assume that the deviations come from the experimental error in sampling suspensions and that MSMPR crystallizer is operating close to ideal mixing.

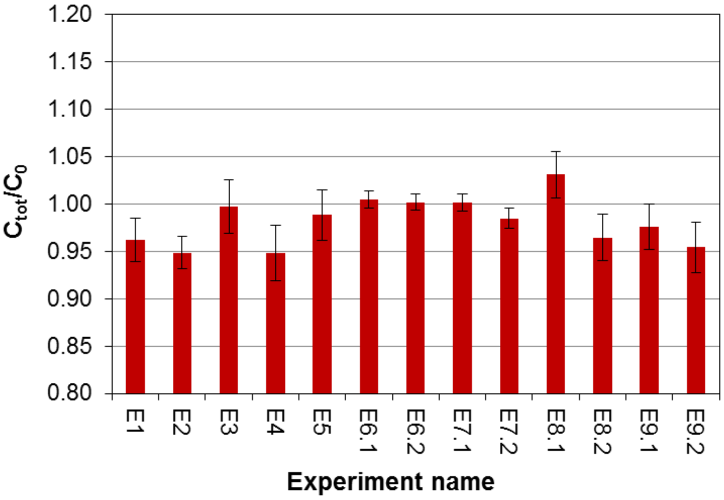

Figure 4.7 Steady state classification values for each continuous crystallization experiment, expressed as the fraction between the API concentration in the magma and that in the feed. Experiments named as EX.Y correspond to the run EX on stage Y. The error bars correspond to the standard deviation from HPLC analysis accounting for error propagation.

4.4.4 Crystal habit of the full-scale batch and MSMPR crystals

Figure 4.8 shows SEM pictures of the crystals obtained from lab-scale MSMPR crystallization (E8) and the crystals used in formulation in the full-scale batch process.

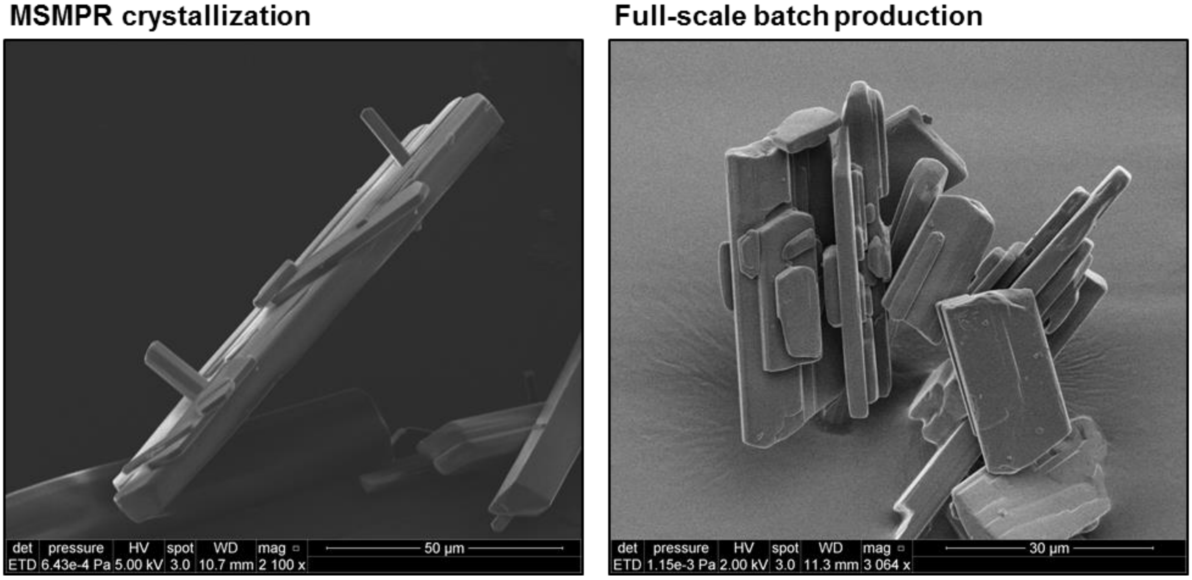

Figure 4.8 SEM pictures displaying the 3D shape of the API samples collected from the MSMPR process, compared to those supplied from full-scale batch production. Note that the two pictures have a different scale bar.

Crystal habit is a main function of the internal structure of the crystals and the crystallization conditions. These conditions include the choice of solvent, the presence of impurities and the rate of crystal growth.[30] Furthermore, mechanical stress causing crystal breakage and attrition can have a significant impact on the final shape of the crystals.

Both processes produce crystals with a plate morphology and a similar relation between the crystal height and width. However, the full-scale batch product exhibits a significantly shorter crystal length. In contrast with the product from MSMPR crystallization, the batch product was likely subject to substantial mechanical stress in downstream processing. The different crystal habit could be explained as a consequence of crystal breakage occurring during downstream processing in full-scale production. However, this hypothesis cannot be verified without a proper study of the effect of crystallization kinetics on crystal habit. Even though both processes use the same solvent and start from a purified solution, the nature of the batch process and the supersaturation profile are completely different. The source of the different morphology will later be investigated from the effect of process conditions on crystal habit and from the behavior of the system upon crystal breakage.

4.4.5 Effect of process conditions on crystal habit

Crystals present multiple crystallographic planes. In this work, we have simplified the crystal morphology to three characteristic dimensions: width, length and height, the latter being the shortest dimension that is hidden in the 2D projection. For the shape analysis, it is assumed that the crystals fall flat in the sample, displaying their two largest dimensions. This is promoted by using a sample presentation method that dilutes the crystallization magma and by the significant difference in surface area between planes in elongated crystals.

Figure 4.9 shows the steady state crystal shape distribution of the first stage MSMPR magma during four runs at variable supersaturations and temperatures. The objective behind the analysis is to detect variations in crystal shape caused by the different conditions of crystal growth. As it was verified during the later analysis of the population balance, experiment E3 and E8 had, respectively, the smallest and largest crystal growth rate in the first MSMPR stage. Populations in the second crystallization stage were left out of this analysis, as they are susceptible to crystal breakage during suspension transfer. Results in Figure 4.9 demonstrate that, in this range of operating conditions, the rates of crystal growth for crystal width and crystal length are proportional regardless of the process temperature and supersaturation.

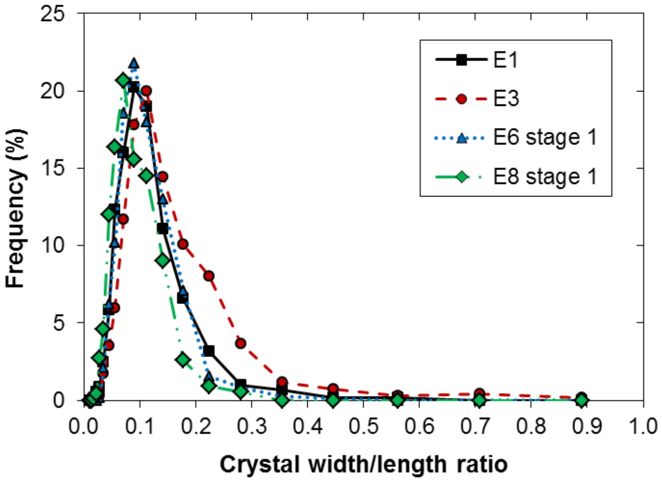

Figure 4.9 Crystal shape distribution, expressed as the ratio between crystal width and crystal length, for the 2D projection of the steady state magma in different runs. The experimental conditions cover the range of supersaturations from 0.27 to 0.49 and temperatures from 10 °C to 30 °C.

Note that the crystal shape distribution for run E3 appears wider than the rest. Different mechanisms, including breakage, size-dependent growth and growth rate dispersion in one dimension, could cause a broadening of the crystal shape distribution. These mechanisms can be investigated from the size dependence of the crystal shape and from the population balance in the MSMPR crystallizer. However, the first step is determining if the broadening is consistent throughout the different crystal sizes. This can be studied from a shape vs length diagram as shown in Figure 4.10.

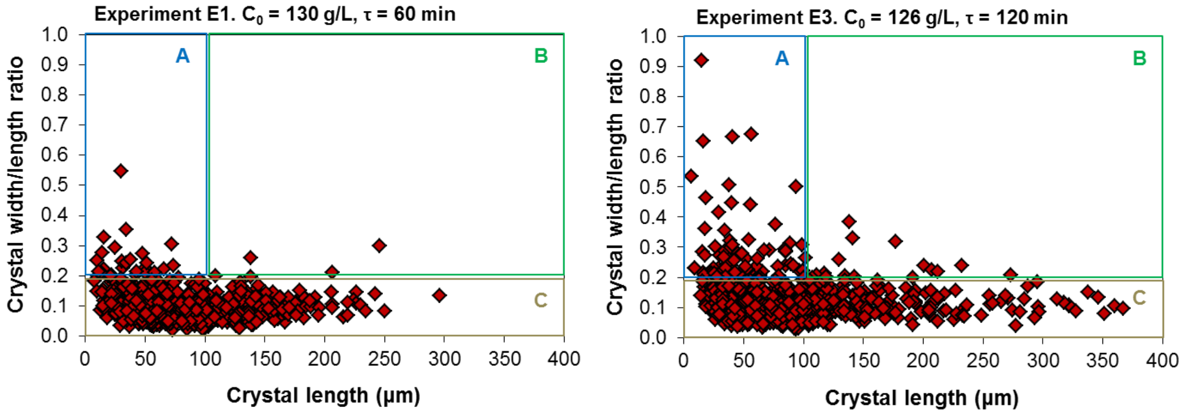

Figure 4.10 Crystal shape diagrams for E1 and E3, containing approximately 700 crystals each. The diagrams have been divided in three regions (A, B, C) to facilitate the discussion.

Inspection of Figure 4.9 reveals that over 95% of the crystals fall in region C (width/length < 0.2) for most of the experiments. For a system with negligible breakage where the growth rates in each dimension have a linear dependency, the mean aspect ratio should remain constant regardless of crystal size. As it can be seen from Figure 4.10, the distribution broadening from Figure 4.9 occurs preferentially at the lower crystal lengths (region A). Runs E1 and E3 were conducted at the same feed concentration and temperature but at different residence times. It can be inferred from region C in Figure 4.10 that a longer residence time leads to an increase in the length of the crystals in the magma. However, longer crystals and extended holding times are more susceptible to crystal fracture. The increased population in region A is presumably a consequence of breakage, leading to the appearance of crystal fragments with a short length and a square-like 2D projection.

The appearance of these fragments would be accompanied by a broadening of the crystal shape distribution, as those crystals that break near the edges will still retain a crystal shape within a reasonable value. However, this broadening is very small in this system due to the limited extent of crystal breakage. From the samples obtained in the first stage, the magma in E3 presents the worst case scenario for this phenomenon.

4.4.6 Crystal breakage in multistage crystallization

To investigate the impact of suspension transfer and second stage crystallization on crystal breakage, samples of the crystallization magma were collected at three different locations: at the first MSMPR stage, at the outlet of the pump transferring the magma between crystallizers (P3), and at the second MSMPR stage. Experiment E7 was selected for this purpose, as it gave the highest suspension density in the first stage crystallizer. In Figure 4.11, a sample of the optical microscopy images of the three points are displayed, accompanied by the shape diagrams of each sample. To facilitate the discussion, the same has been done for the full-scale batch product that is used as a starting suspension in the MSMPR crystallizer.

Note that the largest difference in crystal shape occurs at the pump transferring the suspension from MSMPR 1 to MSMPR 2. Suspension transfer takes less than 5 seconds, and thus it may be assumed that the extent of crystallization is negligible during product removal. The observed variations are solely related to crystal breakage during pumping.

Interestingly, the crystal shape distribution is retained in the second crystallizer. The experiment yielded a solute recovery of 78.0%, with the first 65.9% being recovered in the first crystallizer. Similar to other systems, the second MSMPR unit has a small impact on the crystal size distribution.[66,74] This is because most of the solute mass is recovered in the first stage. The second stage receives a suspension as feed, and the large amount of crystals provide an extended area for solute deposition. Furthermore, the second stage operates at lower temperatures and reduced supersaturations, which limit the overall kinetics of crystallization.

The shape diagram presented in Figure 4.11 does not show a constant, size-independent shape for the formulation product. As suspected from the SEM images in Figure 4.8 and supported by the observed breakage in P3, the API crystals are highly sensitive to crystal breakage in process equipment. Considering the similarity between the crystallization magma at the outlet of P3 and that of the full-scale batch product, and since crystal breakage appears to be heavily dependent on crystal length, it may be assumed that the different crystal shape comes from crystal breakage during downstream processing. Regardless of the source, tablet formulation will certainly lead to API crystal breakage. Thus, there is no point in designing a gentle treatment from an industrial perspective.

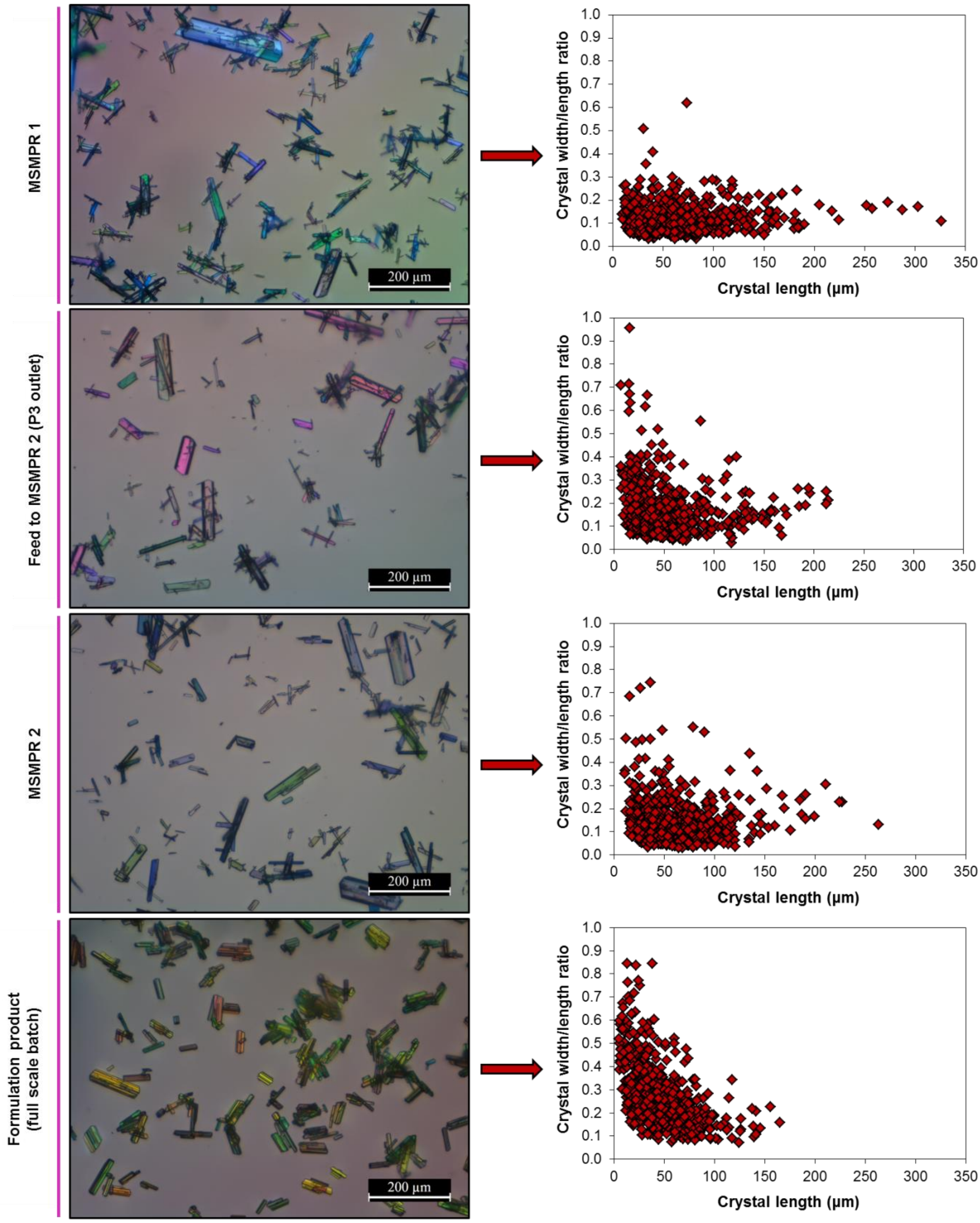

Figure 4.11 Tracking crystal breakage with optical microscopy. An example of a magma picture is placed side by side with the 2D shape diagrams for 700 crystals (multiple pictures) at three sampling points in the MSMPR cascade and for the commercial batch product. This figure, read from top to bottom, follows the hypothesis described in Figure 4.1.

As discussed in Section 4.2.1, unless crystal breakage occurs at the plane perpendicular to the characteristic dimension, the volumetric crystal size distribution will remain unchanged. The smaller volume of the broken crystal is compensated by the birth of a new crystal, a ‘fragment’ of the original, that maintains the same size for all the crystal dimensions but one. The total volume from the two fragments will still remain the same. The volumetric crystal size distributions of run E7 based on crystal width and crystal length have been reported in Figure 4.12, together with the quantitative shape distributions corresponding to the diagrams in Figure 4.11. Note that the accuracy of the size distributions in Figure 4.12 is heavily limited by the small sampling number, and thus care should be taken while assessing the information. However, the observed 35% reduction in the mean crystal length is significantly higher than the previously studied measurement reproducibility (see Appendix B), and it is further supported by the significant shape variations observed in Figure 4.11. The obtained distributions support that crystal breakage affects the volumetric crystal length distribution while the effect on the width distribution is not detectable.

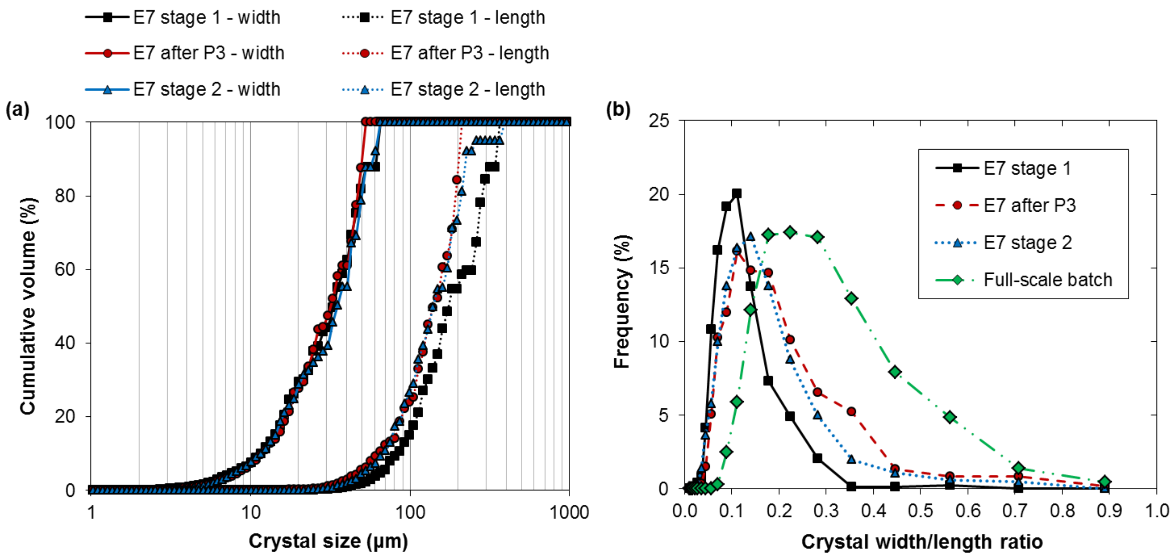

Figure 4.12 2D crystal size (a) and shape (b) distributions at different locations of the steady state system in experiment E7.

The consistency of one of the size distributions with crystal breakage provides a significant advantage for the early assessment of crystal quality. Contrary to the crystal size distributions from laser diffraction, the crystal width distribution is expected to remain consistent through downstream production, as it is not based on projected area but on crystal dimensions that are not sensitive to breakage. In addition, since crystals tend to break on their smallest plane, the second largest dimension (typically defining filterability) is not affected. Thus, focusing on these size distributions simplifies the development of the crystallization process and the later modelling of the downstream unit operations.

4.5 Optimization for a relevant crystal dimension

4.5.1 Selection of a mathematical model

Using a common approach for MSMPR crystallizers, the crystallization rate equations have been determined by fitting a mathematical model that simultaneously solves the population balance and the mass balance for each crystallizer.

Determination of multiple crystal dimensions enables the application of multidimensional population models to predict crystal size and shape. As demonstrated by quantitative image analysis, the crystal shape is independent of the crystal growth rate in the MSMPR crystallizer, and only crystal breakage induces significant changes in the 2D projection of the magma. Given that most of the crystal breakage occurs in the pumps and that this phenomenon is hardly avoidable during downstream processing and formulation, a unidimensional population model based on crystal width is sufficient for this system. The model will be using a shape factor that assumes negligible crystal breakage. Since the obtained populations assume that the crystals never broke in the first place, this approach allows for the independent evaluation of size-dependent growth from the logarithmic population density plot.

The use of population models based on a non-fragile dimension has limitations. If the extent of crystal breakage was significantly higher, the increased amount of dislocations in the broken crystal plane would lead to a faster growth rate in the perpendicular dimension. In addition, even though the increase in surface area upon needle/plate breakage is relatively small, extensive fracture will cause a significant increase in the available surface area for crystal growth. Consequently, the second MSMPR would exhibit lower supersaturations and affect the rates of crystal growth in the other crystal dimensions. Finally, the crystals do not necessarily have to break on the same dimension, or following a straight plane. High degrees of crystal breakage could affect more than one dimension or produce an excessive amount of fines. This approach has been valid for the system studied here, but further consideration would be required for each case.

4.5.2 Population and mass balances for the MSMPR cascade

The unidimensional population balance of a steady state MSMPR crystallizer with negligible agglomeration and breakage in the characteristic dimension was described by Randolph and Larson as in eq 4.1.[56]

$$\frac{d(Gn_i)}{dL} + \frac{n_i - n_{i-1}}{\tau} = 0 \tag{4.1}$$

When the system follows McCabe's ΔL law, the crystal growth rate is not a function of crystal size. The population balance in eq 4.1 can then be integrated for both crystallizers, using the boundary condition $n(0) = n^0$ and considering that the first crystallizer is not seeded:

$$n_1(L) = {n_1}^0 exp\left(\frac{-L}{G_1\tau_1}\right) \tag{4.2}$$

$$n_2(L) = {n_2}^0\, exp\left(\frac{-L}{G_2\tau_2}\right) + {n_1}^0\left[\frac{G_1\tau_1}{G_1\tau_1 - G_2\tau_2}\right]\left[exp\left(\frac{-L}{G_1\tau_1}\right) - exp\left(\frac{-L}{G_2\tau_2}\right)\right] \tag{4.3}$$

Equations 4.2 and 4.3 define the population balance in the first and second crystallizer, respectively. n^0 is the population of zero-sized nuclei and it can be calculated from the rates of nucleation and crystal growth:

$${n_i}^0 = \frac{B_i}{G_i} \tag{4.4}$$

The suspension density for each crystallizer can be obtained from the third moment of the population balance, the density of the solid phase ρ and a volumetric shape factor k_v, assuming that the crystal shape is independent of crystallization conditions.

$$M_T = k_v\rho\int_0^\infty L^3 n dL \tag{4.5}$$

The mass balance for the API in each crystallizer can be written as

$$C_0 = C_{ml} + M_T \tag{4.6}$$

Finally, the rates of nucleation and crystal growth can be expressed from semi-empirical equations, where the mass balance in eq 4.6 can be incorporated to express supersaturation as a function of suspension density and feed concentration:

$$B = k_{b0} exp\left(\frac{-E_b}{RT}\right){M_T}^j\left(\frac{C_0 - M_T - C_{sat}(T)}{C_{sat}(T)}\right)^b \tag{4.7}$$

$$G = k_{g0} exp\left(\frac{-E_g}{RT}\right)\left(\frac{C_0 - M_T - C_{sat}(T)}{C_{sat}(T)}\right)^g \tag{4.8}$$

Equations 4.2, 4.5, 4.7 and 4.8 will have a single solution that satisfies both the mass balance and the population balance in the first crystallizer. For a given feed concentration, crystallization temperature and residence time, this system of equations was solved using the MATLAB function *lsqnonlin* to find the values of B, G, M_T and n in the first MSMPR stage.

Then, eqs 4.3, 4.5, 4.7 and 4.8 were solved in the same way to find the relevant conditions in the second stage.

4.5.3 Determination of the kinetic rate equations

Prediction of the steady state population requires knowledge on the crystallization rate equations, the density of the solid phase and the shape factor of the crystals. The rates of nucleation and crystal growth as described in eqs 4.9 and 4.10 are based on seven parameters that can be obtained by fitting the prediction model to the experimental population distributions.

The bulk density of the API was determined by measuring the volume increase in a graduated cylinder after suspending 20.29 g of the crystalline product in 60 mL of a saturated solution of Melitracen HCl in ethanol. Before the measurement, the suspension was agitated using magnetic stirring to ensure that the crystals are properly dispersed and the air had been removed from the sample. The obtained density for the solid API was 1280 kg/m^3.

The volumetric shape factor based on crystal width was established from image analysis of the crystallization magma. A mean aspect ratio between crystal length and width of 0.89 was determined from the mode of the crystal shape distributions of the experiments in single stage crystallization. Based on SEM observations, the crystal height was assumed to be proportional to the crystal width for all the studied conditions. Assuming that the height is a third of the crystal width, the k_v value was calculated from the ratio between crystal dimensions:

$$l = \frac{w}{0.089} \qquad h = \frac{w}{3} \tag{4.9}$$

$$V_c = k_v L^3 = lhw \underset{L=w}{\Longrightarrow} k_v = \frac{1}{0.089 \cdot 3} = 3.74 \tag{4.10}$$

For a given shape factor and solid density, the experimental population distribution can be obtained using eq 4.11.

$$nexp(w) = \frac{vol(w) M_{T,exp}}{\rho k_v w^3 \Delta w} \tag{4.11}$$

The obtained population distributions follow the trend displayed in Figure 4.13. The linear nature of the logarithmic population density plot demonstrates that the system follows McCabe's ΔL law, and thus that the selected size-independent growth model is appropriate for this system. Note that crystal widths smaller than 2.5 μm deviate from the linear trend presenting lower populations. This behavior is presumably related to the limitations of image analysis. Crystals of this size are too thin to be detected and analyzed at the used microscope magnification, and thus a smaller amount is detected during image analysis. Since the volumetric mean widths in this work are at the order of 20 to 40 μm, and crystals below 2.5 μm never accounted for more than 0.3% of the suspension mass, this limitation should not have a significant impact on the accuracy of the model.

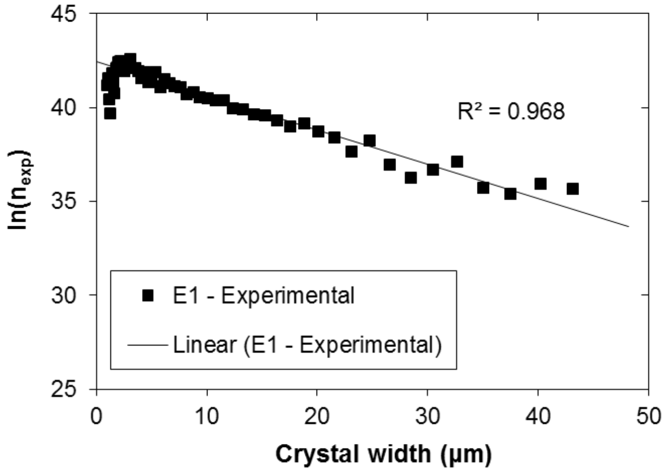

Figure 4.13 Logarithmic population density plot for run E1, including a linear fit for the size range from 3 to 40 μm.

The fluctuations observed for the larger sizes in the population density plot are a consequence of the analysis method. In this work, 700 crystals were sufficient to detect variations in the crystal size distribution and to obtain a mean size with reasonable accuracy. However, this sample number does not allow to obtain a smooth distribution at the larger crystal sizes, where a single channel can include less than 5 crystals. Those crystals, despite being a small amount, constitute a large fraction of the suspension mass because of their size.

Based on the number of crystals that are present in the larger bins, a smooth distribution would require a sample number 1-2 orders of magnitude higher. This is not practical for manual image analysis, but could easily be achieved with an appropriate algorithm. Fluctuations in the volumetric size distribution, as observed in Figure 4.12, produce a scatter in the population density plot and increase the uncertainty of the determined experimental kinetics. To limit the impact of this scatter, the effective rates of nucleation and crystal growth were fitted for populations between 3 and 40 μm.

The kinetic parameters based on crystal width were obtained using the MATLAB function *lsqnonlin*. Based on an initial guess for the parameter vector $\theta = [k_{bo}, E_b, j, b, k_{g0}, E_g, g]$, the best fit of kinetic parameters is obtained by solving the least squares minimization problem:

$$\underset{\theta}{min}\ F = \sum_{E1-9} \sum_{w=3\ \mu m}^{40\ \mu m} \left[\ln\left(nexp(w)\right) - \ln\left(n(w)\right)\right]^2 \tag{4.12}$$

To account for the typically small supersaturations in the second crystallization stage, the population data from the 13 crystallizers in E1 to E9 (including both stages) were used for parameter estimation. The obtained kinetic parameters for the best fit to eq 4.12 are summarized in Table 4.3.

Table 4.3 Fitted kinetic parameters for MSMPR crystallization of Melitracen HCl from ethanol.

Parameter	Value	Units
k_{b0}	$4.79 \cdot 10^{22}$	$m^{-3}s^{-1}$
E_b	73.0	kJ/mol
j	0.56	-
b	2.60	-
k_{g0}	13.1	m/s
E_g	52.5	kJ/mol
g	0.87	-

The activation energies for nucleation and crystal growth are in a similar order of magnitude with those found for MSMPR crystallization of other organic compounds,[73,74,83,189] and show the significant temperature dependency of the rates of crystallization. The relative kinetic order i=b/g has a value of 3, indicating that for the same suspension density shorter holding times lead to a significant reduction in the crystal size.[56] This is consistent with our experimental observations. Furthermore, as expressed by the values of b and j, nucleation is highly supersaturation dependent and receives a small impact from suspension density.

4.5.4 Model verification

The quality of the data fitting and accuracy of the prediction model are verified in two different ways. First, the model predicted rates of nucleation, crystal growth and suspension densities are compared to the values obtained experimentally. The experimental kinetics are calculated from the best fit to eqs 4.2 and 4.3, incorporating the mass balance into the calculation by means of eq 4.5. The comparison between experimental and fitted kinetics is displayed in Figure 4.14.

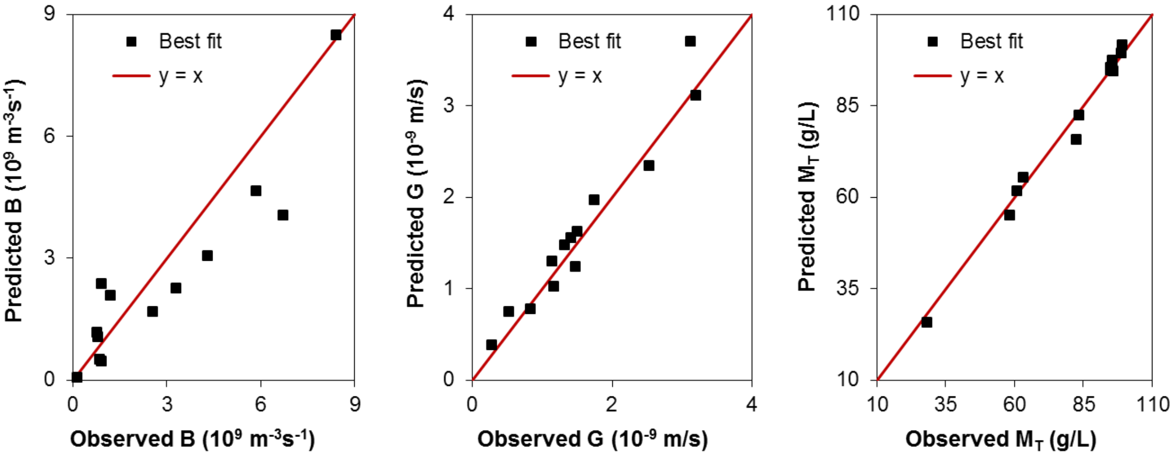

Figure 4.14 Correlation between the observed and predicted kinetics. The values correspond to the 13 crystallizers in 9 runs, including both single stage and multistage crystallization.

The fitted rate equations offer a very good prediction for the suspension density and growth rate in the crystallizers. However, the steady state nucleation rates are poorly predicted by these parameters. The observed deviations are a consequence of multiple factors. It is important to clarify that the plots in Figure 4.14 display the combined experimental error and the fitting error. Since the experimental populations are determined from the volumetric size distribution, any scatter in this distribution caused by the relatively small sampling size will inevitably change the observed system kinetics. This problem is aggravated in multistage crystallization, where kinetics in the second stage depend on the fitted values for stage 1. In addition, since the experimental kinetics are forced to comply with the mass balance, deviations in the slope of the logarithmic distribution will cause uncertainties in the growth rate that will propagate to the calculated nucleation rate.

To quantify the extent that these uncertainties will have on the quality of prediction, an experimental verification is conducted in multistage crystallization. Given that the objective of the model is to predict yields and crystal size distributions, the experimental verification approach will provide an indication of the impact of the estimation errors on crystallization outcomes without including the error propagation in the calculation of experimental kinetics. For the verification experiment, crystallization temperature and residence time were varied simultaneously, using different conditions than those used in the experiments for data fitting. The experimental conditions and predicted suspension densities are summarized in Table 4.4.

Table 4.4 Steady state conditions of the verification experiment and prediction error.

C_0 (g/L)	MSMPR stage	T (°C)	τ (min)	$\text{Yield}_{\text{obs}}$ (%)^b	$\text{Yield}_{\text{pred}}$ (%)^b	Error (%)
129.5 ± 0.2	S1	25	40	56.7 ± 0.4	57.6	1.6
	S2	10	40	76.0 ± 0.6	78.1	2.7

At the verification conditions, the model overestimates the steady state yield in both crystallizers. Considering that the error in the first unit propagates to the second stage, the estimation error is approximately 1.5% on each crystallizer. Slightly lower estimation errors were obtained by Power *et al.* in two stage MSMPR crystallization of benzoic acid.[74] Regarding crystal size distribution, the model offers a good prediction for this experiment as it is shown in Figure 4.15.

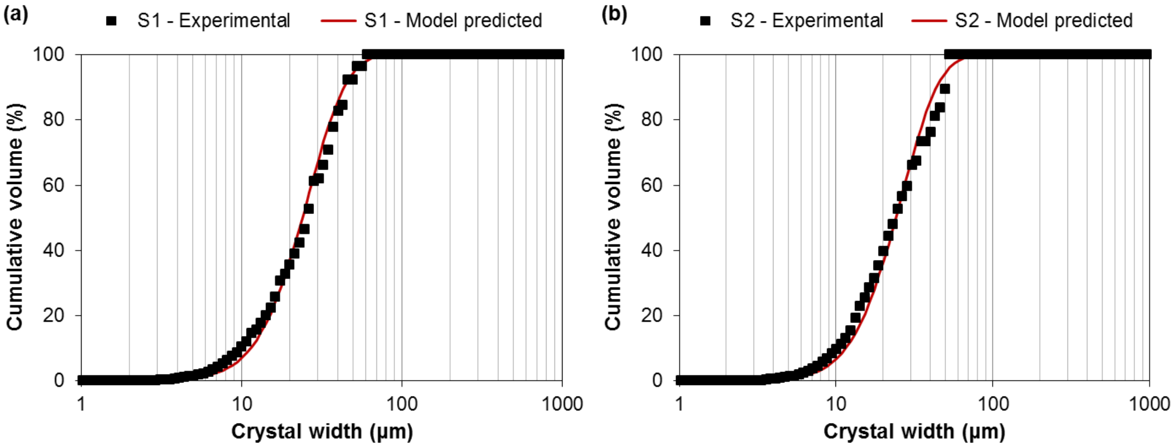

Figure 4.15 Comparison between the observed and predicted crystal width distributions for the verification experiment. (a) MSMPR stage 1. (b) MSMPR stage 2.

4.5.5 Attainable regions of crystal width

The fitted kinetic rate equations were used together with the prediction model to assess the limitations for crystal width distribution control in the investigated setup. The mass based mean crystal width is defined as the fraction between the fourth moment and the third moment of the population distribution:[56]

$$w_{4,3} = \frac{\int_0^\infty w^4 n dw}{\int_0^\infty w^3 n dw} \tag{4.13}$$

Then, an optimization problem was formulated to find the attainable regions of mass based mean crystal width for single stage and two stage MSMPR crystallization.

Single stage:

$$\underset{C_0, T, \tau_{tot}}{Minimize/maximize} \quad w_{4,3}$$

$$\begin{aligned} &Subject\ to: \\ &10\ °C \le T \le 30\ °C \\ &\sigma \le 0.6 \\ &M_T \le 100 g/L \\ &C_{sat,15\ °C} \le C_{ml} \le C_{sat,20\ °C} \\ &Yield \ge 65\% \end{aligned}$$

Two stages:

$$\underset{C_0, T_1, T_2, \tau_1, \tau_2}{Minimize/maximize} \quad w_{4,3}$$

$$\begin{aligned} &Subject\ to: \\ &10\ °C \le T_i \le 30\ °C \\ &\sigma_i \le 0.6 \\ &M_{T,i} \le 100 g/L \\ &C_{sat,15\ °C} \le C_{ml,2} \le C_{sat,20\ °C} \\ &Yield \ge 65\% \\ &\tau_{tot} = \tau_1 + \tau_2 \\ &0.25\tau_2 \le \tau_1 \le 4\tau_2 \\ &T_2 \le T_1 \end{aligned} \tag{4.14}$$

Most of the optimization constraints are shared between the two configurations, as they are related to the system limitations and the expected operation of an implemented process. The constraints on temperature, supersaturation and suspension density are based on the limitations of the kinetic parameters (fitted for values within this range) and the lab-scale experience for this system. At this scale and from previous experience with the system, higher supersaturations lead to fouling at the impeller and higher suspension densities promoted frequent clogging of the product removal stream. These constraints could be varied on a higher scale or for a different setup, provided that the system can successfully sustain the steady state at these conditions. To obtain a crystallization magma that is not subject to significant CSD variations in the transfer lines, the mother liquor concentration at the end of the crystallization process is set to have a saturation temperature between 15 and 20 °C. Furthermore, the step yield of the crystallization process must be higher than 65% to obtain an efficient separation. For the two stage configuration, the residence times are constrained so that none of the crystallizers will be more than four times larger than the other. In addition, a temperature constraint is set so that the second crystallizer is never operating at a higher temperature than the first stage.

The optimization algorithm is solved using the MATLAB function *fmincon*. This function finds the set of conditions that minimize the value of $w_{4,3}$ based on a given initial guess. Especially for two stage crystallization, where the function has 5 input parameters and a large number of constraints, the obtained minimum is highly sensitive to the initial guess. To verify that the function has found the absolute minimum, 10,000 Monte Carlo simulations were conducted with random values for the input parameters. In those simulations, the feed concentration was limited between 80 and 135 g/L, the temperatures between 10 and 30 °C, and the total residence time between 60 and 120 min. Those simulations that did not accomplish the process constraints were discarded. The attainable regions and the results from this verification are plotted together in Figure 4.16.

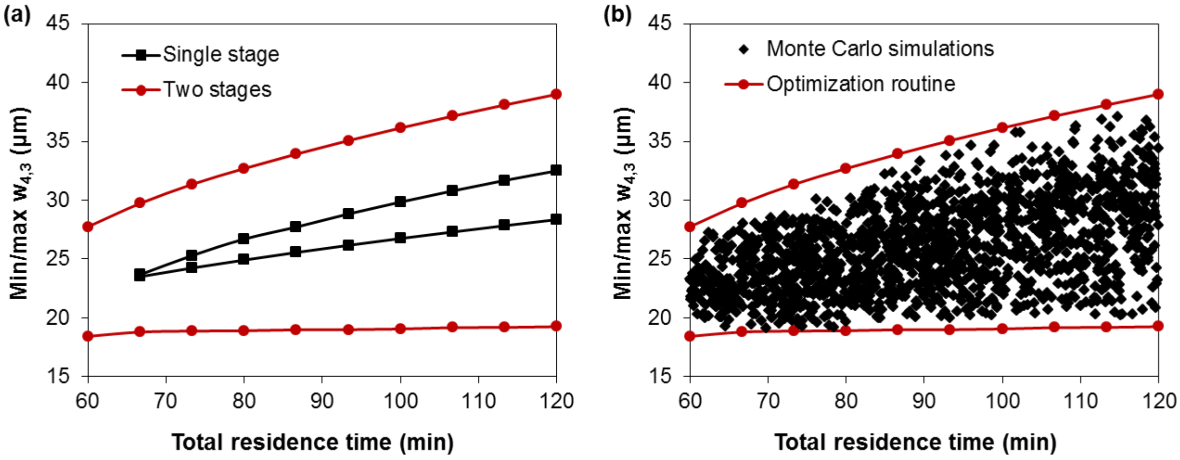

Figure 4.16 (a) Attainable regions for crystal width in the single stage and two stage MSMPR setup. (b) Comparison with the Monte Carlo simulation results.

The obtained attainable regions for the two stage system show a good agreement with the Monte Carlo simulations, indicating that the obtained attainable regions are close to the absolute minimum/maximum size for these constraints. As expected due to the increased degrees of freedom, two stage crystallization offers a much better control of the crystal size for this compound. The attainable regions have a similar shape to what has been seen previously, becoming narrow with shorter residence times until the minimum and maximum sizes eventually converge.[80] This convergence point was not reached for the two stage system as total residence times below 60 min were not investigated. The conditions for minimum and maximum attainable widths are reported in Table 4.5.

Table 4.5 Conditions for minimum and maximum attainable crystal widths in two stage MSMPR crystallization. These limits are subject to the constraints in the optimization problem.

$w_{4,3}$ (µm)	C_0 (g/L)	T_1 (°C)	τ_1 (min)	T_2 (°C)	τ_2 (min)	Yield (%)[a]
Min: 18.4	99.7	18	15	10	45	65
Max: 39.0	130.0	30	94	10	26	73

[a] The yield is calculated as $100(C_0\text{-}C_{ml})/C_0$.

Due to the dependence of crystallization kinetics on temperature and the preferential increase of the nucleation rate at high supersaturations, the largest crystal sizes are obtained by keeping the first stage temperature at 30 °C and using long residence times in the first step. This approach ensures that the first stage operates at low supersaturations promoted by the faster kinetics and the longer holding times. To obtain smaller crystal sizes, the temperatures and residence times in both stages are adjusted so that the highest supersaturation (0.6, according to the constraints) is maintained in each crystallizer. Similar conditions were obtained for the minimum and maximum observed crystal widths using Monte Carlo simulations.

Image analysis from the formulation crystals supplied from full-scale batch production gave a mass based mean crystal width of 19.5 μm. Based on this value, single stage crystallization will hardly produce crystals of similar size unless the process constraints are significantly softened. Consequently, crystallization in two MSMPR stages is the most suitable. However, the process will likely have to operate at very high supersaturations and low yields. A proper study of the fouling limits for the full-scale unit would be required before selecting a set of process conditions. It is likely that the system will operate with a first crystallization unit exhibiting a short residence time and a temperature close to 20 °C. The second unit will have a size approximately 3 times larger, with an operating temperature close to 10 °C. Based on the production rates for the conditions of minimum size in lab-scale, the full-scale crystallization system would require an approximate total volume of 20 L (5 + 15 L) to produce 10 tons of API in 300 days of operation.

4.6 Conclusions

A two stage continuous MSMPR crystallization system was characterized using quantitative image analysis of the crystallization magma. The effect of process conditions on crystal shape was studied from variations in the crystal aspect ratio with the steady state supersaturation and temperature. After demonstrating that the crystal shape does not vary with process conditions or crystal size, the effect of residence time and number of stages on crystal breakage was quantified. It was found that crystal breakage occurs mainly in the pump transferring the suspension between crystallizers, and that it leads to a similar shape distribution as that found in the full-scale batch product that is subject to mechanical stress in downstream production. A mathematical model was developed for the prediction of crystal widths in single stage and two stage crystallization, for which the rate equations for nucleation and growth based on this dimension were determined. The predicted crystal width is resistant to a moderate extent of crystal breakage as demonstrated from analysis of the full-scale batch and MSMPR product.

5 Effect of gas dispersion on nucleation rates

This chapter has been written in a manuscript format. A modified version has been published in the peer-reviewed journal *Crystal Growth & Design* as:

Capellades, G.; Kiil, S.; Dam-Johansen, K.; Mealy, M. J.; Christensen, T. V. & Myerson, A. S. *Crystal growth & design* **17**, 3287-3294 (2017). DOI: 10.1021/acs.cgd.7b00267

5.1 Abstract

From disruption of the supersaturated solution to improved mass transfer in the crystallizing suspension, the introduction of a moving gas phase in a crystallizer could lead to improved rates of nucleation and crystal growth. In this work, saturated air has been injected to batch crystallizers to study the effects on formation of the first crystal and subsequent turbidity build-up. To account for the typically large sample-to-sample variation, nucleation rates were evaluated for a large number of replicates using probability distributions of induction times. The slope and the intercept of the distributions were studied independently, allowing the simultaneous determination of the mean induction time and a certain detection delay related to the rate of crystal growth after formation of the first nucleus. Injecting saturated air in aqueous glycine solutions, the average detection delay was reduced from 69 min to 13 min, and the mean induction time decreased from 128 min to 36 min. The effect on aqueous solutions of L-arginine was less apparent, with a detection delay reduction from 15 min to 3 min, and no significant changes on the rate of primary nucleation. These results demonstrate the potential of this technique for reduction in nucleation induction time and improved mass deposition rates in crystallization operations.

5.2 Introduction

Crystallization is an important separation technique that is extensively used in the chemical, food and pharmaceutical industries. Especially in pharmaceutical production, the crystallized solids are subject to strict quality requirements regarding crystal purity, polymorphism and size distribution.[100] Nucleation plays a fundamental role when defining these quality attributes. Thus, an important part of the recent crystallization research is aimed at achieving a better understanding of this phenomenon.[31]

Transition to the crystalline phase starts with the formation of the first nucleus in a supersaturated solution. This event is stochastic and based on a certain probability that is related to the primary nucleation rate.[36–38] Several factors can affect the probability of observing a primary nucleation event in a crystallizer, mainly: sample volume, supersaturation, temperature, mixing and the presence of impurities.[38,39] Once the first nucleus is formed, solute crystals are present in the system and secondary nucleation can occur. Systems with crystals present have the advantage of producing additional nuclei through secondary nucleation thus increasing the mass deposition rate due to the higher surface area present in the crystalline phase. Secondary nucleation is highly dependent on agitation and becomes the predominant nucleation mechanism at low supersaturations.[39] For the operation of industrial crystallizers, understanding the rates of nucleation and crystal growth is critical to obtain a product with the right size and form.[100,129] A method to selectively enhance one of the two rates can therefore lead to significant advantages in process control.

The use of probabilistic methods to investigate nucleation kinetics dates back from more than 60 years. Some of the first studies were based on solidification in small droplets, using supercooled mercury, tin and water.[195–197] In recent work, probability distributions of induction times have been applied for the evaluation of new methods for control of nucleation rates and polymorphism by using polymer surfaces or gels.[198–201] The extended use of primary nucleation studies led to the development of novel equipment employing microfluidics to accommodate a large number of replicates in a single experiment.[202–204]

Dispersion of a saturated gas in the active crystallization volume has been postulated to enhance primary nucleation through different mechanisms. Bubble flow and collapse cause a mechanical disruption in the supersaturated solution that could have a similar effect to that seen with the application of mixing. In addition, it is frequently stated that the gas-liquid interphase could promote nucleation by acting as a heterogeneous nucleation site.[166,170,172,205,206] In systems limited by mass transfer, mixing induced by the flowing gas would enhance the rate of crystallization at constant supersaturation. When solute crystals are present, perturbations in the flow direction would promote the contact frequency between crystals and enhance the rate of secondary nucleation. These mechanisms would be the most interesting for industrial crystallization, as they would allow gas recirculation without pre-treatment. Alternatively, cold unsaturated gas could be used as a means to induce local supersaturation changes by solvent evaporation and heat transfer.

Previous studies have dealt with the application of gassing to induce nucleation in batch crystallizers.[166,167,170,172] However, due to the complexity of the system and the various ways that gassing could influence primary nucleation, the mechanism is not yet fully understood.

In this study, a probabilistic approach based on induction times has been applied to crystallization under air injection. The statistical significance of kinetic changes caused by the application of gas is evaluated taking into account the existing variation between induction time measurements. The experiments are carried out under continuous saturated air injection and carefully designed to minimize the impact of heat transfer, evaporation or gas expansion on supersaturation of the metastable solutions. Combining the use of probability distributions and a detection method based on sample turbidity allowed decoupling the average time for crystal formation from the time required to achieve a certain solution turbidity. Thus, this study deals with the effect that the presence of a flowing gas would have on (1) the time for formation of the first crystal and (2) turbidity build-up after the first nucleation event.

5.3 Experimental section

5.3.1 Materials

Glycine (≥99.5% purity) was purchased from Alfa Aesar, Haverhill, USA. L-arginine (≥98% purity) was purchased from Sigma-Aldrich, St. Louis, USA. Deionized water was used as the solvent for both compounds. For the experiments involving gas injection, compressed air from the laboratory general supply was selected as the gas phase.

5.3.2 Experimental setup

A schematic of the experimental setup for the air injection experiments is illustrated in Figure 5.1. The air feed is mixed with steam in a boiler and passed through two condensers to remove the excess water. A temperature/relative humidity data logger (Sper Scientific, Scottsdale, USA) is connected to the end of the second condenser to monitor the air properties. Based on the logged data, the heat supplied to the boiler and the temperature of the cooling water are manually adjusted to keep the air saturation with solvent above 95% at 25 °C. The saturated air is distributed to 16 parallel crystallizers through a set of manifolds, and the flow rate at each of the streams is adjusted with an independent needle valve. Air injection is conducted through PEEK™ tubing (Upchurch Scientific®; ID: 0.75 mm, OD: 1/16”), immersed

27 mm from the top of the vial cap. To prevent leaks in the setup and cooling from air expansion, the pressure of the injected air is measured with a manometer and kept below the lower detection limit (0.34 barg). Accordingly, air cooling from Joule-Thomson expansion is maintained under 0.08 °C.[207] A Crystal16® multiple reactor setup (Avantium Research & Technology) is used to control the temperature and agitation rate in the crystallizers. The crystallizers are cylindrical vials with a maximum capacity of 2 ml and 10 mm internal diameter. Sample mixing is obtained through magnetic stirring with PTFE agitation bars (cylindrical, 8 mm x 3 mm). During the induction time measurements, the nucleation event is detected by the Crystal16® unit as a drop in light transmission through each sample.

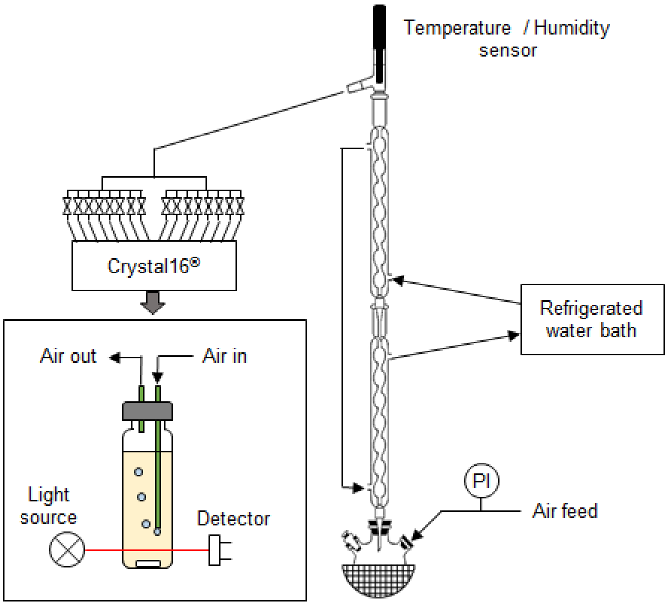

Figure 5.1 Schematic diagram of the experimental setup for the induction time measurements with saturated air injection.

5.3.3 Sample preparation and Crystal16® program

60 g stock suspensions are prepared with different weight fractions of the corresponding solute and demineralized water. These suspensions are dissolved at 60 – 70 °C before the clear solution is pipetted to the sample vials. A sample volume of 1.40 ml is selected for the experiments throughout this work.

To ensure that the induction time measurements start from a crystal free solution, the unit is programmed to pre-heat the samples to at least 10 °C above their saturation temperature for 30 minutes. The samples are then quenched (3 minutes) and the induction times are measured at 25 °C with a studied time frame of 300 minutes for glycine and 150 minutes for L-arginine.

5.3.4 Induction time measurements at variable supersaturations

A first set of induction time measurements was conducted to quantify the effect of supersaturation on nucleation and growth kinetics. These experiments have three functions: (1) to demonstrate that the induction times follow a Poisson distribution for the studied range of kinetics, (2) to determine a supersaturation ratio for the experiments with air injection, and (3) to study the sensitivity of each solute to concentration changes that could arise from solvent evaporation. The measurements were conducted at 300 rpm and in the absence of injection tubing. The studied supersaturation ratios are 0.20, 0.23, 0.26, 0.31, 0.42 for glycine[208] and 0.23, 0.29, 0.35, 0.46, 0.58 for L-arginine.[209] Here, the supersaturation ratio is defined as $\sigma = (C - C_{sat}(25\ °C))/\ C_{sat}(25\ °C)$, where C is the solute weight fraction at the stock solution and $C_{sat}(25\ °C)$ is the solute weight fraction at the saturated solution at 25 °C.

5.3.5 Crystallization under continuous air injection

A series of induction time measurements were conducted using the setup illustrated in Figure 5.1. These experiments were performed with different air flow rates while keeping a constant supersaturation and mixing (300 rpm) in the samples. Reference measurements were conducted without air injection while using the same tubing and immersion.

The temperature of the samples was kept at 25 °C throughout the induction time measurements to prevent condensation and significant cooling in the manifold system. The supersaturation ratios for the aqueous glycine and L-arginine solutions were maintained at 0.20 and 0.23, respectively. These values were carefully selected so that at least 50% of the samples crystallize within the measurement time frame, giving enough points for data treatment, and to ensure that the detection delays are large enough to study changes in the rate of turbidity build-up. Lower supersaturations were avoided as the attainable turbidities were not high enough for a clear detection.

The temperature of the samples at the pre-heating step was maintained at 50 °C for all the samples. To minimize solvent evaporation during this step, the air flow was disconnected until two minutes before crash cooling. The air flow rate was then visually adjusted for each of the streams and the system was videotaped for its later quantification.

At the end of the experiments, the weight loss was measured for each of the samples to quantify the effect of solvent evaporation on supersaturation. Then, the crystallized samples were filtered together and washed with demineralized water. To identify possible changes in the crystallized polymorphs, X-Ray Powder Diffraction (XRPD) patterns of the filtered crystals were obtained for 2θ between 5°and 40°using an X'PertPro PanAnalytical diffractometer.

5.3.6 Effect of increased mixing on primary nucleation

As an approach to study the mechanism behind the system behavior with air injection, induction time measurements were conducted at constant supersaturation with mixing intensities of 500 and 700 rpm. These measurements provide with a quantitative indication on the sensitivity of the system to changes in the mixing conditions. The experiments were performed in the absence of injection tubing.

5.3.7 Theoretical basis and data treatment

In this work, the observed effects on crystallization kinetics have been evaluated on the basis of probability distributions of induction times. For an unseeded system, the time elapsed between the achievement of a constant supersaturation ratio until formation of the first nucleus has been defined as the induction time. The first nucleation event does not occur at a fixed point in time but it is based on a certain probability, which is a function of the primary nucleation rate and the sample volume. For a system with constant volume, changes in the rate of primary nucleation can be studied from the slope of a Poisson distribution containing the induction time measurements for a large number of replicates.[196]

In practice, the nucleation event is not observed until the crystals have grown to be detectable. Different detection methods can lead to significant variations in the observed induction times. For methods based on microscope observations, the formed nucleus has to grow to a certain size before the nucleation event is confirmed. When detection is based on turbidity measurements, a certain extent of crystallization will be required through primary nucleation, secondary nucleation and crystal growth. For agitated systems at low supersaturation, secondary nucleation and crystal growth tend to be the dominant mechanisms for turbidity build-up. This mechanism is illustrated in Figure 5.2 and further evaluated in Section 5.5.

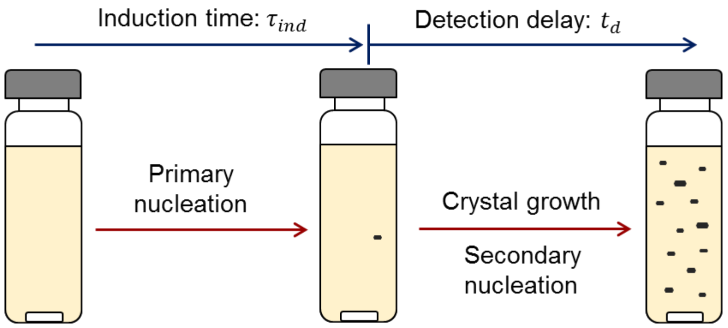

Figure 5.2 Illustration of the steps from achievement of a constant supersaturation to nucleation detection from sample turbidity.

For the same detection instrument and using systems with sufficient agitation, the minimum detectable turbidity will have a fixed value. Thus, variations in the rates of crystal growth and secondary nucleation can be studied from variations in the observed detection delay.

In this work, the induction time measurements were converted into a probability distribution by use of eq 5.1.

$$P(t) = \frac{\xi'(t)}{\xi} \tag{5.1}$$

where $\xi'(t)$ is the number of samples that nucleated before time t, and ξ is the total amount of replicates at the studied conditions.

For a system following a Poisson distribution, the probability $P(t)$ of detecting crystals at time t can be related to the mean induction time τ_{ind} as:[37,210]

$$P(t) = 1 - exp\left(-\frac{t}{\tau_{ind}}\right) \tag{5.2}$$

Equation 5.2 is valid as long as the detection delay is sufficiently small compared to the mean induction time. Especially for slow growing compounds or for detection methods based on sample turbidity, the probability distributions tend to be shifted in the time axis. Previous work accounted for this shift by defining the time for appearance of the nucleus as the time at which nucleation is detected minus the detection delay.[204,211] Equation 5.2 has been modified in a similar way:

$$P(t) = 1 - exp\left(-\frac{t - t_d}{\tau_{ind}}\right) \tag{5.3}$$

where t_d is the average detection delay at the experimental conditions. The values of τ_{ind} and t_d were obtained from linear regression using the logarithmic form of eq 5.3.

5.4 Results

5.4.1 Supersaturation effect on crystallization kinetics

In the first set of experiments, induction times were measured at different supersaturations for the aqueous solutions of the two model compounds. The obtained probability distributions and the fitted kinetics are reported in Figure 5.3 and Table 5.1, respectively.

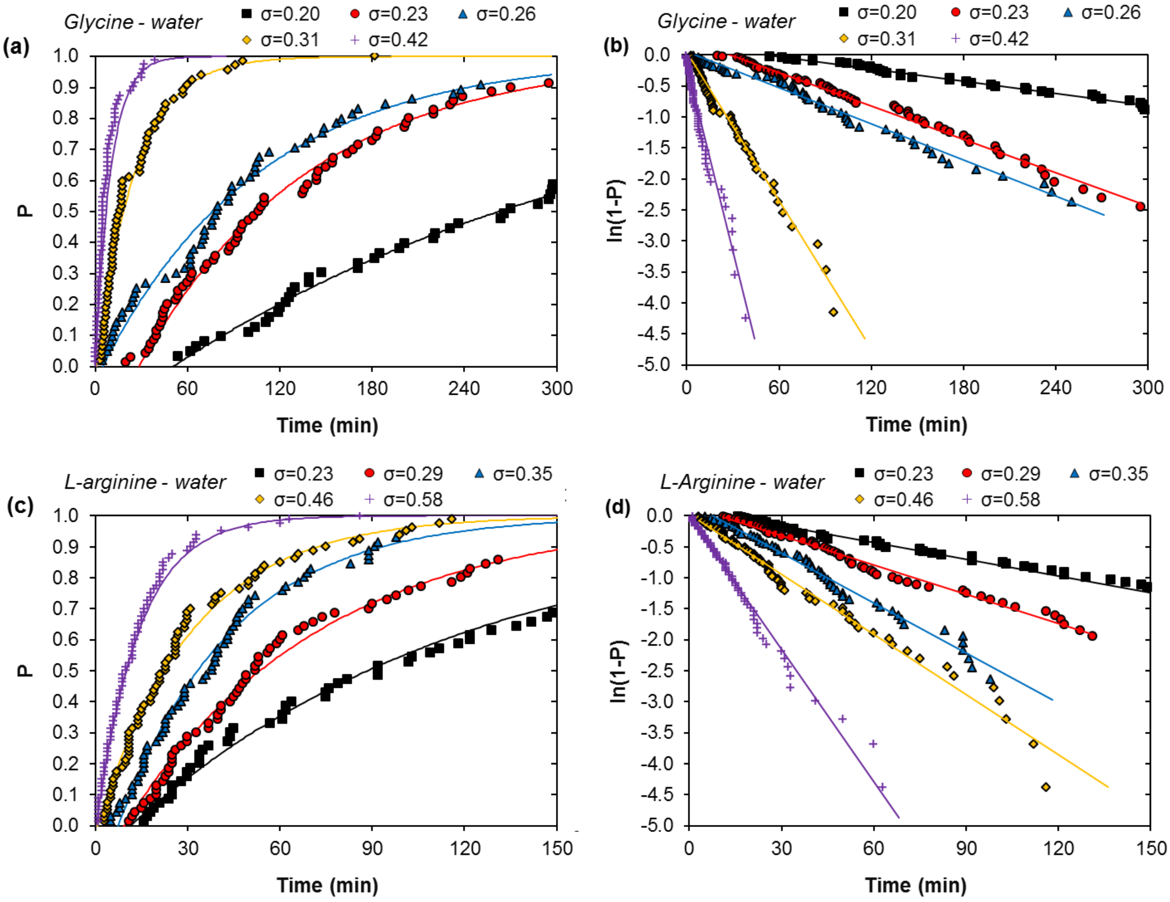

Figure 5.3 Cumulative probability distributions of induction times for aqueous solutions of glycine (a) and L-arginine (c) at different supersaturations. Each point represents the observed induction time of an independent crystallization experiment. (b) and (d) are the logarithmic forms of the probability distributions displayed in (a) and (c), respectively. The solid lines are the theoretical distributions based on the fit to eq 5.3. Sample volume: 1.40 ml. Mixing: 300 rpm. Temperature: 25 °C.

The observed induction times follow a Poisson distribution throughout the experiment time frame, giving a good fit ($r^2 > 0.98$) to the logarithmic form of eq 5.3. As expected, higher supersaturations lead to shorter induction times. The increased rate of primary nucleation is graphically observed from the slope of the distributions and quantified as drop in the mean induction time. The mean detection delay is graphically observed from the intercept of the plots with the time axis. Higher supersaturations lead to faster rates of nucleation and crystal growth, effectively lowering the time required to achieve the minimum detectable turbidity.

Table 5.1 Fitted mean induction times (τ_{ind}) and detection delays (t_d) for different suprersaturation ratios (σ), including 95% confidence intervals from linear regression.

	σ (25 °C)	τ_{ind} (min)	t_d (min)	r^2
Glycine	0.20	305 ± 12	51 ± 7	0.987
	0.23	111 ± 3	28 ± 3	0.991
	0.26	103 ± 3	5 ± 3	0.986
	0.31	25 ± 1	1 ± 1	0.987
	0.42	10 ± 0	-1 ± 1	0.966
L-arginine	0.23	111 ± 4	11 ± 4	0.980
	0.29	64 ± 2	9 ± 2	0.987
	0.35	37 ± 1	7 ± 1	0.986
	0.46	31 ± 1	1 ± 1	0.983
	0.58	14 ± 0	0 ± 1	0.982

5.4.2 Crystallization with continuous air injection

Induction times were measured on samples with constant supersaturation and mixing, using the setup illustrated in Figure 5.1 and a continuous feed of saturated air. The air flow rates at the different experiments were determined in bubbles/min from the recorded video files of 40 random replicates. Using the outer diameter of the injection tubing as a reference, the mean bubble size was determined to be 2.1 mm. Then, the flow rate was converted from bubbles/min to µl/min assuming that the bubbles have a consistent size and a spherical shape. None of the samples presented foaming during the experiments with air injection.

The obtained XRPD data for the filtered crystals can be found in Appendix C. Throughout the experiments in this block, both compounds crystallized in the same form regardless of the air flow rate. These forms are α-glycine and L-arginine dihydrate. For the experiments with glycine-water and air injection at 650 µl/min, traces of γ-glycine were found in one of the measurements. This is the most stable form thermodynamically, but it is rarely obtained at a neutral pH.[212] The probability of obtaining γ-glycine is very small at these conditions, but nucleation of this form is still possible. Since crystallization of γ-glycine was not reproducible, the observation was attributed to this existing low probability.

The observed induction times are reported in Figure 5.4. These results show that air injection had a positive effect on primary nucleation for glycine solutions, giving a 4-fold decrease in the mean induction time for an air flow rate of 1200 µl/min. The effect on primary nucleation is directly related to the flow rate and subject to a minimum value. The smallest studied flow rate (200 µl/min) showed no detectable differences in the induction times.

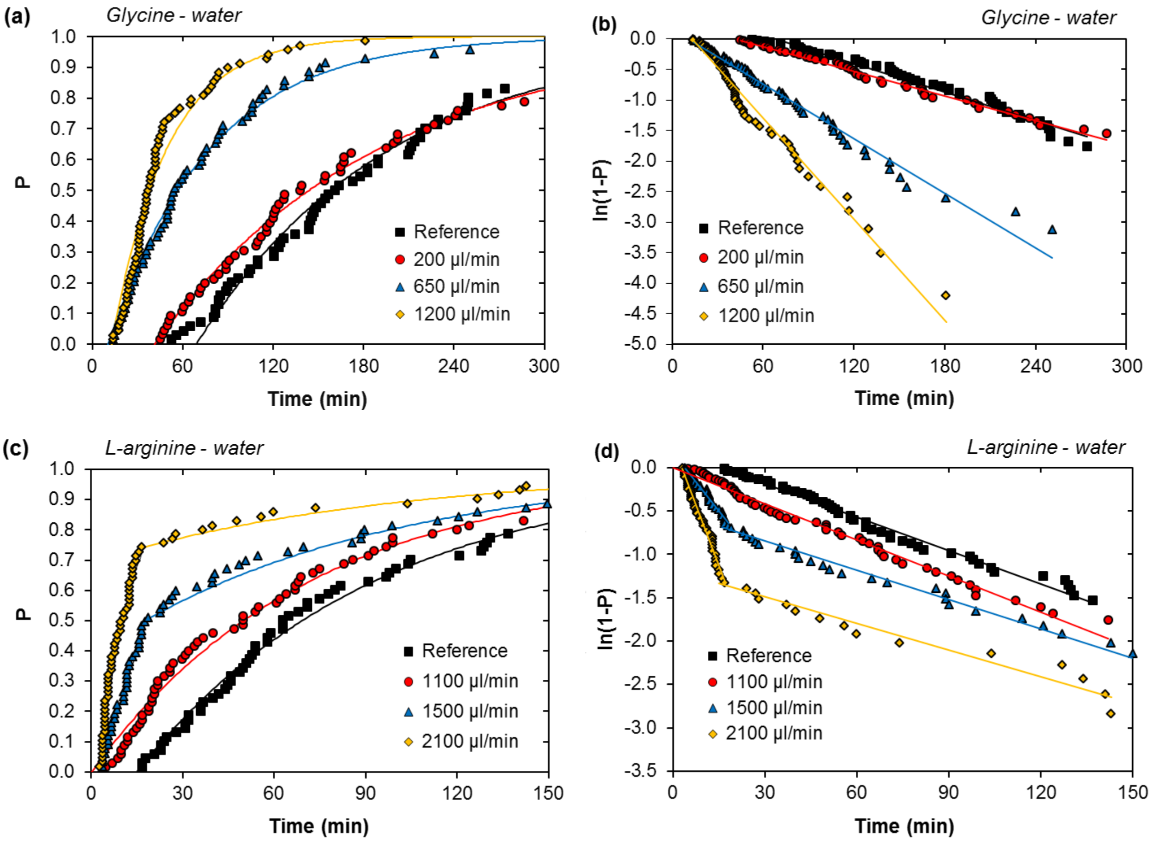

Figure 5.4 Cumulative probability distributions of induction times for aqueous solutions of glycine (a) and L-arginine (c) at different air flow rates. Each point represents the observed induction time of an independent crystallization experiment. (b) and (d) are the logarithmic forms of the probability distributions displayed in (a) and (c), respectively. The solid lines are the theoretical distributions based on the fit to eq 5.3. The distributions for L-arginine at air flow rates of 1500 – 2100 µl/min exhibit a sudden slope change at time = 15 min, indicating the appearance of a second regime with a lower frequency of nucleation. Sample volume: 1.40 ml. Mixing: 300 rpm. Temperature: 25 °C. Supersaturation: 0.20 (glycine) and 0.23 (L-arginine).

Aqueous solutions of L-arginine show a different behavior with the injection of air. For this compound, an air flow rate of 1100 µl/min reduced the detection delay while maintaining a constant induction time. This behavior indicates that, despite the primary nucleation rate is independent of air injection at these conditions, the rates of secondary nucleation and crystal growth are still enhanced.

Flow rates at or above 1500 µl/min gave distributions with two different regimes separated by a sudden slope change at t = 15 min. The appearance of a second regime would be expected if a fraction of the samples had a significantly different primary nucleation rate. In the previous set of experiments (Figure 5.3), similar distribution slopes were obtained with a single regime by increasing the supersaturation of the samples. Thus, this behavior is exclusive for the experiments with air injection.

Multiple nucleation rates have been previously attributed to variations in the concentration of active sites between replicates, coming from different distributions of impurities or differentiated surface properties in the solids present in the samples.[201,213,214] In this work, variations in the amount of nucleation sites were prevented by using the same tubes for all the experiments as well as preparing samples from the same stock solution. XRPD data also shows that both regimes gave the same crystal form of L-arginine. Thus, crystallization of multiple polymorphs has been discarded to explain the appearance of a second regime.

The multiple regime behavior was accompanied by the observation of crystals at the injection point of some samples 5 - 10 min after quenching (see Figure 5.5).

Figure 5.5 L-arginine crystal blocking the air injection point a few minutes after crash cooling.

This phenomenon was only observed at the start of the experiments and for flow rates above 1200 µl/min. It could be explained as consequence of crystal formation during the pre-heating step. Before crash cooling, saturated air is being injected at 25 °C to the undersaturated solution at 50 °C. When the air flow rate is high enough, local evaporation combined with cooling could lead to the formation of small crystals at the tube tip. These crystals would then grow as the bulk solution becomes supersaturated.

Formation of crystals during the pre-heating step would be able to explain the multiple regime behavior of the distributions. Neither the formation of crystals at the tube tip nor the multiple regime were observed at flow rates below 1500 µl/min, presumably because heat transfer and evaporation rate are not sufficient to maintain a local supersaturation during the pre-heating step. To account for this phenomenon, the average induction times were determined only from the slope of the second regime. Assuming that the source of the first crystal does not significantly affect the rate of turbidity build-up, the average detection delay could be obtained from linear regression of the observed induction times within the first 15 min. Note that the accuracy of these calculations is severely lowered. The impact of temperature variations between sample cells and surface variations in the tubing was previously included in the reference samples. However, when data fitting is separated in two time frames, the samples with the lower temperatures and higher surface irregularities in the tubing are more likely to fall within the first slope, affecting the slope of the second half of the distribution. The experimental results obtained with this method should therefore lead to conclusions only if the observed induction times show a strong deviation from the reference values. The fitted induction times and detection delays are summarized in Table 5.2.

Table 5.2 Fitted mean induction times (τ_{ind}) and detection delays (t_d) for the experiments with air injection, including 95% confidence intervals from linear regression.

	Flow rate (µl/min)	**Weight loss (%)**	**τ_{ind} (min)**	**t_d (min)**	**$r^{2\,a}$**
Glycine	0	0.15 ± 0.08	128 ± 5	69 ± 7	0.976
	195 ± 56	0.16 ± 0.10	149 ± 4	42 ± 4	0.991
	651 ± 89	0.25 ± 0.11	67 ± 2	11 ± 3	0.981
	1237 ± 182	0.51 ± 0.23	36 ± 1	13 ± 2	0.977
L-arginine	0	0.22 ± 0.12	78 ± 3	15 ± 2	0.986
	1110 ± 150	0.34 ± 0.13	72 ± 2	0 ± 2	0.987
	1544 ± 287	0.37 ± 0.17	88 ± 5	3 ± 1	0.974 - 0.973
	2111 ± 397	0.43 ± 0.18	97 ± 11	3 ± 0	0.975 - 0.956

[a] Multiple r^2 values come from linear regression on the first and the second regime, respectively.

A common trend for both compounds is a significant reduction in the detection delay with air injection. Interestingly, the detection delay stops decreasing after a certain flow rate. The minimum detection delay was not observed for the experiments at variable supersaturation (Figure 5.3), where induction times and detection delays always decreased together.

The impact of air injection on solvent evaporation is calculated from the difference between the weight loss at the end of the experiment and that of the reference samples. By pre-saturating the air at the solution temperature, the average weight loss from solvent evaporation is kept below 0.36% in glycine solutions. Note that the weight loss is measured after 5 hours of gassing. However, 75% of the samples with this weight loss crystallized within the first hour. The amount of solvent evaporated at the point of nucleation is thus negligible. Based on the observed weight losses, it is safe to assume that the effect of air injection on glycine solutions goes beyond solvent evaporation.

5.4.3 The impact of mixing on induction times

To achieve a better understanding on the sensitivity of the system to changes in the mixing intensity, induction time measurements were conducted at constant supersaturation with agitation rates of 500 rpm and 700 rpm. Results are summarized in Figure 5.6 and Table 5.3.

Table 5.3 Fitted mean induction times (τ_{ind}) and detection delays (t_d) for different mixing intensities, including 95% confidence intervals from linear regression.

	Mixer speed (rpm)	**τ (min)**	**t_d (min)**	**r^2**
Glycine	300	305 ± 12	51 ± 7	0.987
	500	142 ± 4	43 ± 4	0.991
	700	132 ± 4	38 ± 5	0.986
L-arginine	300	111 ± 4	11 ± 4	0.980
	500	64 ± 4	5 ± 3	0.987
	700	51 ± 1	7 ± 1	0.986

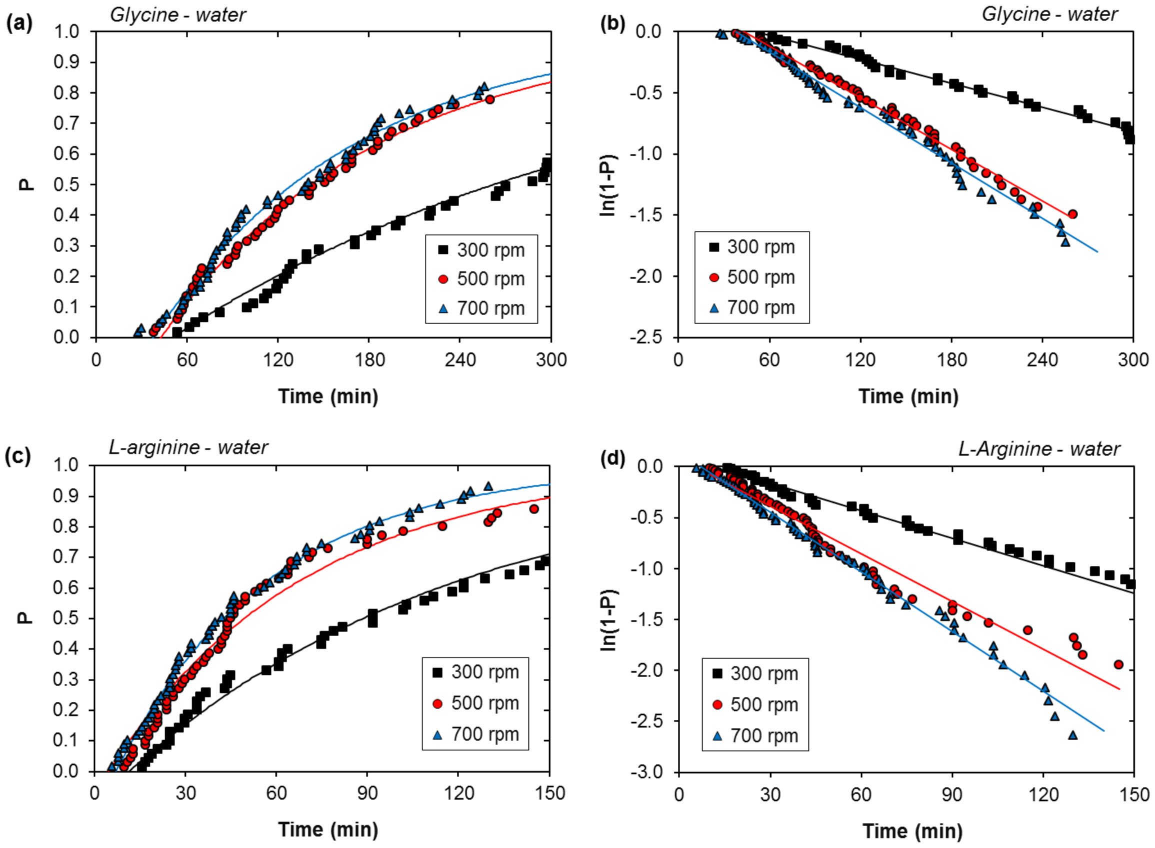

Figure 5.6 Cumulative probability distributions of induction times for aqueous solutions of glycine (a) and L-arginine (b) at constant supersaturation and different mixing intensities. Each point represents the observed induction time of an independent crystallization experiment. (b) and (d) are the logarithmic forms of the probability distributions displayed in (a) and (c), respectively. The solid lines are the theoretical distributions based on the fit to eq 5.3. Sample volume: 1.40 ml. Temperature: 25 °C. Glycine supersaturation: 0.20. L-arginine supersaturation: 0.23.

Mixing can enhance the rate of primary nucleation by promoting contact between solute molecules in solution, thus increasing the probability that a cluster with critical size is formed. However, it does not always have a positive effect. Previous work has shown that certain mixing intensities can lead to destabilization and breakage of the solute clusters.[40,41] Our results show that increasing the impeller speed from 300 rpm to 500 rpm produced a 2-fold decrease in the induction time for both compounds, but the effect of a higher mixing intensity (700 rpm) was barely noticeable. The investigated mixing intensities belong to the transitional mixing regime with impeller Reynolds numbers between 300 and 900. Thus, the observed change in behavior from 500 rpm to 700 rpm is not a consequence of a change in the mixing regime.

5.5 Discussion

5.5.1 Effect of gas injection on primary nucleation

Results with aqueous glycine solutions show a 4-fold reduction in the mean induction time with the injection of saturated air. As supported by the large number of replicates and the measured weight losses, this effect goes beyond sample-to-sample variability and solvent evaporation. Enhancement of the primary nucleation rate was dependent on the air flow rate, and showed no detectable changes at 200 µl/min. The underlying mechanism is presumably related to the perturbation of the supersaturated solution, which would be giving the required energy input for nucleation. This perturbation increases with the air flow rate and it would explain the observed correlation between induction times and injection flow rates. Results for L-arginine indicate that the mechanism goes beyond the increased mixing intensity. Despite both compounds were equally sensitive to increased stirring speeds, L-arginine showed no correlation between the air flow rate and the mean induction time. Were the effect of gas injection explained solely through the additional mixing intensity, both compounds would have shown a similar behavior to the application of air. The effect is thus related to changes in the mixing pattern or local perturbations from bubble collapse.

Alternatively, cluster stabilization at the gas-liquid interphase could have reduced the activation energy for nucleation if the air bubbles were acting as a heterogeneous nucleation site. The total gas-liquid interphase area increases with the flow rate, thus reducing the mean induction time. Since the effect was only observed for one of the two compounds, this mechanism could be sensitive to the system composition.

5.5.2 Mechanism for turbidity build-up

After formation of the first nuclei, the time required for achieving a certain turbidity depends on the combined rates of primary nucleation, secondary nucleation and crystal growth. The contribution of primary nucleation can be studied from the average induction times. Taking the experiments with glycine and an air injection of 650 µl/min as an example, the value of τ indicates that a primary crystal is formed, on average, every 67 minutes. However, the mean detection delay for this experiment is 11 minutes. Considering the much lower value of the detection delay and the fact that building a detectable turbidity requires a large amount of crystals, it is assumed that primary nucleation has a negligible contribution on turbidity after the first crystal is formed. In most of our samples, turbidity is expected to originate from a chain of crystal growth and secondary nucleation events. From the small rates of primary nucleation, this chain could have originated from a single crystal. This single nucleus mechanism was experimentally demonstrated in a similar system by Kadam *et al.*[215]

5.5.3 Effect of gas injection on crystal growth and secondary nucleation

Results from this work demonstrate that air injection is capable of producing a significant drop in the detection delay after the first nucleation event. This behavior was consistent for the two model systems and, in both cases, it is higher than the one observed for increased mixing intensities. In contrast with a faster impeller speed, the effect of gas flow in secondary nucleation could be explained by a change in the mixing direction. The stirring bar provides radial mixing in the sample. With higher agitation speeds, the formed crystals are expected to follow the liquid stream and collide mostly with the impeller and the vial walls. For the experiments with air injection, the upward air flow introduces axial mixing and thus perturbations in the mixing pattern. These perturbations become more important at higher gas flow rates, as they would increase the collision frequency between crystals and promote secondary nucleation. Higher liquid velocities are also expected after bubble collapse, which would promote collisions between nearby crystals.

In addition, were the growth rate in the system limited by diffusion, the improved mass transfer would have a positive effect on crystal growth. Bigger crystals not only contribute to a higher turbidity, but they are also more prone to sedimentation, thus increasing the contact frequency with the impeller and the rate of secondary nucleation.

The observed detection delays stop decreasing after a certain flow rate. This minimum detection delay was not observed for the experiments at variable supersaturation, where a reduction in the mean induction time was always paired with a drop in detection delay. The observed minimum on the detection delay is a consequence of a rate limiting factor. This factor is presumably crystal growth limited by surface incorporation, which would not be affected by the flowing gas in the system. The high detection delays observed for the glycine samples would be supported by the typically slow growth kinetics of this compound, especially at low supersaturations.[216] Alternatively, the effect of gas injection on secondary nucleation could be highly sensitive to the suspension density in the system. When the crystals are originated from a single primary nucleation event, the effect of air flow on crystal collision will be negligible until a sufficient amount of crystals is present in the samples.

5.6 Conclusions

As an approach for a better understanding of the effect of a flowing gas on nucleation and growth kinetics, we have evaluated the effect of continuously injecting saturated air on the observed induction times for two model compounds. Results were analyzed on the basis of probability distributions with independent determination of the mean induction time and detection delay. We have shown that gas injection can have a positive effect on primary nucleation that is dependent on the gas flow rate. Comparing the effects of gas injection with the compound sensitivities to increased agitation rates, it is presumed that the effect goes beyond higher agitation intensities in the sample. Perturbations from the bubble flow and collapse or the presence of the gas-liquid interphase would have had an effect on the primary nucleation rate.

The detection delay dropped with air injection for the two model compounds, indicating that this technique has an effect on the rates of secondary nucleation or diffusion limited crystal growth. A minimum detection delay is observed for both compounds, indicating the presence of a rate limiting factor in turbidity build-up. This factor is presumably crystal growth limited by surface incorporation.

6 Continuous MSMPR crystallization with gas dispersion

This chapter has been written in a manuscript format. A modified version will be submitted to the peer-reviewed journal *Organic Process Research and Development*. The authors to be included in the contribution are *Gerard Capellades, Alessandro Duso, Kim Dam-Johansen, Michael J. Mealy, Troels V. Christensen* and *Søren Kiil*.

6.1 Abstract

Dispersion of a saturated gas in a supersaturated solution has been previously reported to promote nucleation rates during batch crystallization, leading to the exploration of this technique as a cost-effective method to control crystal size distributions. Despite the mechanisms are still unknown, it has been hypothesized that the presence of a flowing gas could promote variations in the flow pattern inside the crystallizer, leading to improved mass transfer and higher rates of secondary nucleation through an increased number of crystal collisions. In this work, we have constructed a lab-scale MSMPR crystallizer with self-induced gas dispersion to investigate the applicability of this technique in continuous crystallization. The effect of different gas hold-ups has been evaluated at high supersaturations and for two different suspension densities. Results show a very limited variation in the overall mass deposition rate, and reductions in the crystal size not exceeding 5 μm for the highest investigated gas hold-up (12%). Studying the effect of impeller speed under the same conditions, we found that an increased mixing intensity has a similar impact as gas dispersion, with a crystal size reduction of 4 μm when the impeller speed was increased from 800 to 950 rpm. These results suggest that the gas dispersion technique is limited to systems where crystallization kinetics can be significantly affected by mixing, and demonstrate a limited applicability for crystal size distribution control in continuous MSMPR crystallizers.

6.2 Introduction

Understanding crystallization kinetics, particularly the nucleation rate, gives a significant advantage for the control of product properties like crystal structure or crystal size distribution. These properties are especially important for pharmaceutical processes where APIs are subject to strict quality requirements. To achieve an adequate bioavailability, and because a large fraction of new APIs have poor water solubility, the design of pharmaceutical crystallization processes is often tailored to the production of very small crystals with a narrow crystal size distribution.[181] Generation of small crystals is particularly challenging as they usually require the use of high supersaturations that lead to a poor control of the nucleation process and fouling in the industrial equipment.

Different techniques have been integrated in pharmaceutical crystallization with the aim of reducing crystal size, the most common being milling and the application of power ultrasound to promote nucleation rates.[99,147,148,154,155,158,161] However, these techniques do not come without limitations. The use of mechanical stress for size reduction of API crystals frequently leads to significantly higher separation costs and variations in crystal shape. Furthermore, these energy intensive methods are hardly applicable with heat sensitive compounds, flammable solvents, and for those systems where a side reaction can be triggered, and their use implies an additional concern for heat dissipation.[148,149] Sonocrystallization has an additional scalability problem since the ultrasonication power decreases heavily with the distance from the ultrasound source.[164,165] Alternative methods to produce small crystals in flow crystallization involve the generation of a local high supersaturation by means of anti-solvent addition or by combination of a hot saturated stream with a colder stream.[106,145,217] These additions are usually conducted in an impinging jet or static mixer that acts as a seed generator at the beginning of the crystallization process.

Previous work studied the impact of gas dispersion on batch crystallization, reporting a significant reduction in the crystallization induction times and applicability for crystal size distribution control for different compounds and scales.[166,168–170,172] Wohlgemuth *et al*. studied the impact of gassing and power ultrasound on induction times and crystal size distributions in adipic acid crystallization, for which both techniques showed a similar crystallization behavior.[167] Since then, the work on gassing crystallization has increased significantly.

In Chapter 5, induction time statistics were applied to separate the rate of primary nucleation from the time required for the system to achieve a certain turbidity.[42] It was found that the shorter induction times could be a consequence of a faster rate of crystallization after the first nucleation event, when the impact of primary nucleation becomes significantly smaller. The presence of a flowing and collapsing gas offered a new perturbation and a significant mixing improvement in batch crystallizers with a transitional mixing regime (Re ≈

300). In this work, we evaluated if this technique could be applicable in a well-mixed continuous crystallizer with impeller Reynolds numbers at the order of 12,000.

From an industrial perspective, the deliberate dispersion of gas in a crystallizer appears counterintuitive. Especially when the entrained gas is in the form of very small bubbles, mechanisms like flotation or gas inclusion in the crystalline phase can significantly impact the product quality and the complexity of the crystallization process.[218] However, it is important not to disregard the effect of fluid dynamics on crystallization, particularly on secondary nucleation and crystal growth. In contrast with a faster impeller speed, gas dispersion promotes mass transfer without inducing crystal breakage or vortex formation. In systems where the crystal growth rate is limited by mass transfer, gas dispersion becomes a simple alternative to enhance crystallization kinetics that is gentle with the crystalline phase and does not necessarily require an additional separation step. Furthermore, a chaotic mixing environment caused by the presence of a flowing gas could promote crystal-to-crystal collisions and secondary nucleation. In contrast to other methods for generating small crystals, the nucleation rate enhancement could be done at constant supersaturations and it would be easily scalable. The gas can be captured from the crystallizer headspace by means of a hollow shaft mixer, and thus the method does not have the high operation costs of ultrasonication or milling.

Continuous MSMPR crystallizers are subject to strict mixing requirements for the achievement of a perfectly mixed suspension and negligible classification in the product removal. In turn, operating with a well-mixed homogeneous system allows for the direct application of *in situ* characterization techniques to monitor the product quality.[110,108] Their simplicity and ability for handling concentrated suspensions makes MSMPR crystallizers the preferred choice for continuous pharmaceutical crystallization. However, this type of crystallizer operates at constant conditions that are constrained by several process and system requirements. Consequently, MSMPR crystallizers are more limited for crystal size distribution control compared to batch or plug flow crystallizers. To significantly expand the attainable region of crystal sizes, one must vary the crystallization method or rely on the use of several crystallization stages.[80]

This study had two main objectives: (1) to assess if gas dispersion is a valid alternative for crystal size distribution control in continuous MSMPR crystallizers, and (2) to further develop the understanding of the effect of a moving gas phase on crystallization kinetics. To this end, a first set of experiments was designed so that the effect of gas hold-up on crystallization yield and crystal size distribution could be assessed at a constant impeller speed. Results from these experiments were later compared to the effect of varying the impeller speed to investigate if there is a relationship between the effect of gas dispersion and that of a higher mixing intensity.

6.3 Experimental section

6.3.1 Materials

Melitracen hydrochloride (≥99.8% purity) was obtained in powder form from H. Lundbeck A/S. Absolute ethanol (≥99.8% purity) purchased from VWR Chemicals was used as a solvent for the process. The solubility data for this solute-solvent system is reported in Section 4.4.1. House nitrogen supplies were used to provide the gas phase.

6.3.2 Continuous crystallization setup

The experimental work was conducted using a coupled dissolver-crystallizer configuration as depicted in Figure 6.1. The dissolver and the MSMPR crystallizer were jacketed reactors with operating volumes of 1000 and 900 mL (excluding gas phase), respectively.

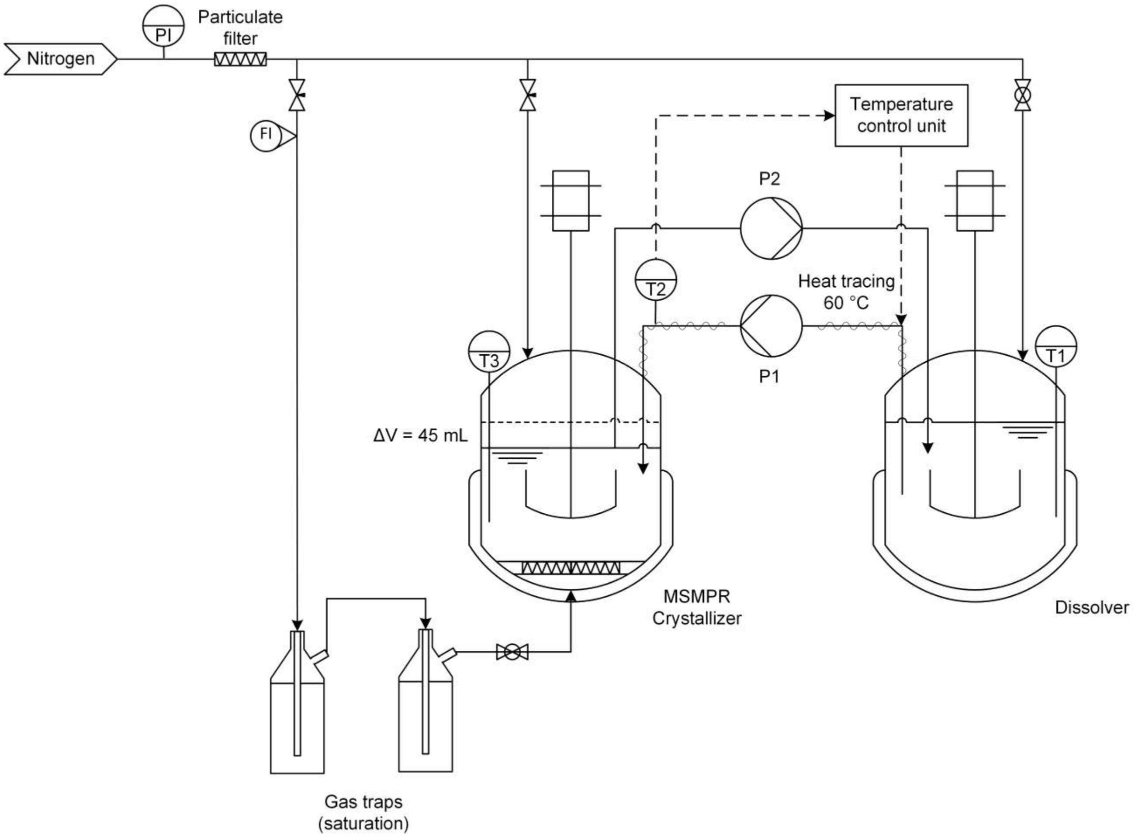

Figure 6.1 Schematic diagram of the setup for continuous MSMPR crystallization with gas dispersion.

An undersaturated feed was kept at 60 °C in the dissolver during operation. P1 was a peristaltic pump (LongerPump BT100-1F) that continuously delivered the feed to the MSMPR crystallizer. The feed stream was heat traced to 60 °C using a temperature control unit (Lund

& Sørensen) to prevent crystallization in the tubing. Product removal was achieved using a programmable peristaltic pump (P2, LongerPump WT600-1F). An intermittent withdrawal approach was used to minimize classification in the product removal stream, by which 5% of the crystallization magma is removed every 5% of a residence time.[78] This was achieved by means of a dip pipe that defines the operating volume of the crystallizer. For each withdrawal step, P2 was programmed to work at full speed (1850 mL/min) and remove a total volume of 150 mL. From this volume, only 45 mL correspond to the crystallization magma above the dip pipe. The excess pumping was conducted so that the product removal stream remains free of suspension between consecutive withdrawals.

The MSMPR crystallizer was connected to an external supply of nitrogen saturated with ethanol. The nitrogen source was first passed through a 0.5 μm particulate filter to prevent the introduction of solid impurities to the MSMPR crystallizer. Then, the gas could be separated in up to three streams, leading to the bottom of the crystallizer and the headspace of each vessel. The latter were present to provide an inert environment before the experiments, but they were not active during operation as they would prevent the saturation of the crystallizer headspace. To minimize solvent evaporation during gas injection, the nitrogen feed connecting to the bottom of the MSMPR crystallizer was passed through two gas traps in series, containing 250 and 100 mL of absolute ethanol at room temperature. During the experiments, the total pressure drop in the nitrogen line was kept below 0.8 bar to prevent significant cooling from Joule-Thomson expansion. The gas saturation and its effect on the crystallizer concentration have been studied experimentally and the results are reported in Appendix D.

6.3.3 Crystallizer design and three phase mixing

A 1000 mL jacketed filter reactor (Ace Glass Incorporated) was used as the MSMPR crystallizer. The vessel had a diameter of 100 mm and was equipped with four 8 mm baffles located 2 mm away from the crystallizer wall. The equipment was designed to operate in three different modes: (1) without gas dispersion, (2) with self-induced gas entrainment by means of a hollow shaft mixer, and (3) with self-induced entrainment and a bottom gas feed that is passed through a 500 μm stainless steel mesh. To isolate the effect of gas hold-up from variations in mechanical mixing, the three modes of operation shared the same impeller system and agitation speed. The baffles and impellers were designed and constructed in house using stainless steel AISI 316. The different components are shown in Figure 6.2.

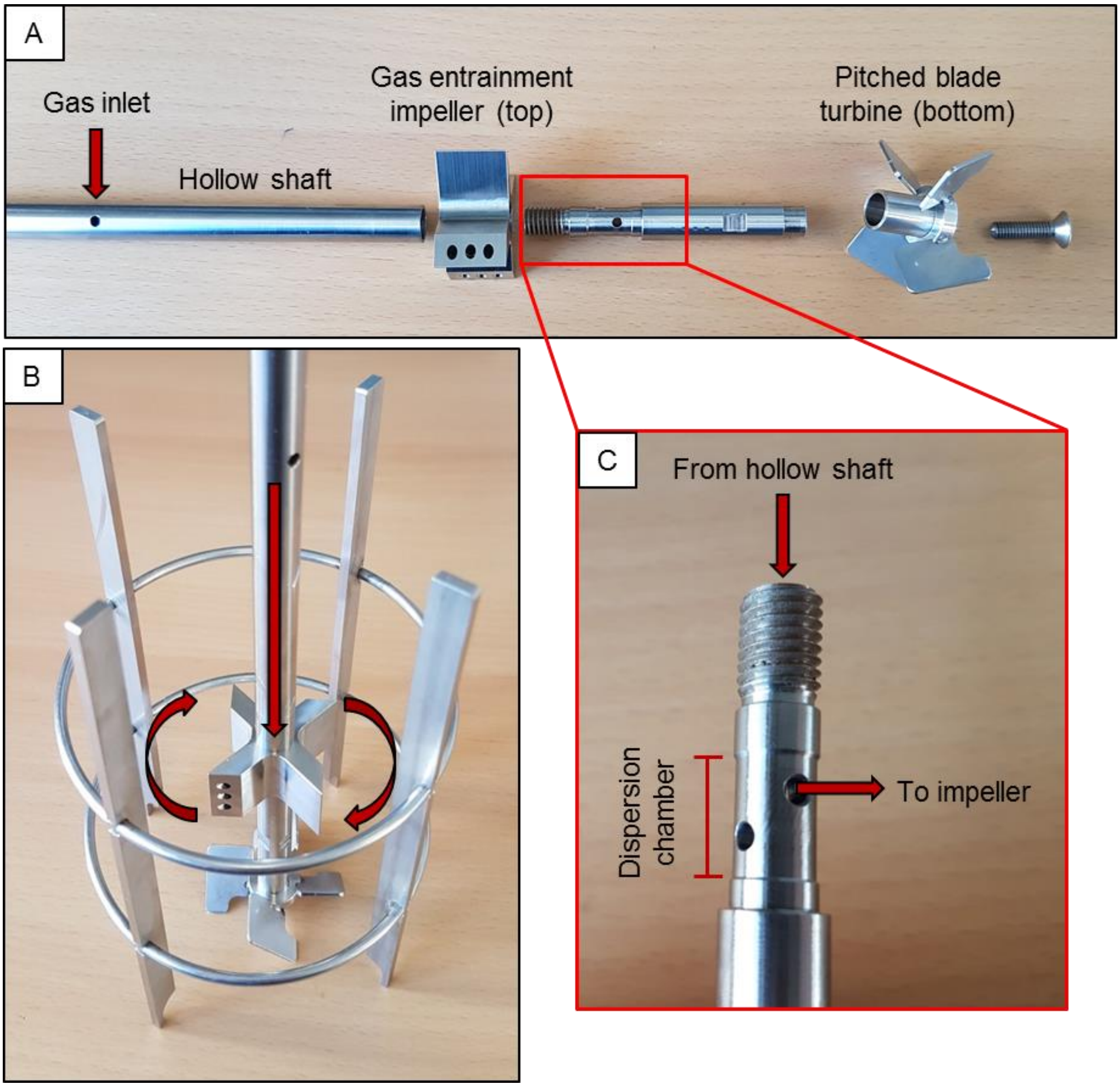

Figure 6.2 Designed impellers for the three phase MSMPR crystallizer. (a) Setup components. (b) Mounted mixer and baffles. The arrows indicate the gas flow and impeller rotation. (c) Close-up of the connection between the hollow shaft and the gas entrainment impeller. When the pieces are connected (b), the gas entrainment impeller is located around the dispersion chamber.

The impeller setup was divided in four components to facilitate dismantling and cleaning in case crystallization occurs in the hollow shaft, and to allow for the testing of different impeller combinations. To connect the different components, the shaft pieces can be screwed together trapping the impellers in the narrow shaft regions.

Induced gas dispersion was achieved through a hollow 40 mm four blade radial flow impeller. The design of the impeller was inspired by the commercially available impellers from Parr Instrument. By creating a hollow path between the crystallizer headspace and the back of the impeller blades, the pressure drop generated at the back of the blades during agitation acts as the driving force to capture the gas from the crystallizer headspace and disperse it into the liquid phase.[219] In this type of gas dispersion, the internal gas circulation is subject to a minimum rotation speed and the circulation rate is a function of the agitation intensity.[220,221] The minimum impeller speed for self-induced gas entrainment in this work was 650 rpm, corresponding to an approximated impeller Reynolds number of 10,000 in absolute ethanol. However, an agitation speed of 800 rpm was selected for the experiments ($Re \approx 12{,}000$) as it provides the maximum gas hold-up with negligible vortex formation. In the experiments without gas dispersion, the hollow shaft was slid inside silicon tubing so that the gas inlet was tightly sealed.

The second impeller was a solid pitched blade turbine (40 mm, 4 blades, 60°), located at the bottom end of the shaft. Its main functions are to prevent solids classification at the bottom of the vessel and to assist in the dispersion of the bottom gas feed. Furthermore, the downward pumping facilitates the dispersion of gas to the bottom of the crystallizer, allowing for homogenous gas dispersion even when the gas is captured by the first impeller.

6.3.4 Methodology for the continuous crystallization experiments

The experiments in this work were conducted in the setup described in Figure 6.1. In all the investigated conditions, the crystallization temperature was kept at 10 °C and the crystallization volume at 900 mL excluding the gas phase. Since varying the impeller speed or the gas hold-up leads to a different suspension height for the same operating volume, the position of the dip pipe for product removal was adjusted at the beginning of each experiment. This ensured that the residence time in the crystallizer remained constant between experiments.

The experiments started from a saturated suspension containing the same concentration in both vessels. After the feed was dissolved at 60 °C and the crystallizer reached a temperature of 10 °C, the pumps were started at full speed for 5-10 seconds so that the inner part of the feed tubing was preheated. Then, the feed flow rate was calibrated with a 25 mL graduated cylinder. Evolution to steady state was tracked using an FBRM G400 probe (Mettler Toledo) that monitors variations in the crystal size distribution. Since the presence of the gas phase and the different mixing intensities can influence the FBRM measurement, the chord length distribution was measured off-line with a 45 mL magma sample in a magnetically agitated beaker. The beaker, sample size, agitation intensity and probe position were maintained constant during the experiments to obtain comparable chord length distributions. At the working temperature and supersaturation, the mother liquor concentration was close to the saturation point at room temperature (C_{sat}(20 °C)= 34.7 g/L) and thus the FBRM readings were stable for few minutes during the off-line reading. The off-line magma sample was returned to the dissolver after the measurement.

At steady state, 4 mL HPLC samples were removed from the feed and the crystallizer mother liquor and filtered through a 0.45 μm syringe filter. Furthermore, a magma sample was analyzed with optical microscopy to detect variations in crystal shape. The sampling method was described in detail in Section 4.3.6. All the steady state samples were taken four times at consecutive residence times and the results were averaged for the data analysis.

At the end of the experiment, the consistency of the feed flow rate was verified with a 25 mL graduated cylinder and the steady state classification was quantified by removing a 4 mL HPLC sample from three different positions in the crystallizer (top, between the two impellers, and below the second impeller). The acceptance criterion for variations in the feed flow rate was a deviation equal or lower than 0.5 mL/min (2.5 and 3.3 % variation for residence times of 60 and 45 min, respectively). Results from the classification check are provided in Appendix D.

The HPLC samples were analyzed using a Hitachi LaChrom Elite system equipped with a Phenomenex Gemini® 10 cm x 4.6 mm x 3 μm C18 110 Å silica column and a L-2455 diode array detector (Hitachi), with detection at 230 nm (see Appendix A for the methods).

6.4 Results and discussion

6.4.1 Consistency of the steady state and sampling accuracy

One of the main complications in the experimental work was to attain an identical feed concentration between experiments, as the extensive off-line sampling led to small variations in the dissolver concentration after several hours of operation. Such variations could lead to misleading conclusions, and thus their impact on the steady state conditions was quantified first. Three experiments were conducted at the same target conditions, during which the feed concentration varied from 97 to 100 g/L. The steady state conditions are reported in Table 6.1.

The steady state was reproducible with a standard deviation amongst the mother liquor concentrations of 0.3 g/L (0.7% of the mean value). The standard deviation amongst the three suspension densities is 1.6 g/L (2.4% of the mean value), and 0.7% (1.1% of the mean value) for the crystallization step yield. These uncertainties include not only the sampling and experimental error, but also the error propagation from the calculations. Variations in the steady state caused by the dispersion of gas will be evaluated considering that these are the minimum uncertainties in the experimental determination of the steady state conditions.

Table 6.1 Steady state conditions for the three repetitions of experiment A1. The experiments were conducted at 10 °C with a residence time of 45 min. The measured values include the mean ± standard deviation of the four replicate samples of the same experiment at steady state, accounting for error propagation in the calculations.

Experiment	C_0 (g/L)	s (rpm)	Gas	C_{ml} (g/L)	M_T (g/L)[a]	Yield (%)[b]
A1.1	97.5 ± 1.5	800	No	35.6 ± 0.3	64.4 ± 1.8	63.5 ± 1.9
A1.2	97.2 ± 1.8	800	No	36.1 ± 0.4	64.4 ± 1.7	62.9 ± 2.2
A1.3	100.1 ± 1.8	800	No	35.7 ± 0.2	67.1 ± 0.6	64.3 ± 2.2

[a] The crystallizer's suspension density is calculated as C_0-C_{ml}.

[b] The step yield is calculated as $100(C_0-C_{ml})/C_0$.

Especially when the crystal size distribution analysis is conducted off-line, experimental error during sampling combined with fluctuations in CSD during the experiment was a concern for the reproducibility of the results. Figure 6.3 shows the obtained square weighted chord length distributions for different steady state measurements of the same experiment and for three independent experiments. These distributions were chosen for this study as they are usually compared to a volumetric crystal size distribution during MSMPR analysis.[76,77,83,184,189]

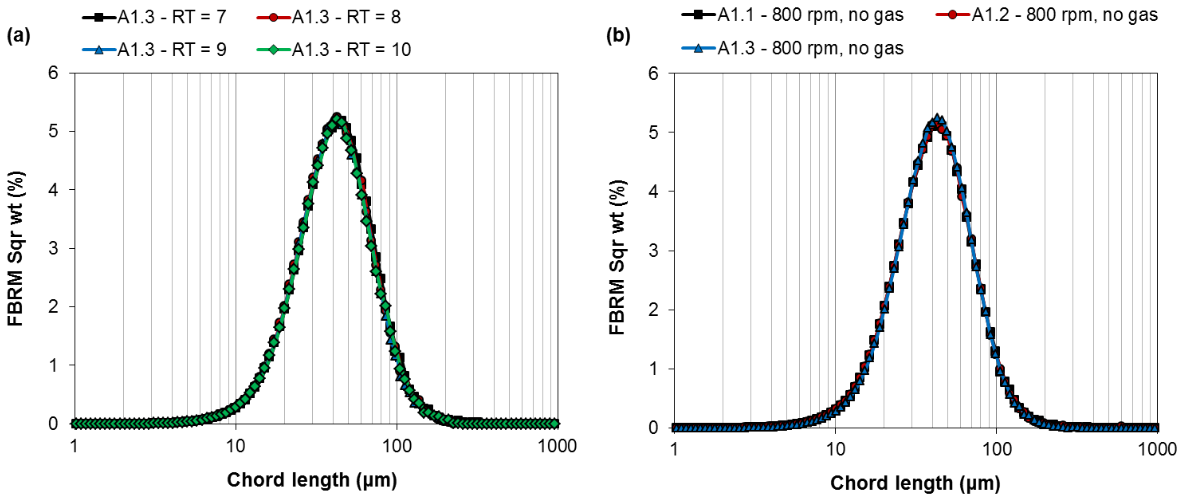

Figure 6.3 (a) Steady state square weighted chord length distribution for different residence times during run A1.3, and (b) comparison between the steady state values on the three repetitions at the same conditions. The latter distributions were obtained from the average over four consecutive residence times at steady state.

Variations in the chord length distribution are negligible in both cases, demonstrating that the sampling method is reproducible and that the steady state is consistent through small deviations in the feed concentration. The square weighted mean chord length presented a standard deviation of 0.3 μm (0.7% of the mean value) between the triplicate experiments.

6.4.2 Extent of gas dispersion

Two different gas hold-ups were investigated in this work. Their values were approximated based on the increase in suspension height upon gassing and the vessel diameter. With an agitation speed of 800 rpm, self-induced gas entrainment provided an approximated gas hold-up of 4% in the crystallizer. The hold-up was increased to 12% with the injection of saturated nitrogen (2.5 L/min) from the bottom of the crystallizer. Compared to other systems with gas entrainment, the obtained hold-up for self-induced entrainment is fairly low, supporting the need for bottom injection to extend the conditions of this study.[222] The homogeneity of gas dispersion was assessed visually using an undersaturated solution containing 15 g/L of Melitracen HCl in ethanol at 10 °C. Figure 6.4 shows a picture of the liquid-gas mixture with 12% hold-up. No apparent difference on bubble size was observed between the two hold-ups.

Figure 6.4 Gas dispersion in the MSMPR crystallizer. The picture was taken on an undersaturated API solution at 10 °C. Agitation speed: 800 rpm. Flow rate (bottom injection): 2.5 L/min.

6.4.3 Continuous crystallization with gas entrainment

The effect of a flowing gas on MSMPR crystallization was evaluated at two different suspension densities (appr. 65 g/L and 15 g/L) adjusted from the feed concentration. The objective was to separate the effects on secondary nucleation from those on primary nucleation and crystal growth. If the flowing gas was able to enhance crystal collisions and secondary nucleation, the extent of this effect would be a function of the suspension density in the crystallizer. To be able to compare the results at both suspension densities, the residence times were adjusted so that a similar steady state supersaturation was obtained in the experiments. The supersaturation value was adjusted experimentally so that it had the highest value that does not result in fouling during the experiment time frame. The steady state supersaturations, calculated as $(C_{ml}-C_{sat}(T))/\ C_{sat}(T)$, were in the range of 0.5 – 0.6 for a feed concentration of 100 g/L and 0.4 – 0.5 for a feed concentration of 50 g/L. Furthermore, the crystallization temperature was maintained at 10 °C to limit the rate of crystal growth and to minimize solvent evaporation. At the studied conditions, the crystal size is already close to the minimum value that can be achieved in the MSMPR crystallizer without fouling. Thus, the industrial applicability of gas dispersion can be directly compared to the best case scenario for generating small crystals in the single stage MSMPR crystallizer. A summary of the experimental conditions is provided in Table 6.2.

Table 6.2 Summary of the experimental conditions for the continuous crystallization experiments with gas dispersion. All the experiments were conducted with an operating volume (excluding gas phase) of 900 mL. The measured feed concentration values include the mean ± standard deviation of the four replicates at steady state.

Experiment	C_0 (g/L)	T (°C)	τ (min)	s (rpm)	Gas hold-up (%)
A1.3	100.1 ± 1.8	10	45	800	0
A2	100.6 ± 1.6	10	45	800	4
A3	101.8 ± 0.6	10	45	800	12
A4	52.5 ± 1.0	10	60	800	0
A5	49.5 ± 1.4	10	60	800	4
A6	50.2 ± 0.6	10	60	800	12

For most of the experimental runs, the dispersion of gas did not produce complications in terms of classification or steady state stability. The system reached steady state within 7-9 residence times regardless of the gas hold-up, and the steady state was successfully maintained for at least four residence times before the experiments were stopped. An exception was experiment A6 which was operated for 13 hours (13 residence times) and it did not reach steady state. Examination of the top of the crystallization vessel at the end of the experiment showed a large fouling ring near the suspension-headspace border. This phenomenon was much less apparent in experiment A5, and practically non-existent in experiment A3. Presumably, foam formation at the top of the vessel provided a region with poor mixing that facilitated the growth of a fouling layer at the top of the vessel. Even though the foam layer occupied a very small height in the crystallization magma (1-2 mm), the use of intermittent withdrawal expanded the area of the vessel wall that is covered by the moving foam layer. The negligible impact in runs A2-3 could be explained by the shorter experiment duration and the higher solids concentration that helps to minimize both foam formation and regions with high supersaturation in the crystallizer. Pictures of the crystallization vessel at the end of runs A3, A5 and A6 are shown in Figure 6.5.

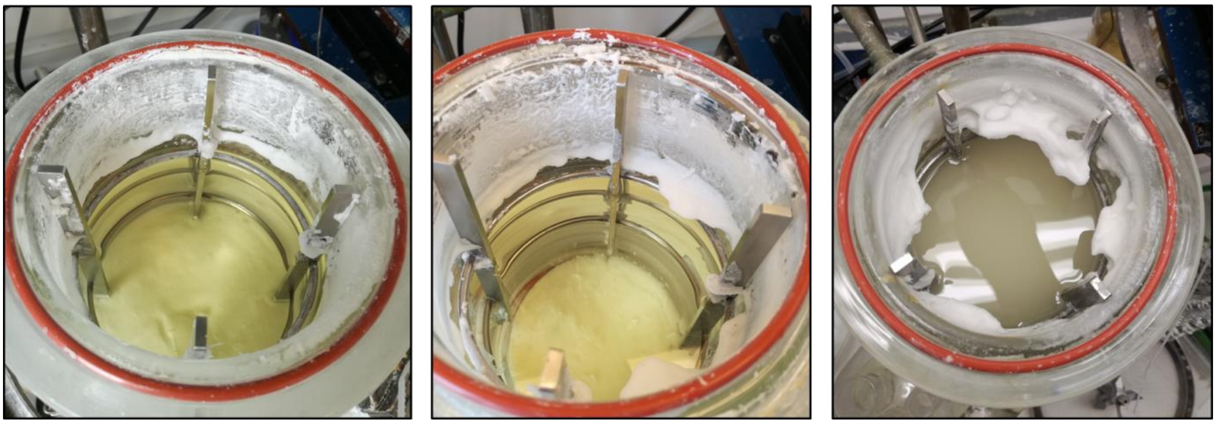

Figure 6.5 Crust formation at the top of the MSMPR crystallizer. Left: end of experiment A3 Middle: end of experiment A5. Right: end of the first attempt at experiment A6. None of the other experiments in this work presented this phenomenon.

Since the extent of crust formation precluded the attainment of steady state in run A6, this experiment was repeated and the encrustation was manually removed every 30 minutes during start-up. The evolution to steady state for the first and second attempt at run A6, tracked with FBRM, is plotted together in Figure 6.6.

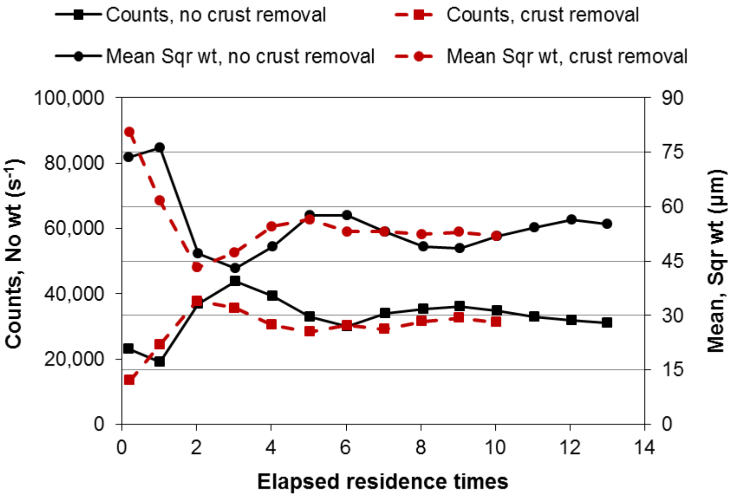

Figure 6.6 Evolution of the FBRM counts and square weighted mean chord length throughout the two attempts at run A6. Encrustation at the top of the crystallizer was periodically removed in the second attempt.

As it can be seen from Figure 6.6, removing the formed crust from the top of the vessel was an effective method to stabilize the MSMPR crystallizer during start-up. However, note that the accuracy of the experimental results is lower, as the user interaction can affect both the observed yield and crystal size distribution, especially when the solute suspension density is already small.

Other than the observed crust formation at low suspension densities, the presence of the flowing gas did not have a significant effect on the steady state classification nor on the representative product removal. This was verified using separate experiments described in Appendix D.

A sample of the microscope pictures taken for the crystallization magma is provided in Figure 6.7. Despite the high operating supersaturations, none of the experiments with gas dispersion presented detectable inclusions of gas bubbles in the crystal lattice. Furthermore, the crystal shape was consistent regardless of the operating conditions, and none of the experiments presented significant crystal breakage.

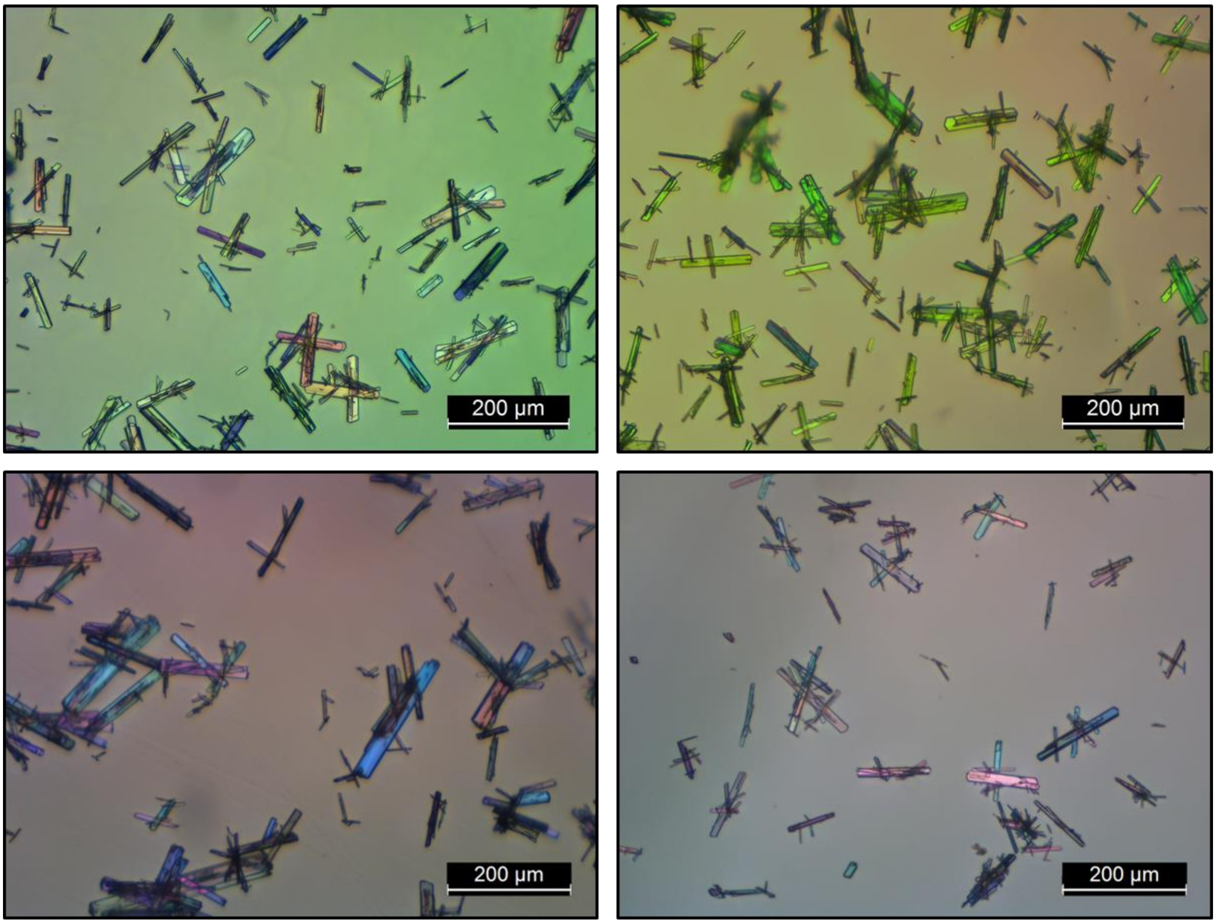

Figure 6.7 Microscope pictures of the crystallization magma from runs A1.3 (top left), A3 (top right), A4 (bottom left) and the second attempt at A6 (bottom right).

For a constant feed concentration, temperature and residence time, studying variations in the steady state mother liquor concentration is the most direct approach to detect variations in the overall rate of crystallization. In this work, this approach has been preferred over the study of crystal populations due to the small variations in yield and size distribution between experiments. Calculating the crystal populations is subject to error propagation from the experimental feed concentration, mother liquor concentration and crystal size distribution. The uncertainties are especially significant when a variation of 2-3 g/L in the feed concentration between experiments can trigger a similar variation in the steady state suspension density. As it is expected due to the significant dependence of the mass deposition rate with supersaturation, and further validated with the results in Table 6.1, the mother liquor concentration is a much more stable parameter than the suspension density through small fluctuations in the feed concentration. The steady state mother liquor concentrations have been plotted together with the saturation concentration in Figure 6.8.

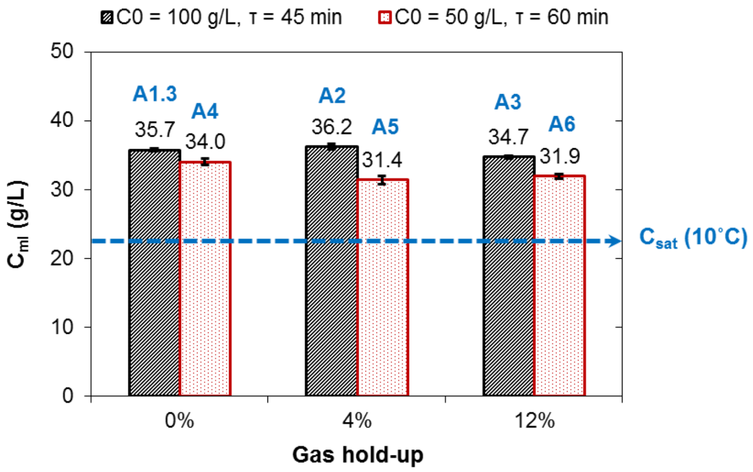

Figure 6.8 Effect of gas hold-up on the steady state mother liquor concentration in the MSMPR crystallizer. The error bars are calculated from the standard deviations between four consecutive samples at steady state.

From the results in Figure 6.8, only the dispersion of gas at low feed concentrations (A5, A6) produced a detectable drop in the steady state mother liquor concentration. This variation would suggest a kinetic enhancement triggered by gas dispersion. However, due to the observed degree of fouling at the top of the vessel, it is complicated to assess if the dispersion of gas had an effect on crystallization yield beyond the experimental reproducibility. Even if the encrustation is limited by manual removal, its formation and growth will contribute to a higher solute mass deposition in the crystallizer.

If gas dispersion had an enhancing effect on primary nucleation or crystal growth, this effect would be consistent regardless of suspension density, especially when all the experiments share the same temperature and a similar supersaturation. Moreover, an effect on secondary nucleation would be more significant for the experiments at high feed concentration due to the significant dependence of this phenomenon with suspension density. Based on the results from experiments A1 to A3, gas dispersion has no observable impact on crystallization for the studied system. Thus, it is likely that the observed reductions for experiments A4 to A6 come from fouling and not from a kinetic enhancement from the gas phase.

The limited effect of gas dispersion is supported by the observed chord length distributions at steady state. As it can be observed from Figure 6.9, a gas hold-up of 4% in experiment A2 gave the same crystal size distribution as operating without gas dispersion (exp. A1.3). A size reduction of 5 μm was observed for a gas hold-up of 12% (A3). Such reduction is significantly higher than the experiment reproducibility reported in Figure 6.3, and it could have been caused by a promotion of secondary nucleation. This experiment also exhibited the lowest mother liquor concentration at the studied feed concentration. Even though the value is marginally, yet statistically higher than the experiment reproducibility, a smaller effect in the mother liquor concentration would be expected due to the slower growth rate at lower supersaturations. The small increase in crystal size and the broadening of the chord length distribution for experiments A4 to A6 is to be expected, as those crystals that fall from the fouling layer will have a longer effective residence time and thus a larger size.

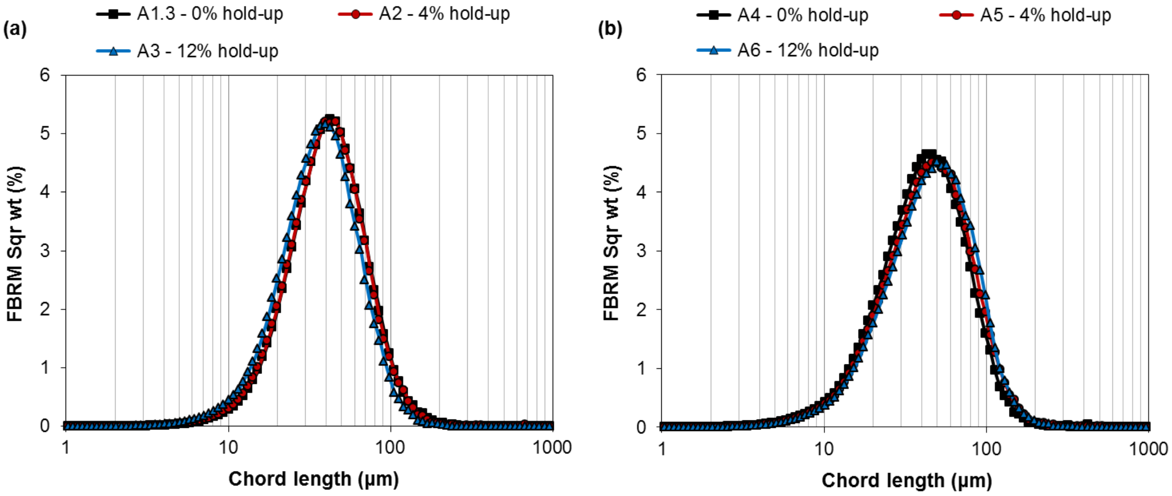

Figure 6.9 Effect of gas hold-up on the steady state chord length distribution in the crystallization magma. (a) Experiments at high suspension densities (A1 to A3). (b) Experiments at low suspension densities (A4 to A6).

Based on the significant amount of work that reports an effect of gas dispersion in batch crystallization, the limited effect of this technique in MSMPR crystallization was surprising. It is important to note that, in contrast to batch crystallizers, a continuous MSMPR crystallizer operating at steady state exhibits a constant supersaturation and suspension density. The steady state is maintained by the internal feedback between crystallization kinetics and the crystal size distribution, and supersaturation plays an important role defining these parameters. When a phenomenon produces a small enhancement in crystallization kinetics, it triggers a reduction in the mother liquor concentration. This produces a drop in supersaturation that limits the net kinetic enhancement. This kind of behavior is common in continuous MSMPR crystallization and it is aggravated when the system operates close to equilibrium. Consequently, a significant change in other process parameters like the residence time or feed concentration often leads to small variations in the steady state mother liquor concentration.[70,74,184] In this work we have operated at high supersaturations that should minimize this issue. However, there is a possibility that the effects of gas dispersion are too small to produce a variation in the steady state far beyond the experimental error in the determination of the steady state conditions.

Alternatively, the limited effect observed in this work could be related to the mixing conditions in the MSMPR crystallizer. It is expected that the upward-flowing gas will generate additional mixing in the magma. Nevertheless, the increased mixing intensity does not necessarily lead to a significant increase in the number of crystal impacts. Prior studies on crystal-impeller impact frequencies reported a direct dependency between the probability of collision and the local Stokes number.[223] Smaller particles tend to follow the fluid streamlines rather than the sedimentation inertia. Thus, especially when the crystal size distribution is narrow, perturbing these fluid streamlines does not necessarily lead to a higher crystal-crystal collision frequency.

Finally, it is possible that despite the high operating supersaturations, the collision energy is not high enough to cause secondary nucleation. The probability of generating secondary nuclei from a crystal collision depends on the contact force applied to the parent crystal.[45,46,48] If the collisions promoted by the gas phase do not have enough intensity, or if secondary nucleation relies on impeller-crystal collisions for this system, it is expected that the gas phase will have a negligible effect compared to a higher impeller speed.

The limited effect of gas dispersion due to the suspension mixing behavior would be supported by the results in Chapter 4, where the kinetic rate equations fitted for a smaller MSMPR crystallizer gave a nucleation rate order for suspension density of 0.56. Even though variations in crystallization kinetics can occur upon crystallizer scale-up, secondary nucleation dominated by crystal-crystal collisions typically leads to a second order dependency for the suspension density.[56]

6.4.4 Continuous crystallization at variable agitation speeds

To further investigate the mechanisms behind the observed behavior, the effect of varying the mixing intensity through different impeller speeds was investigated in the same setup. An impeller speed of 650 rpm (Re ≈ 10,000 in ethanol) was selected at the lower end, as this was the minimum agitation speed that would induce gas entrainment. Even though these experiments were conducted without gas entrainment, lower impeller speeds were not investigated as the objective was to conduct the evaluation in a mixing region that would allow for gas dispersion as an alternative. The maximum investigated impeller speed was 950 rpm (Re ≈ 14,000 in ethanol) above which significant vortex formation started to occur. The experimental conditions are summarized in Table 6.3.

Table 6.3 Summary of the experimental conditions for the continuous crystallization experiments at different agitation intensities. All the experiments were conducted with an operating volume of 900 mL. The measured feed concentration values include the mean ± standard deviation of the four replicates at steady state.

Experiment	C_0 (g/L)	T (°C)	τ (min)	s (rpm)	Gas hold-up (%)
A7	98.2 ± 0.8	10	45	650	0
A8	98.3 ± 1.6	10	45	950	0
A9	50.9 ± 0.4	10	60	650	0
A10	50.4 ± 0.3	10	60	950	0

The steady state mother liquor concentrations are plotted together in Figure 6.10. To facilitate the analysis, the results from experiments A1.3 and A4 (800 rpm and no gas dispersion) are included in the plot.

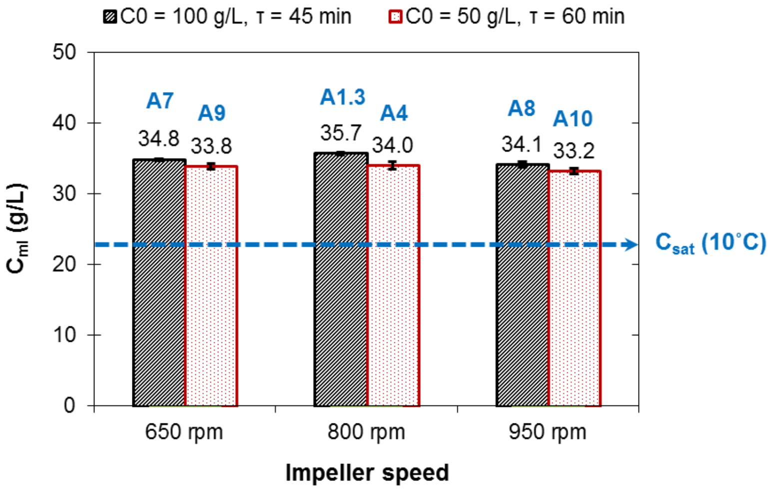

Figure 6.10 Effect of impeller speed on the steady state mother liquor concentration in the MSMPR crystallizer. The error bars are calculated from the standard deviations between four consecutive samples at steady state.

The similarity between the mother liquor concentrations indicates that there is no significant variation in the mass deposition rate caused by a higher impeller speed. These results demonstrate that, at the mixing conditions that would allow for gas dispersion in this system, crystallization kinetics cannot be further promoted by mixing.

The steady state chord length distributions for different mixing intensities are reported in Figure 6.11. As expected from the negligible variations in the mother liquor concentration, the crystal size distribution is not subject to significant changes despite the variations in mixing. A 4 μm reduction in the mean chord length was observed at the higher suspension density when the impeller speed was increased from 800 to 950 rpm. The size reduction would suggest a promotion of the secondary nucleation rate or the presence of crystal breakage. However, no significant variations in the crystal shape distribution were observed upon the analysis of approximately 700 crystals from the optical microscopy pictures of the crystallization magma (reported in Appendix D). An increased effect in crystal breakage was discarded based on this analysis. Note that the distribution obtained at 650 rpm is very similar to the one obtained at 950 rpm. Considering that the chord length distribution is unaltered at the lower suspension densities, it is unlikely that diffusion-limited crystal growth would be a consequence of the increased crystal size between 650 rpm and 800 rpm. From the small extent of the observed variations, it is likely that the observed variations are a consequence of experimental error.

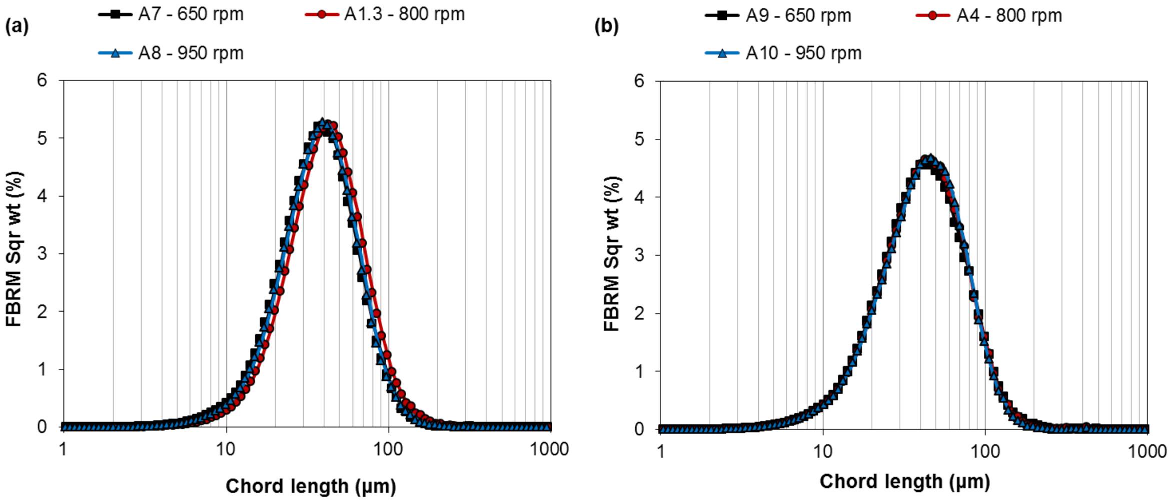

Figure 6.11 Effect of impeller speed on the steady state chord length distribution in the crystallization magma. (a) Experiments at high suspension densities (A1.3, A7, A8). (b) Experiments at low suspension densities (A4, A9, A10).

Increasing the stirrer speed would be expected to promote the secondary nucleation through an increased number of crystal collisions with the impellers, vessel walls, baffles and other crystals.[223,224] Furthermore, were the crystal growth rate limited by diffusion, an increased mixing intensity would lead to a faster rate of crystal growth. Even though these effects, a negligible impact of mixing on crystallization kinetics has been previously reported in stirred tanks.[225,226]

The fact that higher mixing intensities did not lead to a significant reduction in the steady state mother liquor concentration supports that crystallization kinetics are not limited by diffusion, and that the rate of nucleation cannot be further promoted by mixing. Considering the high impeller velocity, it is unlikely that the energy provided by collisions with the impeller is not sufficient to generate secondary nuclei. Thus, the negligible effect of mixing is likely a consequence of a fixed collision frequency between the crystals and other solids in the crystallizer. The already high fluid velocities in the crystallizer, combined with the small crystal sizes, facilitate that the crystals follow the fluid streamlines instead of colliding with the impeller or each other.

From the point of view of continuous pharmaceutical crystallization, results from this work have different implications. First and foremost, despite its applicability to induce nucleation in batch crystallization, gas dispersion is not an efficient tool for reduction of crystal sizes in a well-mixed continuous MSMPR crystallizer. The homogeneous dispersion of a gas phase requires high agitation intensities, and when the aim is to generate small crystals, the other conditions in the MSMPR crystallizer are already adjusted for a small crystal size. Even though these results are for just one system, it is likely that other systems will face the same problem as they would operate with high mixing intensities and small crystal sizes, for which the promotion of crystal collisions is limited by the tendency of the crystals to follow the fluid streamlines. Furthermore, continuous crystallization systems in pharmaceutical production usually deal with significantly smaller suspension densities than batch processes, thus making the promotion of crystal collisions more difficult. Since the observed tendency for foam formation and fouling becomes an additional concern for the implemented process, the effect of gas dispersion should have been significantly higher to compensate for the added complexity.

6.5 Conclusions

This chapter was aimed at the assessment of the industrial applicability of gas dispersion for crystal size distribution control in continuous MSMPR crystallizers. To this end, the effect of a moving gas phase on crystallization yield and crystal size distribution was investigated at high supersaturations and two different suspension densities. The crystallizer was designed to promote the formation of small crystals and to comply with the heavy demands of three phase mixing. Results from this work show that gas dispersion does not have an appreciable effect in the steady state conditions. Further investigation on the effects of mixing intensity revealed that, due to the mixing requirements in the crystallizer and the initially small crystal sizes, crystallization kinetics cannot be further promoted by mixing. In contrast to previous observations in batch crystallization, results in this work show that the effectiveness of the gas dispersion technique depends on the system sensitivity towards changes in the crystallizer fluid dynamics, thus supporting that the mechanism for kinetic enhancement by means of gassing is related to variations in the crystallizer mixing intensity.

7

Concluding remarks

The work described in this thesis is the result of three years of research towards the development of novel MSMPR crystallizer configurations with improved control over the crystal size and shape. This chapter summarizes the main achievements of this thesis, accounting for the project objectives described in Chapter 1. The open challenges and suggestions for future work are described at the end of the chapter.

7.1 Conclusions

This project has been structured to be academically relevant yet at the same time provide a proof-of-concept for continuous crystallization of Melitracen hydrochloride. This thesis starts with a critical review of the current state-of-the-art methods for MSMPR process development and the novel configurations for generating small crystals. Current methods for MSMPR process development rarely account for variations in crystal shape quantitatively. Especially for compounds exhibiting different crystal habits during process development, kinetics determined from a chord length distribution or the projected area are not necessarily reliable for the early assessment of an optimal set of crystallization conditions. In this area, recent advances towards *in situ* quantitative image analysis will soon provide a solution, although their application has been mostly focused on batch production. Furthermore, although the use of MSMPR cascades provides with a significant improvement for crystal size distribution control, generation of small crystals is limited by product and process constraints. As an alternative to the use of milling or ultrasonication, gas dispersion was considered because of its simplicity and the reported effect in reducing the induction times during batch crystallization.

The project continued with an experimental assessment of the optimal crystallization solvent and the limitations of FBRM as a characterization technique for process development in the Melitracen HCl case study. The latter revealed that, as supported by other studies, the solids concentration has a major impact on the measured chord length distributions. Although this technique is still preferred for *in situ* quality assessment, it is hardly adequate for process development when different suspension densities are employed.

The aforementioned limitations of FBRM measurements, combined with the observed variations in crystal shape during the early stages of MSMPR process development, led to a process development method based entirely on quantitative image analysis. In contrast with methods that measure the crystal size distribution from projected area, the simultaneous characterization of crystal size and shape revealed that this compound is sensitive to crystal breakage in process equipment, and that only the largest dimension is significantly affected by this breakage. Studying the effects of crystallization kinetics on crystal habit for conditions where breakage is negligible, it was found that the shape is consistent throughout the studied range of process conditions. Thus, a unidimensional population model was applied based on the crystal dimension that is not sensitive to breakage, from which the absence of size dependent growth and growth rate dispersion was confirmed. Finally, the application of realistic process constraints to a prediction model revealed that (1) the attainable regions for crystal width distribution control in the MSMPR cascade are very small, and (2) that generating crystals of equivalent size to those currently produced in the batch process would require two crystallization stages and supersaturations close to the fouling limit. These results supported the investigation of novel methods to expand the attainable crystal sizes in MSMPR crystallizers towards smaller crystals.

A fundamental study on the effect of air injection on induction times demonstrated that dispersing a saturated gas in a saturated solution has the potential to promote crystallization rates. In contrast with similar studies, it was found that the reduced induction times are not necessarily related to a higher rate of primary nucleation, but they could be caused by a faster crystallization rate after the first nucleus is formed. By separating the frequency of primary nucleation from the detection delay related to the rate of turbidity build-up after formation of the first nucleus, a consistent 5-fold reduction in the detection delay was obtained for two model compounds. Studying the effect of stirring speed revealed that both systems were sensitive to variations in crystallization kinetics caused by mixing. Thus, the observed promotion could be related to either an increase in the secondary nucleation rate or the enhancement of a diffusion-limited crystal growth.

Considering the previously obtained results, gas dispersion was investigated as a potential solution to the generation of small crystals in the Melitracen hydrochloride case. A novel MSMPR crystallizer employing self-induced gas dispersion was designed with the expected configuration for an implemented system. The assessment was conducted at two gas hold-ups for conditions that were already optimized for the generation of small crystals. It was found that, in contrast with the observations in batch crystallizers, gas dispersion was not able to affect crystallization kinetics to a point that this technique would be industrially applicable. The reason is presumably related to the mixing intensities that allow for three-phase dispersion. In contrast with batch crystallizers, MSMPR crystallizers have strong requirements for homogeneous mixing. Especially when the crystals are already small, high mixing intensities do not necessarily lead to an increased collision frequency. It is likely that at those conditions that are already optimized for the generation of small crystals, gas dispersion is no longer efficient. This hypothesis was further supported by an investigation of the effect of mixing on crystallization kinetics, which did not show a significant impact on crystallization kinetics at the same conditions.

7.2 Suggestions for future work

- *Continuous crystallization of Melitracen HCl*. From this work, it is already known that similar crystals to those currently applied in formulation can be obtained with two-stage MSMPR crystallization, following the conditions described in Table 4.5. It would be necessary to evaluate the consistency of these results by connecting the MSMPR cascade to a lab-scale synthesis, where the nature of the impurities would be different. This configuration would also allow for the application of a precipitation approach, by which Melitracen base could be mixed with an HCl solution in the first MSMPR stage. If the product quality was negatively affected by this approach, it would be necessary to pre-heat the feed stream to 60 °C and join the two streams before the first MSMPR crystallizer, thus applying the cooling crystallization approach used in this project.
- *Process imaging for MSMPR characterization*. Results from this thesis demonstrate the significant advantage of quantitative image analysis for MSMPR process development. Although the time for manual image analysis was significantly shorter than that for the MSMPR experiments, manual analysis is tedious and leads to a poor accuracy because of the small sampling numbers. The application of algorithms for automated analysis would be the first step towards a more practical process development approach. Due to the current limitations of *in situ* imaging techniques, it is suggested to still employ the sampling method developed in this thesis, as it is simple and provides with an optimal sample presentation for the analysis. From a quality assessment point of view, FBRM can still be used in the implemented process for feedback control.
- *Fundamental effect of gas dispersion on nucleation rates*. Although this thesis suggests that the effect of gas dispersion is just a consequence of a different mixing pattern in the crystallizer, the effect of the gas-liquid interphase on nucleation could be verified with induction time measurements in a static system. The study could employ slugs of air and supersaturated solution in a tubular system, where the gas-liquid interphase is constant regardless of the slug size. By controlling the slug size, the surface area to volume ratio can thus be controlled and the effect on the primary nucleation rate quantified with induction time statistics.

References

(1) DiMasi, J. A.; Grabowski, H. G.; Hansen, R. W. *Journal of Health Economics* **2016**, *47*, 20–33.

(2) Tamimi, N. A. M.; Ellis, P. *Nephron - Clinical Practice* **2009**, *113*, 125–131.

(3) Plumb, K. *Chemical Engineering Research and Design* **2005**, *83* (6), 730–738.

(4) Munos, B. *Nature Reviews Drug Discovery* **2009**, *8* (12), 959–968.

(5) Federsel, H.-J. *Expert opinion on drug discovery* **2010**, *5* (9), 813–818.

(6) Behr, A.; Brehme, V. A.; Ewers, C. L. J.; Grön, H.; Kimmel, T.; Küppers, S.; Symietz, I. *Engineering in Life Sciences* **2004**, *4* (1), 15–24.

(7) Poechlauer, P.; Broxterman, Q. B.; Yang, B.; Ende, D.; Baird, J.; Bertsch, C.; Hannah, R. E.; Orco, P. D.; Noorman, O. H.; Yee, S.; Reintjens, R.; Wells, A.; Massonneau, V.; Manley, J. *Organic Process Research & Development* **2011**, *15*, 900–911.

(8) Schaber, S. D.; Gerogiorgis, D. I.; Ramachandran, R.; Evans, J. M. B.; Barton, P. I.; Trout, B. L. *Industrial & Engineering Chemistry Research* **2011**, *50* (17), 10083–10092.

(9) US Food and Drug Administration. PAT — A Framework for Innovative Pharmaceutical Development, Manufacturing, and Quality Assurance https://www.fda.gov/downloads/drugs/guidances/ucm070305.pdf.

(10) US Food and Drug Administration. FDA Perspective on Continuous Manufacturing http://www.fda.gov/downloads/aboutfda/centersoffices/officeofmedicalproductsandtobacco/cder/ucm341197.pdf (accessed Oct 3, 2014).

(11) Lee, S. L. In *MIT-CMAC 2nd International Symposium on Continuous Manufacturing of Pharmaceuticals*; 2016.

(12) Lee, S. L.; O'Connor, T. F.; Yang, X.; Cruz, C. N.; Chatterjee, S.; Madurawe, R. D.; Moore, C. M. V; Yu, L. X.; Woodcock, J. *Journal of Pharmaceutical Innovation* **2015**, *10* (3), 191–199.

(13) Yu, L. X. *Pharmaceutical Research* **2008**, *25* (4), 781–791.

(14) Wong, S. Y.; Chen, J.; Forte, L. E.; Myerson, A. S. *Organic Process Research & Development* **2013**, *17* (4), 684–692.

(15) Dallinger, D.; Kappe, C. O. *Current Opinion in Green and Sustainable Chemistry* **2017**, *7*, 6–12.

(16) Pedersen, M. J.; Holm, T. L.; Rahbek, J. P.; Skovby, T.; Mealy, M. J.; Dam-johansen, K.; Kiil, S. *Organic Process Research & Development* **2013**, *17*, 1142–1148.

(17) Anderson, N. G. *Organic Process Research & Development* **2012**, *16* (5), 852–869.

(18) Gutmann, B.; Cantillo, D.; Kappe, C. O. *Angewandte Chemie - International Edition* **2015**, *54*, 6688–6728.

(19) Poechlauer, P.; Manley, J.; Broxterman, R.; Gregertsen, B.; Ridemark, M. *Organic Process Research & Development* **2012**, *16*, 1586–1590.

(20) Hartman, R. L.; McMullen, J. P.; Jensen, K. F. *Angewandte Chemie - International Edition* **2011**, *50* (33), 7502–7519.

(21) Mascia, S.; Heider, P. L.; Zhang, H.; Lakerveld, R.; Benyahia, B.; Barton, P. I.; Braatz, R. D.; Cooney, C. L.; Evans, J. M. B.; Jamison, T. F.; Jensen, K. F.; Myerson, A. S.; Trout, B. L. *Angewandte Chemie - International Edition* **2013**, *52*, 12359–12363.

(22) Adamo, A.; Beingessner, R. L.; Behnam, M.; Chen, J.; Jamison, T. F.; Jensen, K. F.; Monbaliu, J. M.;

Myerson, A. S.; Revalor, E. M.; Snead, D. R.; Stelzer, T. *Science* **2016**, *352* (6281), 61–67.

(23) International Conference on Harmonization (ICH) on technical requirements for registration of pharmaceuticals for human use. ICH guideline Q6A https://www.ich.org/fileadmin/Public_Web_Site/ICH_Products/Guidelines/Quality/Q6A/Step4/Q6Astep4.pdf.

(24) Byrn, S.; Pfeiffer, R.; Ganey, M.; Hoiberg, C.; Poochikian, G. *Pharmaceutical Research* **1995**, *12* (7), 945–954.

(25) Toutain, P.-L.; Bousquet-Mélou, A. *Journal of Veterinary Pharmacology and Therapeutics* **2004**, *27*, 455–466.

(26) Shargel, L.; Wu-Pong, S.; Yu, A. *Applied Biopharmaceutics & Pharmacokinetics*, 6 edition.; McGraw Hill, 2012.

(27) Jambhekar, S. S.; Breen, P. J. *Basic Pharmacokinetics*, Second edi.; Pharmaceutical Press, 2012.

(28) Khadka, P.; Ro, J.; Kim, H.; Kim, I.; Kim, J. T.; Kim, H.; Cho, J. M.; Yun, G.; Lee, J. *Asian Journal of Pharmaceutical Sciences* **2014**, *9*, 304–316.

(29) Ochi, M.; Kimura, K.; Kanda, A.; Kawachi, T.; Matsuda, A.; Yuminoki, K.; Hashimoto, N.; M., O.; K., K.; A., K.; T., K.; A., M.; K., Y. *AAPS PharmSciTech* **2016**, *17* (4), 932–939.

(30) Myerson, A. S. *Handbook of Industrial Crystallization*, Second Edi.; Butterworth-Heinemann, 2002.

(31) Chen, J.; Sarma, B.; Evans, J. M. B.; Myerson, A. S. *Crystal growth & design* **2011**, *11*, 887–895.

(32) Oxtoby, D. W. *J. Phys.: Condens. Matter* **1992**, *4*, 7627–7650.

(33) Erdemir, D.; Lee, A. Y.; Myerson, A. S. *Accounts of chemical research* **2009**, *42* (5), 621–629.

(34) Kashchiev, D.; van Rosmalen, G. M. *Crystal Research and Technology* **2003**, *38* (7–8), 555–574.

(35) Vekilov, P. G. *Crystal growth & design* **2010**, *10* (12), 5007–5019.

(36) Turnbull, D. *The Journal of Chemical Physics* **1950**, *18* (2), 198–203.

(37) Toschev, S.; Milchev, A.; Stoyanov, S. *Journal of Crystal Growth* **1972**, *13/14*, 123–127.

(38) Kashchiev, D. *Nucleation: Basic theory with applications*, 1st ed.; Butterworth-Heinemann, 2000.

(39) Mullin, J. W. *Crystallization*, 4th ed.; Butterworth-Heinemann: Oxford, U.K., 2001.

(40) Mullin, J. W.; Raven, K. D. *Nature* **1962**, *195*, 35–38.

(41) O'Grady, D.; Barrett, M.; Casey, E.; Glennon, B. *Chemical Engineering Research and Design* **2007**, *85* (7), 945–952.

(42) Capellades, G.; Kiil, S.; Dam-Johansen, K.; Mealy, M. J.; Christensen, T. V.; Myerson, A. S. *Crystal Growth & Design* **2017**, *17*, 3287–3294.

(43) Maggioni, G. M.; Mazzotti, M. *Crystal Growth & Design* **2017**, *17*, 3627–3635.

(44) Melia, T. P.; Moffitt, W. P. *Journal of colloid science* **1964**, *19*, 433–447.

(45) Clontz, N. A.; McCabe, W. L. *Chemical Engineering Progress Symposium Series* **1971**, *67*, 110.

(46) Bauer, L. G.; Larson, M. A.; Dallons, V. J. *Chemical Engineering Science* **1974**, *29* (5), 1253–1261.

(47) Randolph, A. D.; Sikdar, S. K. *AIChE Journal* **1974**, *20* (2), 410–412.

(48) Tai, C. Y.; McCabe, W. L.; Rousseau, R. W. *AIChE Journal* **1975**, *21* (2), 351–358.

(49) Powers, H. E. C. *Ind. Chem.* **1963**, *39*, 351.

(50) Friej, S.; Reyhani, M. M.; Parkinson, G. M. *Applied Physics A: Materials Science and Processing* **1998**, *66*, 507–511.

(51) Garside, J.; Larson, M. A. *Journal of Crystal Growth* **1978**, *43*, 694–704.

(52) Denk, E. G.; Botsaris, G. D. *Journal of Crystal Growth* **1972**, *15*, 57–60.

(53) Garside, J.; Rusli, I. T.; Larson, M. A. *AIChE Journal* **1979**, *25* (1), 57–64.

(54) Cui, Y.; Myerson, A. S. *Crystal Growth & Design* **2014**, *14* (10), 5152–5157.

(55) Ness, J. N.; White, E. T. *AIChE Symposium series* **1976**, *72*, 64–73.

(56) Randolph, A. D.; Larson, M. A. *Theory of particulate processes - Analysis and Techniques of Continuous Crystallization*; Academic Press, Inc., 1971.

(57) Beckmann, W. In *Crystallization: Basic Concepts and Industrial Applications*; Beckmann, W., Ed.; Wiley-VCH, 2013; pp 7–33.

(58) Vekilov, P. G. *Crystal growth & design* **2007**, *7* (12), 2796–2810.

(59) Garti, N.; Karpuj, L.; Sarig, S. *Crystal Research and Technology* **1981**, *16* (10), 1111–1115.

(60) Puel, F.; Marchal, P.; Klein, J. *Chemical Engineering Research and Design* **1997**, *75* (2), 193–205.

(61) Kempkes, M.; Vetter, T.; Mazzotti, M. *Chemical Engineering Research and Design* **2010**, *88* (4), 447–454.

(62) Liang, Z.; Zhang, M.; Wu, F.; Chen, J. F.; Xue, C.; Zhao, H. *Computers and Chemical Engineering* **2017**, *99* (2017), 296–303.

(63) Srisanga, S.; Flood, A. E.; Galbraith, S. C.; Rugmai, S.; Soontaranon, S.; Ulrich, J. *Crystal Growth and Design* **2015**, *15* (5), 2330–2336.

(64) Tavare, N. S. *Canadian Journal of Chemical Engineering* **1985**, *63* (June), 436–442.

(65) McCabe, W. L. *Industrial and Engineering Chemistry* **1929**, *21* (1), 30–33.

(66) Li, J.; Lai, T. T. C.; Trout, B. L.; Myerson, A. S. *Crystal Growth and Design* **2017**, *17* (3), 1000–1007.

(67) Wierzbowska, B.; Piotrowski, K.; Koralewska, J.; Hutnik, N.; Matynia, A. *Korean Journal of Chemical Engineering* **2009**, *26* (1), 175–181.

(68) Mydlarz, J.; Jones, A. *The Chemical Engineering Journal* **1993**, *53*, 125–135.

(69) Mydlarz, J.; Jones, A. *The Chemical Engineering Journal* **1994**, *55*, 69–80.

(70) Hou, G.; Power, G.; Barrett, M.; Glennon, B.; Morris, G.; Zhao, Y. *Crystal Growth & Design* **2014**, *14* (4), 1782–1793.

(71) Hansen, B. B.; Kiil, S.; Johnsson, J. E. *AIChE Journal* **2009**, *55* (10), 2746–2753.

(72) Wierzbowska, B.; Piotrowski, K.; Hutnik, N.; Matynia, A. *Indian Journal of Chemical Technology* **2010**, *17*, 296–302.

(73) Morris, G.; Power, G.; Ferguson, S.; Barrett, M.; Hou, G.; Glennon, B. *Organic Process Research and Development* **2015**, *19* (12), 1891–1902.

(74) Power, G.; Hou, G.; Kamaraju, V. K.; Morris, G.; Zhao, Y.; Glennon, B. *Chemical Engineering Science* **2015**, *133*, 125–139.

(75) Zhang, H.; Quon, J.; Alvarez, A. J.; Evans, J.; Myerson, A. S.; Trout, B. *Organic Process Research and Development* **2012**, *16* (5), 915–924.

(76) Ferguson, S.; Ortner, F.; Quon, J.; Peeva, L.; Livingston, A.; Trout, B. L.; Myerson, A. S. *Crystal Growth and Design* **2013**, *14* (2), 617–627.

(77) Quon, J. L.; Zhang, H.; Alvarez, A.; Evans, J.; Myerson, A. S.; Trout, B. L. *Crystal Growth & Design* **2012**, *12* (6), 3036–3044.

(78) Alvarez, A. J.; Singh, A.; Myerson, A. S. *Crystal Growth & Design* **2011**, *11* (10), 4392–4400.

(79) Vetter, T.; Burcham, C. L.; Doherty, M. F. *Computer Aided Chemical Engineering* **2014**, *34*, 465–470.

(80) Vetter, T.; Burcham, C. L.; Doherty, M. F. *Chemical Engineering Science* **2014**, *106*, 167–180.

(81) Yang, Y.; Nagy, Z. K. *Industrial & Engineering Chemistry Research* **2015**, *54* (21), 5673–5682.

(82) Park, K.; Kim, D. Y.; Yang, D. R. *Industrial and Engineering Chemistry Research* **2016**, *55* (26), 7142–7153.

(83) Lai, T.-T. C.; Cornevin, J.; Ferguson, S.; Li, N.; Trout, B. L.; Myerson, A. S. *Crystal Growth & Design* **2015**, *15*, 3374–3382.

(84) Rawlings, J. B.; Miller, S. M.; Witkowski, W. R. *Industrial & Engineering Chemistry Research* **1993**, *32*, 1275–1296.

(85) Simon, L. L.; Pataki, H.; Marosi, G.; Meemken, F.; Hungerbühler, K.; Baiker, A.; Tummala, S.; Glennon, B.; Kuentz, M.; Steele, G.; Kramer, H. J. M.; Rydzak, J. W.; Chen, Z.; Morris, J.; Kjell, F.; Singh, R.; Gani, R.; Gernaey, K. V; Louhi-kultanen, M.; O'Reilly, J.; Sandler, N.; Antikainen, O.; Yliruusi, J.; Frohberg, P.; Ulrich, J.; Braatz, R. D.; Leyssens, T.; von Stosch, M.; Oliveira, R.; Tan, R. B. H.; Wu, H.; Khan, M.; O'Grady, D.; Pandey, A.; Westra, R.; Delle-case, E.; Pape, D.; Angelosante, D.; Maret, Y.; Steiger, O.; Lenner, M.; Abbou-Oucherif, K.; Nagy, Z. K.; Litster, J. D.; Kamaraju, V. K.; Chiu, M.-S. *Organic Process Research & Development* **2015**, *19*, 3–62.

(86) Silva, A. F. T.; Burggraeve, A.; Denon, Q.; Van Der Meeren, P.; Sandler, N.; Van Den Kerkhof, T.; Hellings, M.; Vervaet, C.; Remon, J. P.; Lopes, J. A.; De Beer, T. *European Journal of Pharmaceutics and Biopharmaceutics* **2013**, *85*, 1006–1018.

(87) Mettler Toledo. FBRM method of measurement https://www.mt.com/vn/en/home/library/videos/automated-reactors/Lasentec-FBRM-Method-of-Measurement.html (accessed Sep 1, 2017).

(88) Kail, N.; Briesen, H.; Marquardt, W. *Particle and Particle Systems Characterization* **2007**, *24* (3), 184–192.

(89) Heath, A. R.; Fawell, P. D.; Bahri, P. A.; Swift, J. D. *Particle and Particle Systems Characterization* **2002**, *19* (2), 84–95.

(90) Worlitschek, J.; Mazzotti, M. *Particle and Particle Systems Characterization* **2003**, *20*, 12–17.

(91) Barrett, P.; Glennon, B. *Particle and Particle Systems Characterization* **1999**, *16* (5), 207–211.

(92) Ruf, A.; Worlitschek, J.; Mazzotti, M. *Particle and Particle Systems Characterization* **2000**, *17* (4), 167–179.

(93) Kail, N.; Briesen, H.; Marquardt, W. *Powder Technology* **2008**, *185* (3), 211–222.

(94) Kail, N.; Marquardt, W.; Briesen, H. *Chemical Engineering Science* **2009**, *64* (5), 984–1000.

(95) Li, M.; Wilkinson, D.; Patchigolla, K. *Particle and Particle Systems Characterization* **2006**, *23*, 170–174.

(96) Li, M.; Wilkinson, D. *Chemical Engineering Science* **2005**, *60* (12), 3251–3265.

(97) Li, M.; Wilkinson, D.; Patchigolla, K. *Chemical Engineering Science* **2005**, *60* (18), 4992–5003.

(98) Shekunov, B. Y.; York, P. *Journal of Crystal Growth* **2000**, *211* (1–4), 122–136.

(99) Kim, S.; Wei, C.; Kiang, S. *Organic Process Research and Development* **2003**, *7* (6), 997–1001.

(100) Tung, H.-H. *Organic Process Research & Development* **2013**, *17* (3), 445–454.

(101) Kramer, H. J. M.; Kadam, S. S. In *Industrial Crystallization Process Monitoring and Control*; Chianese, A., Kramer, H. J. M., Eds.; Wiley-VCH, 2012; pp 35–50.

(102) Wang, X. Z.; Roberts, K. J.; Ma, C. *Chemical Engineering Science* **2008**, *63* (5), 1173–1184.

(103) O'Sullivan, B.; Barrett, P.; Hsiao, G.; Carr, A.; Glennon, B. *Organic Process Research and Development* **2003**, *7* (6), 977–982.

(104) O'Sullivan, B.; Glennon, B. *Organic Process Research and Development* **2005**, *9* (6), 884–889.

(105) Schöll, J.; Bonalumi, D.; Vicum, L.; Mazzotti, M.; Müller, M. *Crystal Growth and Design Design* **2006**, *6* (4), 881–891.

(106) Ferguson, S.; Morris, G.; Hao, H.; Barrett, M.; Glennon, B. *Chemical Engineering Science* **2012**, *77*, 105–111.

(107) Luo, Y. H.; Wu, G. G.; Sun, B. W. *Journal of Chemical and Engineering Data* **2013**, *58* (3), 588–597.

(108) Powell, K. a.; Saleemi, A. N.; Rielly, C. D.; Nagy, Z. K. *Chemical Engineering and Processing: Process Intensification* **2015**, *97*, 195–212.

(109) Leyssens, T.; Baudry, C.; Escudero Hernandez, M. L. *Organic Process Research & Development* **2011**, *15* (2), 413–426.

(110) Powell, K. A.; Saleemi, A. N.; Rielly, C. D.; Nagy, Z. K. *Organic Process Research and Development* **2016**, *20* (3), 626–636.

(111) Kutluay, S.; Sahin, Ö.; Ceyhan, A. A.; Izgi, M. S. *Journal of Crystal Growth* **2017**, *467*, 172–180.

(112) Barrett, P.; Glennon, B. *Trans IChemE* **2002**, *80*, 799–805.

(113) Jiang, M.; Zhu, X.; Molaro, M. C.; Rasche, M. L.; Zhang, H.; Chadwick, K.; Raimondo, D. M.; Kim, K. K. K.; Zhou, L.; Zhu, Z.; Wong, M. H.; O'Grady, D.; Hebrault, D.; Tedesco, J.; Braatz, R. D. *Industrial and Engineering Chemistry Research* **2014**, *53* (13), 5325–5336.

(114) Calderon De Anda, J.; Wang, X. Z.; Lai, X.; Roberts, K. J.; Jennings, K. H.; Wilkinson, M. J.; Watson, D.; Roberts, D. *AIChE Journal* **2005**, *51* (5), 1406–1414.

(115) Wang, X. Z.; Calderon De Anda, J.; Roberts, K. J. *Chemical Engineering Research and Design* **2007**, *85* (7), 921–927.

(116) Ma, C. Y.; Wang, X. Z.; Roberts, K. J. *Advanced Powder Technology* **2007**, *18* (6), 707–723.

(117) Zhang, R.; Ma, C. Y.; Liu, J. J.; Wang, X. Z. *Chemical Engineering Science* **2015**, *137*, 9–21.

(118) Huo, Y.; Liu, T.; Liu, H.; Ma, C. Y.; Wang, X. Z. *Chemical Engineering Science* **2016**, *148*, 126–139.

(119) Liu, T.; Huo, Y.; Ma, C. Y.; Wang, X. Z. *Journal of Crystal Growth* **2016**, *469*, 160–167.

(120) Eggers, J.; Kempkes, M.; Mazzotti, M. *Chemical Engineering Science* **2008**, *63* (22), 5513–5521.

(121) Eggers, J.; Kempkes, M.; Cornel, J.; Mazzotti, M.; Koschinski, I.; Verdurand, E. *Chemical Engineering Science* **2009**, *64*, 163–171.

(122) Schorsch, S.; Vetter, T.; Mazzotti, M. *Chemical Engineering Science* **2012**, *77* (2012), 130–142.

(123) Schorsch, S.; Ochsenbein, D. R.; Vetter, T.; Morari, M.; Mazzotti, M. *Chemical Engineering Science* **2014**, *105*, 155–168.

(124) Brown, C. J.; Ni, X.-W. *Crystal Growth & Design* **2011**, *11* (3), 3994–4000.

(125) Brown, C. J.; Ni, X.-W. *Crystal Growth & Design* **2011**, *11* (3), 719–725.

(126) Brown, C. J.; Ni, X.-W. *CrystEngComm* **2012**, *14*, 2944–2949.

(127) Tachtatzis, C.; Sheridan, R.; Michie, C.; Atkinson, R. C.; Cleary, A.; Dziewierz, J.; Andonovic, I.; Briggs, N. E. B.; Florence, A. J.; Sefcik, J. *Chemical Engineering Science* **2015**, *133*, 82–90.

(128) Yu, Z. Q.; Chew, J. W.; Chow, P. S.; Tan, R. B. H. *Chemical Engineering Research and Design* **2007**, *85* (7), 893–905.

(129) Nagy, Z. K.; Braatz, R. D. *Annual review of chemical and biomolecular engineering* **2012**, *3*, 55–75.

(130) Borchert, C.; Temmel, E.; Eisenschmidt, H.; Lorenz, H.; Seidel-morgenstern, A.; Sundmacher, K. *Crystal Growth & Design* **2014**, *14*, 952–971.

(131) Le Borne, S.; Eisenschmidt, H.; Sundmacher, K. *Chemical Engineering Science* **2016**, *139*, 61–74.

(132) Larsen, P. A.; Rawlings, J. B.; Ferrier, N. J. *Chemical Engineering Science* **2007**, *62* (5), 1430–1441.

(133) Argaw, G. A.; Alport, M. J.; Malinga, S. B. *African Sugar Technology Association* **2006**, *80*, 399–411.

(134) Masuda, H.; Iinoya, K. *Journal of Chemical Engineering of Japan* **1971**, *4* (1), 60–66.

(135) Masuda, H.; Gotoh, K. *Advanced Powder Technology* **1999**, *10* (2), 159–173.

(136) Patchigolla, K.; Wilkinson, D. *Industrial and Engineering Chemistry Research* **2008**, *47* (3), 804–812.

(137) Pons, M.-N.; Vivier, H.; Delcour, V.; Authelin, J.-R.; Paillères-Hubert, L. *Powder Technology* **2002**, *128*, 276–286.

(138) Podczeck, F. *Powder Technology* **1997**, *93*, 47–53.

(139) Li, M.; Wilkinson, D.; Patchigolla, K. *Particulate Science and Technology* **2005**, *23* (3), 265–284.

(140) Patchigolla, K.; Wilkinson, D.; Li, M. *Particle & Particle Systems Characterization* **2006**, *23* (2), 138–144.

(141) Monnier, O.; Fevotte, G.; Hoff, C.; Klein, J. P. *Chemical Engineering Science* **1997**, *52* (7), 1125–1139.

(142) Muhrer, G.; Mazzotti, M.; Müller, M. *Journal of Supercritical Fluids* **2003**, *27* (2), 195–203.

(143) Zhao, Y.; Krishna, V.; Hou, G.; Power, G.; Donnellan, P.; Glennon, B. *Chemical Engineering Science* **2015**, *133*, 106–115.

(144) Alvarez, A. J.; Myerson, A. S. *Crystal Growth & Design* **2010**, *10* (5), 2219–2228.

(145) Jiang, M.; Zhu, Z.; Jimenez, E.; Papageorgiou, C. D.; Waetzig, J.; Hardy, A.; Langston, M.; Braatz, R. D. *Crystal Growth and Design* **2014**, *14* (2), 851–860.

(146) Furuta, M.; Mukai, K.; Cork, D.; Mae, K. *Chemical Engineering and Processing: Process Intensification* **2016**, *102*, 210–218.

(147) Eder, R. J. P.; Schrank, S.; Besenhard, M. O.; Roblegg, E.; Gruber-Woelfler, H.; Khinast, J. G. *Crystal Growth and Design* **2012**, *12* (10), 4733–4738.

(148) Rossi, D.; Jamshidi, R.; Saffari, N.; Kuhn, S.; Gavriilidis, A.; Mazzei, L. *Crystal Growth and Design* **2015**, *15* (11), 5519–5529.

(149) Jiang, M.; Papageorgiou, C. D.; Waetzig, J.; Hardy, A.; Langston, M.; Braatz, R. D. *Crystal Growth & Design* **2015**, *15* (5), 2486–2492.

(150) Wong, S. Y.; Cui, Y.; Myerson, A. S. *Crystal Growth & Design* **2013**, *13* (6), 2514–2521.

(151) Cui, Y.; Jaramillo, J. J.; Stelzer, T.; Myerson, A. S. *Organic Process Research & Development* **2014**.

(152) Koswara, A.; Nagy, Z. K. *IFAC-PapersOnLine* **2015**, *48* (8), 193–198.

(153) Brown, C. J.; Adelakun, J. a.; Ni, X. *Chemical Engineering and Processing: Process Intensification* **2015**, *97*, 180–186.

(154) Yang, Y.; Song, L.; Gao, T.; Nagy, Z. K. *Crystal Growth and Design* **2015**, *15* (12), 5879–5885.

(155) Yang, Y.; Song, L.; Zhang, Y.; Nagy, Z. K. *Industrial & Engineering Chemistry Research* **2016**, *55*, 4987–4996.

(156) Acevedo, D.; Kamaraju, V. K.; Glennon, B.; Nagy, Z. K. *Organic Process Research and Development* **2017**, *21* (7), 1069–1079.

(157) Igarashi, K.; Yamanaka, Y.; Azuma, M.; Ooshima, H. *Journal of Chemical Engineering of Japan* **2012**, *45* (1), 28–33.

(158) Narducci, O.; Jones, a. G.; Kougoulos, E. *Crystal Growth & Design* **2011**, *11* (5), 1742–1749.

(159) Narducci, O.; Jones, a. G.; Kougoulos, E. *Chemical Engineering Science* **2011**, *66* (6), 1069–1076.

(160) Wood, R. W.; Loomis, A. L. *Philos. Magaz. Ser.* **1927**, *74* (22), 417–436.

(161) Sander, J. R. G.; Zeiger, B. W.; Suslick, K. S. *Ultrasonics Sonochemistry* **2014**, *21* (6), 1908–1915.

(162) Zhang, Z.; Sun, D.-W.; Zhu, Z.; Cheng, L. *Comprehensive Reviews in Food Science and Food Safety* **2015**, *14* (4), 303–316.

(163) Nalajala, V. S.; Moholkar, V. S. *Ultrasonics Sonochemistry* **2011**, *18*, 345–355.

(164) Technology, C.; Ox, O.; Kingdom, U. *Organic Process Research & Development* **2005**, *9* (6), 923–932.

(165) Luque de Castro, M. D.; Priego-Capote, F. *Ultrasonics Sonochemistry* **2007**, *14* (6), 717–724.

(166) Wohlgemuth, K.; Kordylla, A.; Ruether, F.; Schembecker, G. *Chemical Engineering Science* **2009**, *64* (19), 4155–4163.

(167) Wohlgemuth, K.; Ruether, F.; Schembecker, G. *Chemical Engineering Science* **2010**, *65* (2), 1016–1027.

(168) Kleetz, T.; Pätzold, G.; Schembecker, G.; Wohlgemuth, K. *Crystal Growth and Design* **2017**, *17* (3), 1028–1035.

(169) Kleetz, T.; Braak, F.; Wehenkel, N.; Schembecker, G.; Wohlgemuth, K. *Crystal Growth & Design* **2016**, *16* (3), 1320–1328.

(170) Kleetz, T.; Funke, F.; Sunderhaus, A.; Schembecker, G.; Wohlgemuth, K. *Crystal Growth & Design* **2016**, *16* (12), 6797–6803.

(171) Terdenge, L.; Kossuch, J. A.; Schembecker, G.; Wohlgemuth, K. *Powder Technology* **2017**, *320*, 386–396.

(172) Ceyhan, A.; Baytar, O.; Pehlivan, E. *Acta chimica Slovenica* **2014**, *61* (2), 391–397.

(173) Matsumoto, M.; Wada, Y.; Oonaka, A.; Onoe, K. *Journal of Crystal Growth* **2013**, *373*, 73–77.

(174) Zhang, Y.; Becker, T.; Kösters, M. *Asia-Pacific Psychiatry* **2013**, *5* (4), 231–236.

(175) Du, W.; Yin, Q.; Gong, J.; Bao, Y.; Zhang, X.; Sun, X.; Ding, S.; Xie, C.; Zhang, M.; Hao, H. *Crystal Growth and Design* **2014**, *14* (9), 4519–4525.

(176) Kelly, R. C.; Rodríguez-Hornedo, N. *Organic Process Research and Development* **2009**, *13* (6), 1291–1300.

(177) Hao, H.; Hou, B.; Wang, J. K.; Lin, G. *Journal of Crystal Growth* **2006**, *290* (1), 192–196.

(178) European Medicines Agency. ICH guideline Q3C (R6) on impurities: guideline for residual solvents http://www.ema.europa.eu/docs/en_GB/document_library/Scientific_guideline/2011/03/WC500104258.pdf (accessed Aug 21, 2017).

(179) Rumble, J. R. *CRC Handbook of Chemistry and Physics*, 98th editi.; CRC Press, 2017.

(180) Wong, S. Y.; Tatusko, A. P.; Trout, B. L.; Myerson, A. S. *Crystal Growth & Design* **2012**, *12* (11), 5701–5707.

(181) Ferguson, S.; Morris, G.; Hao, H.; Barrett, M.; Glennon, B. *Chemical Engineering Science* **2013**, *104*, 44–54.

(182) Acevedo, D.; Peña, R.; Yang, Y.; Barton, A.; Firth, P.; Nagy, Z. K. *Chemical Engineering and Processing: Process Intensification* **2016**, *108*, 212–219.

(183) Seidell, A. *Solubilities of inorganic and organic compounds*, Second edi.; D. Van Nostrand Company, 1919.

(184) Lai, T. C.; Ferguson, S.; Palmer, L.; Trout, B. L.; Myerson, A. S. *Organic Process Research and Development* **2014**.

(185) Chianese, A.; Kramer, H. J. M. *Industrial Crystallization Process Monitoring and Control*, First edit.; Wiley-VCH, 2012.

(186) Yu, W.; Erickson, K. *Powder Technology* **2008**, *185*, 24–30.

(187) Li, H.; Kawajiri, Y.; Grover, M. A.; Rousseau, R. W. *Crystal Growth and Design* **2014**, *14* (2), 607–616.

(188) Yang, Y.; Nagy, Z. K. *Chemical Engineering Science* **2015**, *127*, 362–373.

(189) Li, J.; Trout, B. L.; Myerson, A. S. *Organic Process Research and Development* **2016**, *20* (2), 510–516.

(190) Vartak, S.; Myerson, A. S. *Organic Process Research and Development* **2017**, *21* (2), 253–261.

(191) Ma, C. Y.; Wang, X. Z. *AIChE Journal* **2008**, *54* (9), 2321–2334.

(192) Sha, Z. L.; Hatakka, H.; Louhi-Kultanen, M.; Palosaari, S. *Journal of Crystal Growth*. 1996, pp 1105–1110.

(193) Toyokura, K.; Ohki, K. *International Chemical Engineering* **1991**, *31* (3), 493–500.

(194) Garside, J.; Shah, M. B. *Industrial and Engineering Chemistry* **1980**, *19* (2), 509–514.

(195) Vonnegut, B. *Journal of Colloid Science* **1948**, *3* (6), 563–569.

(196) La Mer, V. K.; Pound, G. M. *Journal of the american chemical society* **1952**, *74* (10), 2323–2332.

(197) Turnbull, D. *The Journal of Chemical Physics* **1952**, *20* (3), 411–424.

(198) Tan, L.; Davis, R. M.; Myerson, A. S.; Trout, B. L. *Crystal Growth & Design* **2015**, *15*, 2176–2186.

(199) Diao, Y.; Helgeson, M. E.; Myerson, A. S.; Hatton, T. A.; Doyle, P. S.; Trout, B. L. *Journal of the American Chemical Society* **2011**, *133* (11), 3756–3759.

(200) Curcio, E.; López-Mejías, V.; Di Profio, G.; Fontananova, E.; Drioli, E.; Trout, B. L.; Myerson, A. S. *Crystal Growth and Design* **2014**, *14* (2), 678–686.

(201) Diao, Y.; Whaley, K. E.; Helgeson, M. E.; Woldeyes, M. A.; Doyle, P. S.; Myerson, A. S.; Hatton, T. A.; Trout, B. L. *Journal of the American Chemical Society* **2012**, *134* (1), 673–684.

(202) Ildefonso, M.; Candoni, N.; Veesler, S. *Organic Process Research and Development* **2012**, *16* (4), 556–560.

(203) Ildefonso, M.; Revalor, E.; Punniam, P.; Salmon, J. B.; Candoni, N.; Veesler, S. *Journal of Crystal Growth* **2012**, *342* (1), 9–12.

(204) Laval, P.; Salmon, J.-B.; Joanicot, M. *Journal of Crystal Growth* **2007**, *303* (2), 622–628.

(205) Hem, S. L. *Ultrasonics* **1967**, *5* (4), 202–207.

(206) Kulkarni, S. A.; Kadam, S. S.; Meekes, H.; Stankiewicz, A. I.; Horst, J. H. *Crystal Growth & Design* **2013**, *13*, 2435–2440.

(207) Roebuck, J. R. *Proceedings of the National Academy of Sciences of the United States of America* **1926**, *12* (1), 55–58.

(208) Yang, X.; Wang, X.; Ching, C. B. *Journal of Chemical and Engineering Data* **2008**, *53* (5), 1133–1137.

(209) Hayashi, K.; Matsuda, T.; Takeyama, T.; Hino, T. *Agr. Biol. Chem.* **1966**, *30* (4), 378–384.

(210) Kashchiev, D.; Verdoes, D.; van Rosmalen, G. M. *Journal of Crystal Growth* **1991**, *110* (3), 373–380.

(211) Jiang, S.; Ter Horst, J. H. *Crystal Growth and Design* **2011**, *11* (1), 256–261.

(212) Little, L. J.; Sear, R. P.; Keddie, J. L. *Crystal Growth and Design* **2015**, *15* (11), 5345–5354.

(213) Laval, P.; Crombez, A.; Salmon, J. B. *Langmuir* **2009**, *25* (3), 1836–1841.

(214) Diao, Y.; Myerson, A. S.; Hatton, T. A.; Trout, B. L. *Langmuir* **2011**, *27* (9), 5324–5334.

(215) Kadam, S. S.; Kramer, H. J. M.; Ter Horst, J. H. *Crystal Growth and Design* **2011**, *11* (4), 1271–1277.

(216) Mohan, R.; Myerson, A. S. *Chemical Engineering Science* **2002**, *57* (20), 4277–4285.

(217) Jiang, M.; Li, Y. E. D.; Tung, H. H.; Braatz, R. D. *Chemical Engineering and Processing: Process Intensification* **2015**, *97*, 242–247.

(218) Soare, A.; Lakerveld, R.; Van Royen, J.; Zocchi, G.; Stankiewicz, A. I.; Kramer, H. J. M. *Industrial and Engineering Chemistry Research* **2012**, *51* (33), 10895–10909.

(219) Martin, G. Q. *Ind. Eng. Chem. Process Des. Develop.* **1972**, *11* (3), 397–404.

(220) Joshi, J. B.; Sharma, M. M. *The Canadian Journal of Chemical Engineering* **1977**, *55*, 683–695.

(221) Sawant, S. B.; Joshi, J. B. *The Chemical Engineering Journal* **1979**, *18*, 87–91.

(222) Murthy, B. N.; Kasundra, R. B.; Joshi, J. B. *Chemical Engineering Journal* **2008**, *141* (1–3), 332–345.

(223) Kee, K. C.; Rielly, C. D. *Chemical Engineering Research and Design* **2004**, *82* (A9), 1237–1249.

(224) Melia, T. P.; Moffitt, W. P. *Industrial and Engineering Chemistry Fundamentals* **1964**, *3* (4), 313–317.

(225) Ting, H. H.; McCabe, W. L. *Industrial and Engineering Chemistry* **1934**, *26* (11), 1201–1207.

(226) Sikdar, S. K.; Randolph, A. D. *AIChE Journal* **1976**, *22* (1), 110–117.

Appendix A – Methods for HPLC analysis

This section provides with a short instruction manual on how to determine the concentration of Melitracen HCl through HPLC analysis. Note that the HPLC method has been designed for the rapid determination of Melitracen concentrations from purified Melitracen HCl – ethanol solutions. The presence of additional impurities would require a more complex approach.

A.1 Equipment

Pump: Hitachi L-2130.
Autosampler: Hitachi L-2200.
Column oven: Hitachi L-2300.
Column: Gemini 3 µm C18 110 Å, 100 x 4.6 mm ID (Phenomenex).
Detector: Hitachi Diode Array Detector (DAD) L-2455.

A.2 Preparation of the mobile phase

Amounts for buffer preparation (50 mM ammonium formate), in a 1 liter bottle:

1. Ammonium formate – 3.15 g.
2. Water (Demineralized, miliq) – 1000 ml.
3. Adjust to pH = 9.0 with an aqueous ammonium hydroxide solution.

Mobile phase: 10% buffer, 90% Acetonitrile.

1. To prepare 1.8 liters of mobile phase, pour 1620 ml of acetonitrile and 180 ml of buffer in a blue cap flask. Shake vigorously.
2. Place the flask in the ultrasound bath for 30 min and under a fume extractor. Leave the cap open. This step is conducted to degas the mobile phase.
3. Without further mixing the mobile phase, connect it to the HPLC (line B) through the provided in-line filter.

A.3 Sample preparation

1. Heat the sample in a thermomixer (see temperatures in Table A.1) and leave it agitated (800 rpm) until full dissolution.
2. While the samples are being heated up, pipette the corresponding ethanol volumes to the dilution vials and cap them. Always use a 200 µl pipette for the samples and the 1000 µl pipette for the ethanol.
3. Remove the sample from the thermomixer and conduct the two dilutions using the amounts specified in Table A.1.

Table A.1 Dilution procedures for the most common sample concentrations in this work.

Expected concentration (g/L)	Dissolution temperature (°C)[a]	Dilution 1 (µL)		Dilution 2 (µL)		Dilution factor
		Sample	Ethanol	Sample	Ethanol	
20 – 40	40	200	800	200	800	1/25
40 – 70	50	200	800	100	900	1/50
70 – 130	60	100	900	100	900	1/100

[a] The dissolution temperature is kept approximately 10 °C above the API solubility, as determined in this work.

4. Prepare the HPLC samples by pipetting 100 µl of the previously diluted samples to 900 µl of mobile phase. This final dilution is conducted in a 1.5 mL HPLC vial.

A.4 HPLC method

Mobile phase flow rate: 0.8 mL/min.
Time: 5 min.
Temperature: 40 °C.
Inj. volume: 20 µL.
Detection: 230 nm.

The typical retention time for Melitracen is 2.37 min. The analysis should lead to a chromatogram similar to Figure A.1.

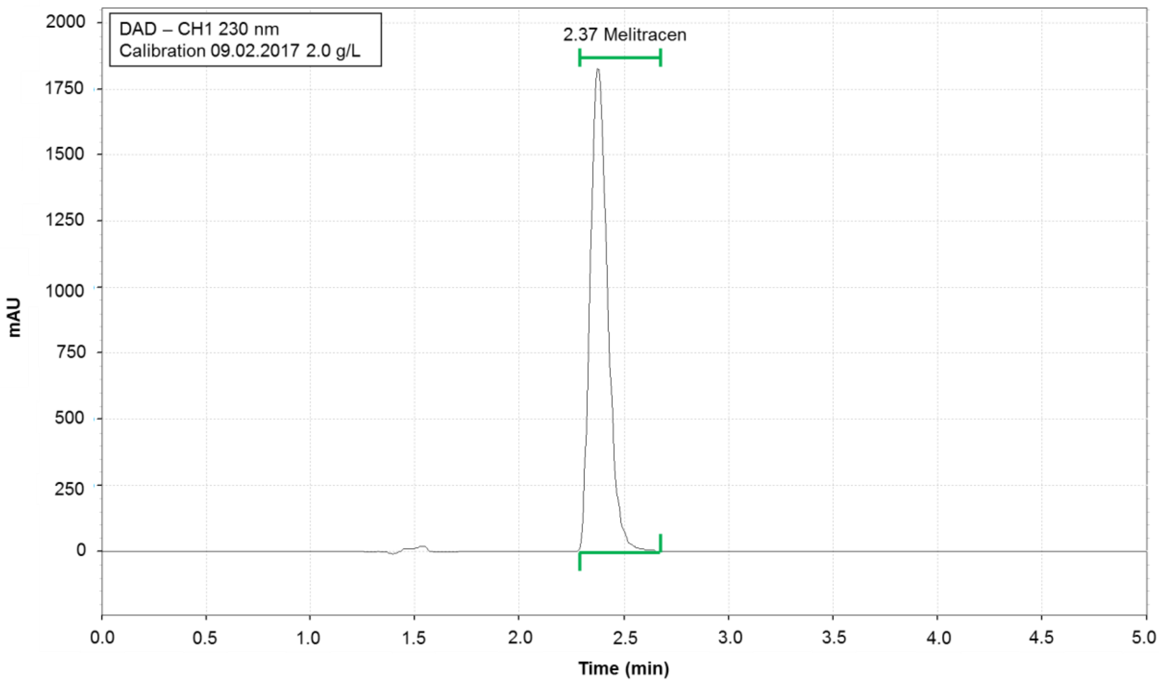

Figure A.1 Typical chromatogram from HPLC analysis of a Melitracen HCl – ethanol solution, corresponding to the maximum studied concentration (2.0 g/L before the last dilution).

A.5 Preparation of standards

1. Dry appr. 2 g Melitracen HCl in the oven at 110°C for at least 20 hours.
2. Using the dried crystals, prepare 6 standards with the concentrations stated in Table A.2. The dilutions are conducted in a volumetric flask using absolute ethanol as a solvent.
3. Prepare the HPLC samples by pipetting 100 μl of the standard solution to 900 μl of mobile phase. This dilution is conducted in a 1.5 mL HPLC vial.
4. Store the standards in closed 20 mL vials (dated). They should be kept in the fridge and replaced at least once every 2 months, or when a significant change in absorbance is observed. The calibration line should be repeated every time a new mobile phase is prepared.

Table A.2 Standard concentrations and amounts for preparation.

Concentration (g/L)	Amount to weight (g)	Standard volume (mL)
0.4	0.0400	100
0.7	0.0700	100
1.0	0.1000	100
1.3	0.1300	100
1.6	0.0800	50
2.0	0.1000	50

These standard concentrations typically yield a nonlinear calibration line as shown in Figure A.2. This shape was consistent throughout the project and is likely a consequence of the high concentrations in the injected sample. Lower concentrations were not employed as the dilution factors to obtain a linear plot were unreasonably high.

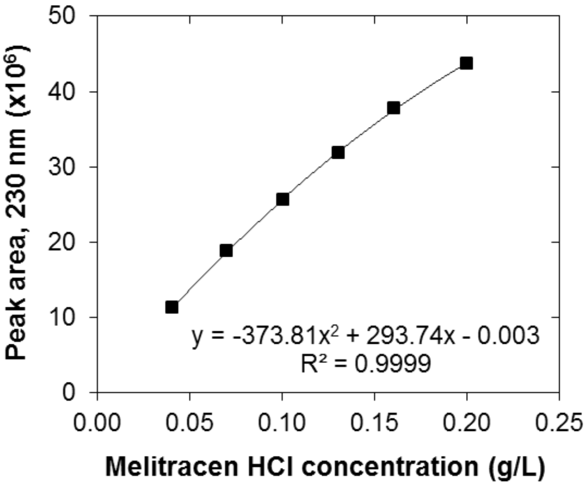

Figure A.2 Typical calibration curve for the determination of Melitracen HCl concentrations from HPLC analysis. The values are plotted including the standards' dilution with mobile phase.

Appendix B – Supporting information, Ch4

B.1 Effect of the number of measured crystals on the size distribution

The number of measurements conducted for image analysis was determined based on the variations in crystal size induced by a change in the crystallization conditions. Figure B.1 shows the average crystal width (number based) plotted against the number of measurements for 5 experiments that exhibited different crystal size distributions. The average crystal width typically stabilizes after 200 measurements, after which the fluctuations in the average value (<5%) are significantly lower than the variation between experiments.

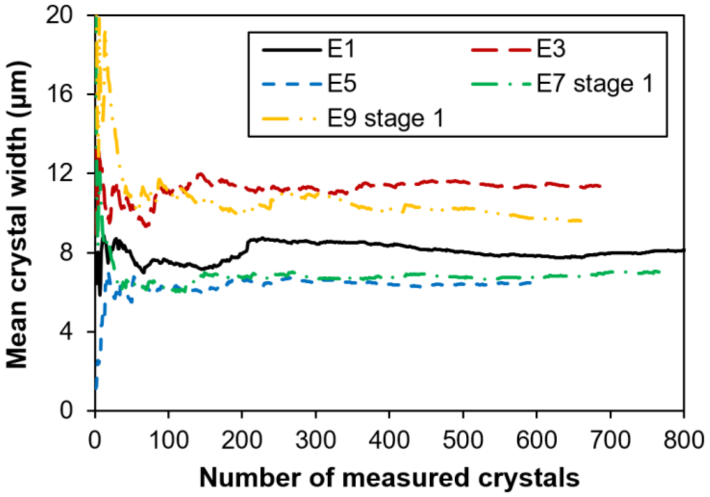

Figure B.1 Variations in the number based mean crystal width over the number of measured crystals during image analysis of experiments 1, 3, 5, 7 and 9.

Note that the volumetric distribution is based on the higher end of the number based distribution, which contains a smaller amount of samples and thus it is more scattered. To study the accuracy of the volumetric distributions obtained with 700 crystals, the measurements for experiments E1 and E4 were conducted in duplicate with approximately 700 crystals per repetition, coming from different pictures of the same experiment. The mass-based mean sizes were considered to be the least reproducible value for these measurements, since they are heavily dependent on the higher end of the distribution. Thus, the measurement error was estimated from the reproducibility of these values. The obtained results are reported in Table B.1.

Table B.1 Results from the duplicate measurements of the mass-based mean crystal length and width for runs E1 and E4.

Run	Dimension	Mass-based mean size, R1 (μm)	Mass-based mean size, R2 (μm)	Average ± SD (μm)	Error (%)
E1	Width	27.6	27.0	27.3 ± 0.3	2.2
	Length	168	203	185 ± 18	19
E4	Width	21.4	24.1	22.8 ± 1.4	12
	Length	162	177	169 ± 7	8.7

In this work, E4 and E5 presented the smallest crystal sizes, with a mass-based mean crystal width of 23 μm for both experiments. The largest mass-based crystal width, obtained at the second stage of E9, was 42 μm. Considering that the estimation error can be as high as 20 %, care should be taken when studying small variations in the crystal size distribution. Furthermore, it is important to induce significant variations in the process conditions during the study, and to compensate the uncertainties on the size distribution by using a large amount of experiments. The obtained variations during the MSMPR experiments were considered high enough to study an overall trend, although they may be limited for very similar experiments. This estimation error explains the observed differences between the observed and model predicted crystallization kinetics, and further supports the need for a reliable automated size measurement that increases the number of measurements by at least an order of magnitude.

B.2 XRPD patterns for the MSMPR product

The obtained XRD patterns from experiments 1, 3, 6 and 8 are reported in Figure B.2. These experiments were selected to include the effects of supersaturation and temperature in the analysis. As it was expected for a system without previous polymorphism issues, the crystal structure remains unaltered in the MSMPR experiments. Furthermore, based on the background of the XRD patterns, the product shows a similar degree of crystallinity than that found in the batch product.

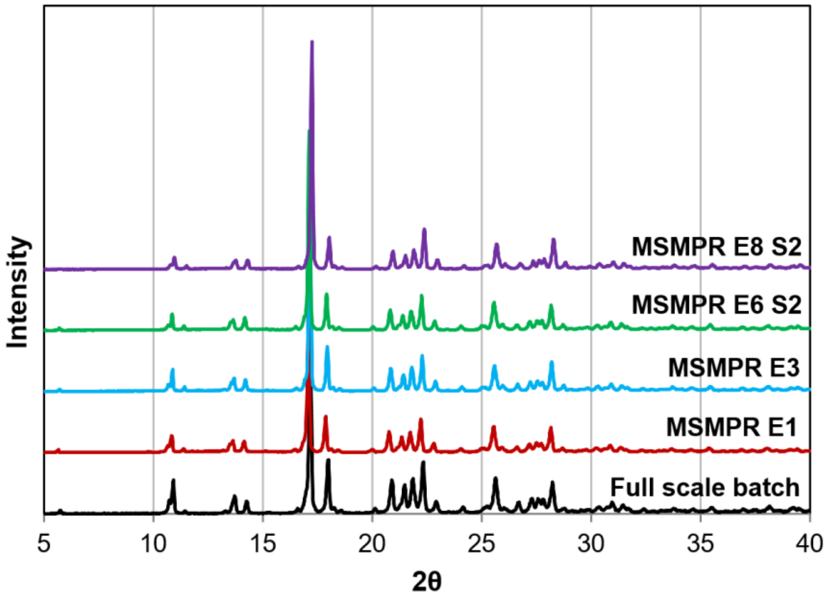

Figure B.2 XRD patterns of the crystals obtained from full-scale batch and lab scale MSMPR crystallization.

Appendix C – Supporting information, Ch5

C.1 XRPD patterns of the crystallized samples

At the end of the experiments with air injection, the crystallized samples were filtered together and the powder was analyzed using X-Ray Powder Diffraction. The resulting patterns are reported in Figure C.1 and Figure C.2.

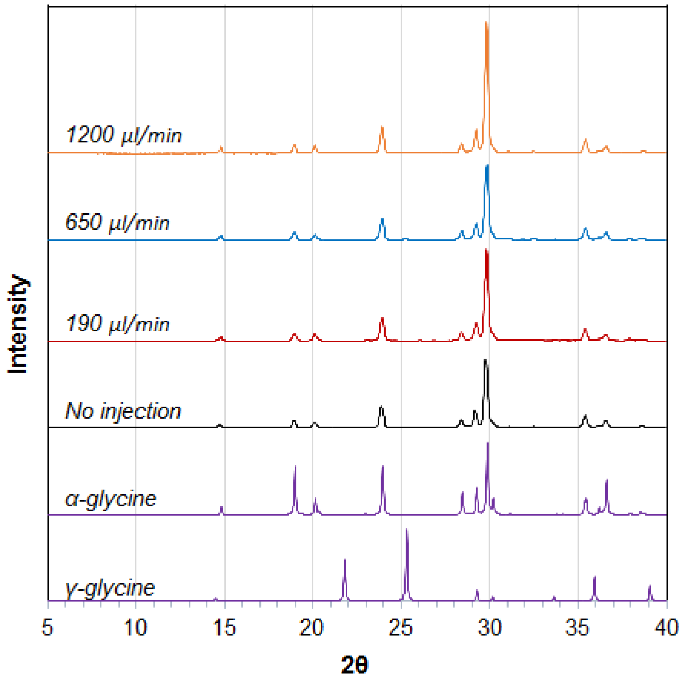

Figure C.1 XRD patterns of the glycine samples crystallized with air injection. The reference patterns (purple) were calculated using the Mercury software from Cambridge Crystallographic Data Centre (CCDC).

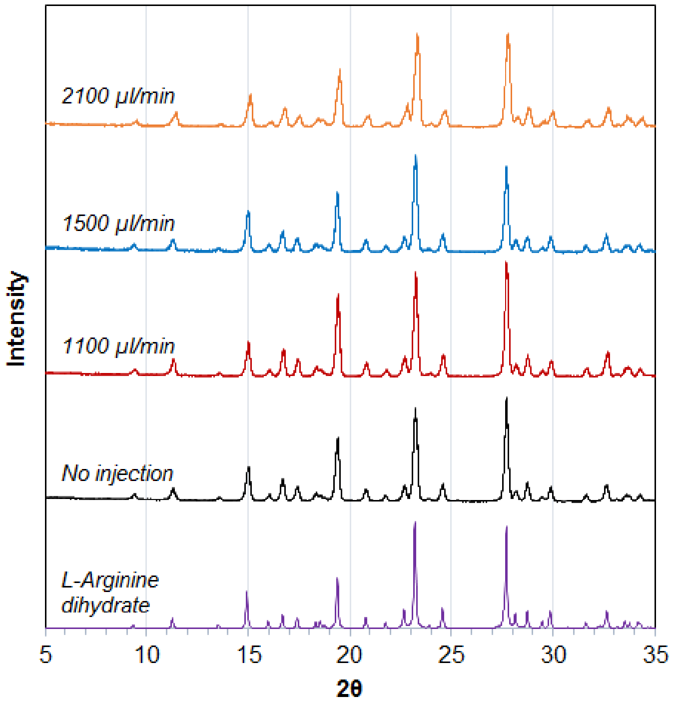

Figure C.2 XRD patterns of the L-arginine samples crystallized with air injection. The reference patterns (purple) were calculated using the Mercury software from Cambridge Crystallographic Data Centre (CCDC).

C.2 Logged air temperature and saturation data

Throughout the course of the experiments with air injection, the temperature and Relative Humidity (RH) of the injected air were measured every 5 minutes with a sensor located at the end of the second condenser (see Figure 5.1). The logged data is plotted in Figure C.3 and Figure C.4.

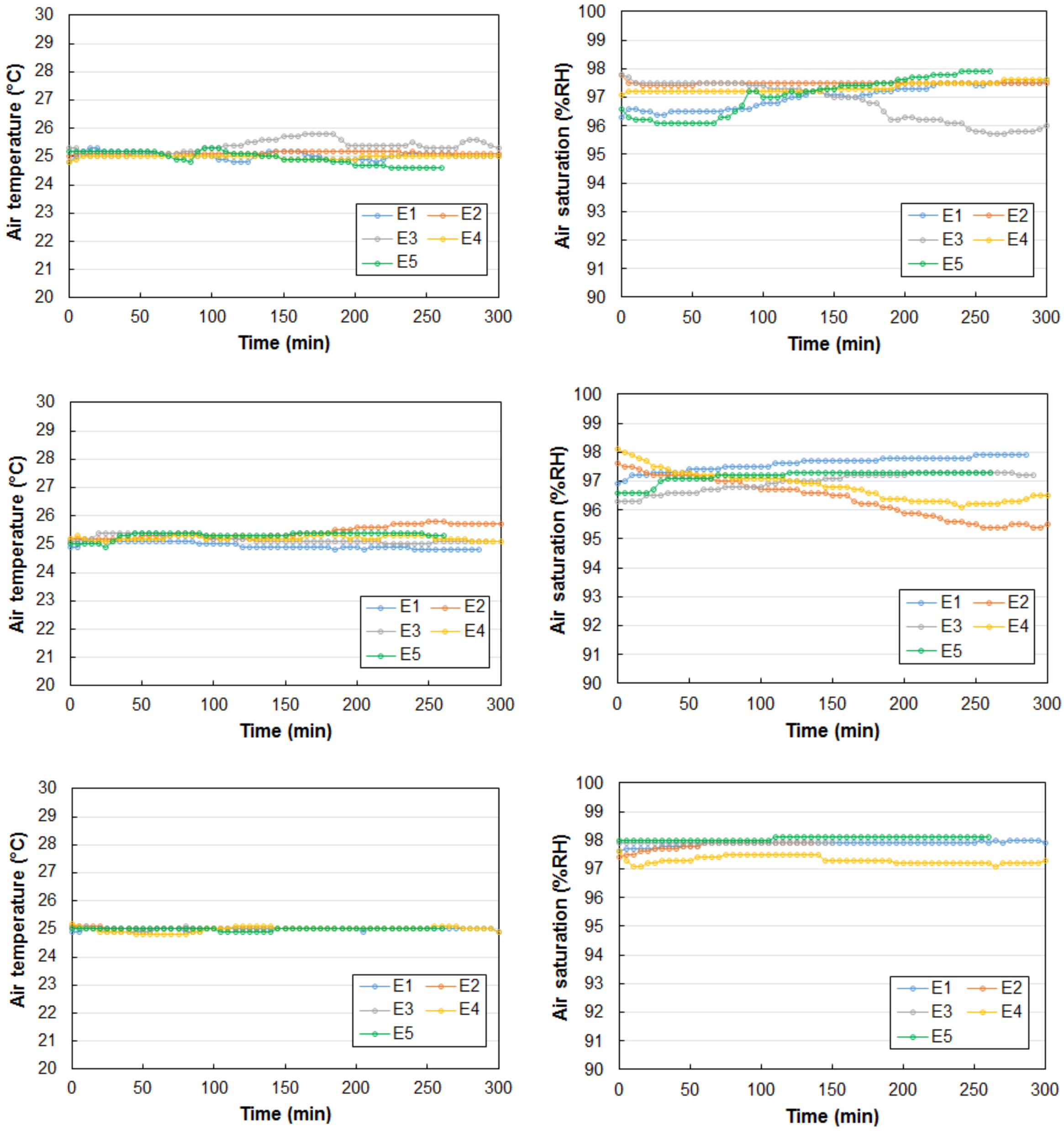

Figure C.3 Evolution of the air temperature and saturation throughout the experiments with air injection on glycine solutions. Top: 200 µl/min; Middle: 650 µl/min; Bottom: 1200 µl/min. E1-E5 correspond to 5 repetitions at the same conditions. Each of these repetitions contains up to 16 parallel samples.

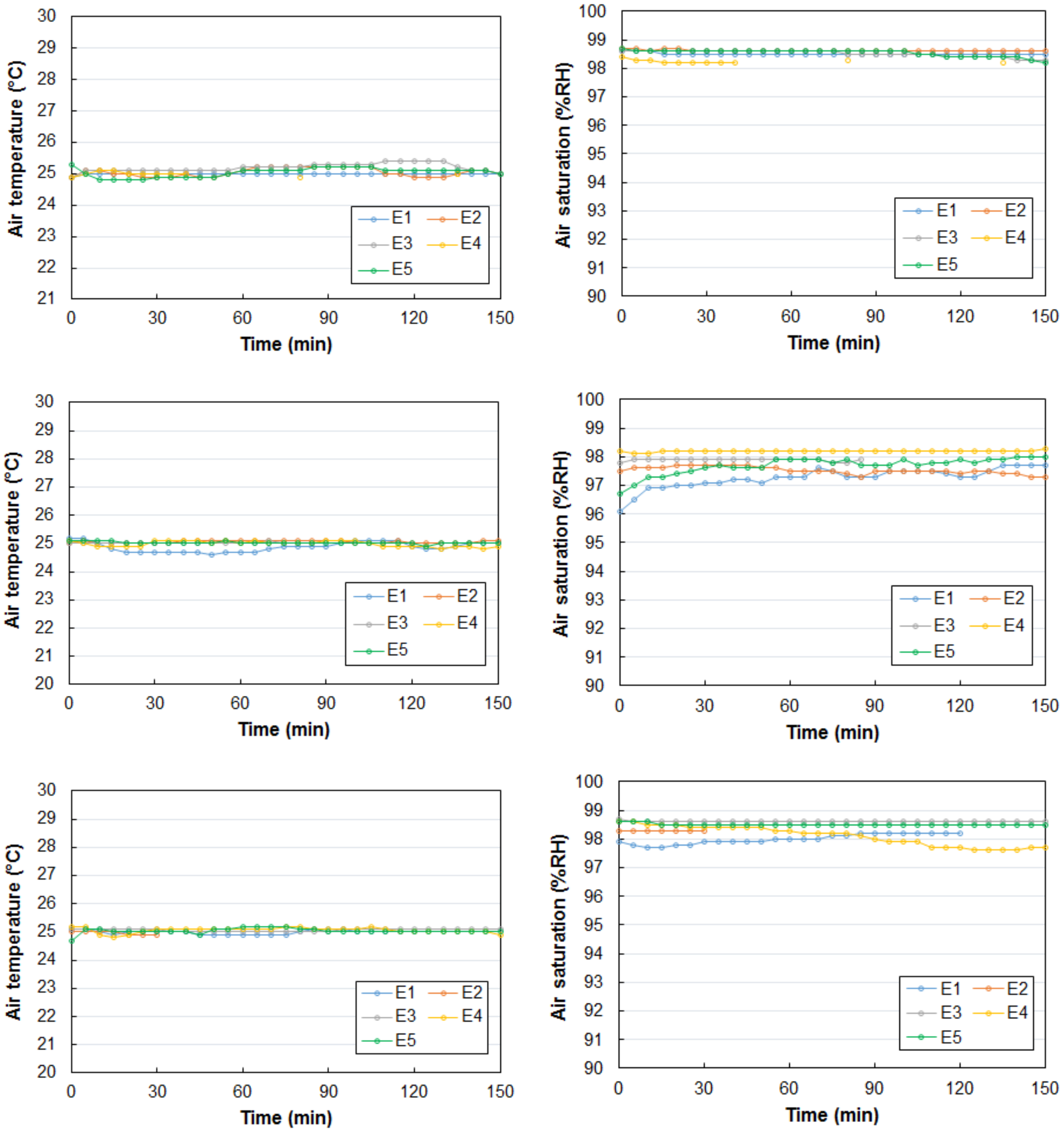

Figure C.4 Evolution of the air temperature and saturation throughout the experiments with air injection on L-arginine solutions. Top: 1100 μl/min; Middle: 1500 μl/min; Bottom: 2100 μl/min. E1-E5 correspond to 5 repetitions at the same conditions. Each of these repetitions contains up to 16 parallel samples.

Appendix D – Supporting information, Ch6

D.1 Effect of gas injection on solvent evaporation

Given that this study covers the effect of a flowing gas on MSMPR crystallization kinetics, the effects of solvent evaporation that could trigger a supersaturation increase must be mitigated to get reliable conclusions. This is not a concern when the gas is internally circulated from the headspace, as the gas phase will be saturated and roughly at the same temperature than the magma. However, using an external gas feed requires quantitative knowledge on its effect on supersaturation.

Figure D.1 shows the evolution of the solute concentration over 7 hours of gas dispersion in an undersaturated API-ethanol solution at 10 °C.

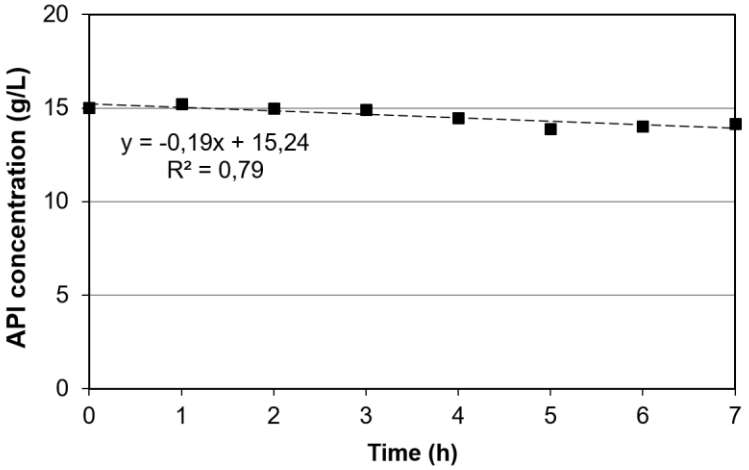

Figure D.1 Evolution of the API concentration in the undersaturated solution over 7 hours of gassing. Temperature: 10 °C. Impeller speed: 800 rpm. Dispersion from gas entrainment and bottom injection (2.5 L/min, pre-saturated gas).

Over the seven hour long experiment, the API concentration dropped from 15 g/L to 14 g/L, corresponding to a condensation rate of 9 mL/h. Consequently, the ethanol concentration in nitrogen achieved in the gas traps (working at 20 °C) falls above the gas saturation point at 10 °C. The experiments in this work have a residence time between 45 min and 60 min. Considering the existing variations between experiments and the short residence times, variations in the mother liquor concentration induced by the gas phase are negligible in the MSMPR crystallizer.

D.2 Preliminary mixing and product removal studies

To investigate the effects of agitation intensity and foam formation in three-phase mixing, the homogeneous distribution of solids in the MSMPR crystallizer was investigated with an API suspension at equilibrium. A 2 L suspension was prepared with a total concentration of 100 g/L of Melitracen HCl in ethanol. 900 mL of the prepared suspension were poured in the crystallizer and the rest was saved for refilling the vessel between samples. The agitation speed was set to 800 rpm for the measurements. 4 mL HPLC samples were taken from the suspension at three different positions in the crystallizer, being 5, 63, and 115 mm from the bottom of the vessel. The sampling was conducted in triplicates before the vessel was refilled to 900 mL. Then, gas dispersion was started with the maximum investigated hold-up (12%) and the sampling was repeated in triplicates. To validate the accuracy of the off-line FBRM sampling, the chord length distribution was measured in-line from the top of the crystallizer and from 45 mL off-line samples taken at the three different positions previously mentioned. The vessel was refilled to 900 mL before each sample. The obtained results, summarized in Table D.1, demonstrate that gas dispersion has no significant impact on the crystal concentration or the size distribution in the crystallizer.

Table D.1 API concentrations and square weighted mean chord lengths for the samples taken at different positions in the MSMPR crystallizer. The liquid level had a total approximated height of 120 mm.

Sampling height (mm)	C_{API} (g/L) – No gas	C_{API} (g/L) – 12% hold-up	FBRM Sqr wt mean (µm) – No gas	FBRM Sqr wt mean (µm) – 12% hold-up
5	100.3 ± 1.9	103.8 ± 1.6	44.5 (off-line)	44.3 (off-line)
63	100.6 ± 0.4	99.6 ± 2.5	42.9 (off-line)	44.8 (off-line)
115	102.6 ± 2.3	99.7 ± 2.8	43.2 (off-line) 44.0 (in-line)	43.8 (off-line)

D.3 Measured steady state classification in the MSMPR crystallizer

The steady state classification in the MSMPR crystallizer was studied at the end of each experiment by taking three magma samples at different positions in the crystallizer. The classification level was studied from the fraction of API concentration between the MSMPR crystallizer and the dissolver. Results are provided in Figure D.2.

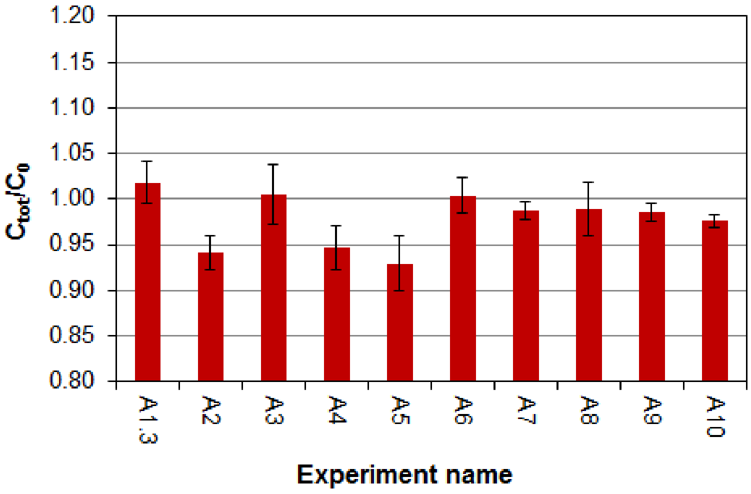

Figure D.2 Steady state classification values for each continuous crystallization experiment, expressed as the fraction between the API concentration in the magma and that in the dissolver. The error bars correspond to the standard deviation from HPLC analysis accounting for error propagation.

None of the experiments presented a significant excess in the API concentration at the crystallizer over that at the feed vessel. On the contrary, some of the experiments presented a lower API concentration in the crystallization magma (up to 7%). These results do not show a particular trend, but share similar values with our observations at a smaller scale and are likely related to the accuracy of the sampling method. Indeed, when a suspension is being sampled, classification of the solid phase can occur during sampling leading to a small reduction in the measured API concentration. As most of the experiments show deviations lower than 2%, it is reasonable to assume that there is no significant classification in the steady state crystallizer.

D.4 Detection of crystal breakage in the experiments with variable mixing

To study the reason behind the crystal size distribution variations in experiments A7, A1.3 and A8, optical microscopy pictures showing the 2D projection of the steady state magma were manually analyzed. The analysis was conducted for 700 crystals using the image processing software ImageJ (ver. 1.6.0). The resulting crystal shape distributions, reported in Figure D.3, show no significant variation in the crystal shape.

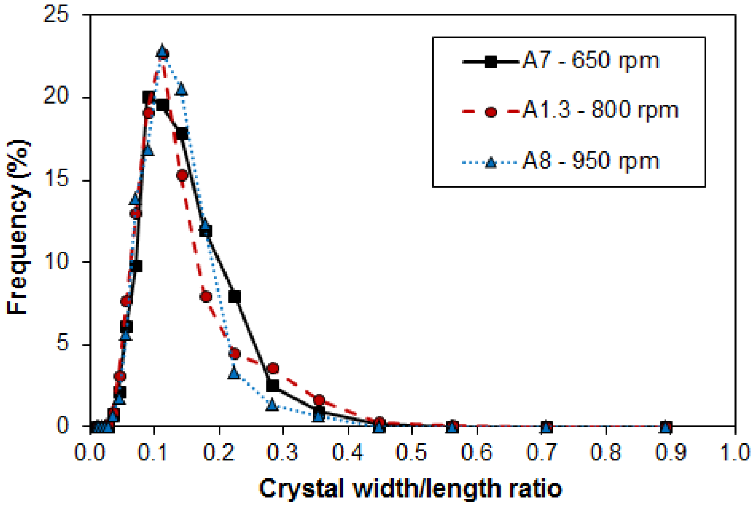

Figure D.3 Steady state crystal shape distribution for experiments A7, A1.3 and A8, obtained from the 2D projection of the crystallization magma.